On the Exploration of Quasars and the Astrometric Microlensing Effect with the Gaia Satellite

Svea Proft

Astronomisches Rechen-Institut

Zentrum für Astronomie der Universität Heidelberg

Heidelberg 2016

Dissertation
submitted to the
Combined Faculties for the Natural Sciences and for Mathematics
of the Ruperto-Carola University of Heidelberg, Germany
for the degree of
Doctor of Natural Sciences

Put forward by

Dipl.-Phys. Svea Proft
Born in: Wolfen

Oral examination: June 29, 2016

On the Exploration of Quasars and the Astrometric Microlensing Effect with the Gaia Satellite

Über die Erforschung von Quasaren und dem astrometrischen Mikrolinseneffekt mit dem Gaia-Satelliten

Zusammenfassung: Seit fast zwei Jahren scannt der Satellit Gaia den Himmel, um eine bisher unerreichte Positionsgenauigkeit bei Sternen zu erreichen und eine Vielfalt an Daten zu gewinnen. In dieser Arbeit beschäftigen wir uns mit zwei verschiedenen Fragestellungen im Hinblick auf Gaia. Im ersten Forschungsschwerpunkt ermitteln wir, welche der gewonnenen Gaia-Daten dazu geeignet sind, den Aufbau von Quasaren besser zu verstehen. Dazu simulieren wir die niedrig- und hochaufgelösten Quasarspektren, die von Gaias blauem und rotem Photometern bzw. vom Radialgeschwindigkeitsspektrometer (RVS) erzeugt werden. Weiterhin untersuchen wir helle SDSS-Quasare, die eine Rotverschiebung aufweisen, bei der breite Emissionslinien (BEL) in den Spektralbereich des RVS fallen. Wir finden heraus, dass niedrig aufgelöste Quasar-Spektren dazu genutzt werden können, um die Äquivalentbreite, Kontinuumsvariabilität, und den so genannten Baldwin-Effekt zu untersuchen. Für etwa siebzig helle Quasare wird Gaia zusätzlich hochaufgelöste Spektren aufnehmen, mit denen die Variabilität der BEL anhand des Linienprofils erforscht werden kann. Aus unseren Analysen folgern wir, dass Gaia eine große Datenmengen zur Verfügung stellt, die man nutzen kann, um die Variabilität in Quasarspektren besser zu verstehen. In unserem zweiten Forschungsschwerpunkt tragen wir dazu bei, astrometrische Mikrolinsenereignisse in den Gaia-Daten besser vorherzusagen. Auf diese Weise kann zeitgleich die zugehörige Helligkeitsveränderung beobachtet werden. Um unsere bereits publizierte Suche nach Mikrolinsenereignissen (Proft et al. 2011) zu verbessern, vergrößern wir den Suchradius um potentielle Linsensterne und überprüfen erneut die Eigenbewegungen der Linsen. Aufgrund der Programmoptimierung finden wir fünfzig neue potentielle Mikrolinsenereignisse, von denen sechs berechnete Positionsveränderungen aufweisen, die zu einem messbaren Gaia-Signal führen können. Derzeit sind die Fehler der Messgrößen zu groß, um zeitnah diese Ereignisse zu verfolgen. Wir werden beobachten, ob unsere Mikrolinsenvorhersagen eintreten und können mit zukünftigen Gaia-Daten präzisere Vorhersagen treffen.

On the Exploration of Quasars and the Astrometric Microlensing Effect with the Gaia satellite

Abstract: For two years, the Gaia satellite has been scanning the sky to obtain an unmatched positional accuracy of stars and a variety of data. In this thesis, we investigate two different kinds of questions with respect to Gaia. In our first research focus we explore Gaia data that is suitable to learn more about the structure of quasars. For this, we simulate low- and high-resolution quasar spectra as they would be generated by Gaia's blue and red photometers and the radial velocity spectrograph (RVS). Furthermore, we investigate bright SDSS quasars with broad emission lines (BELs) redshifted into the wavelength range of Gaia's RVS. We find out that quasar low-resolution spectra enable the study of equivalent widths, continuum variability, and the so called Baldwin effect. For about seventy bright quasars, Gaia will obtain high-resolution spectra from which BEL variability can be studied using the line profile. From our analysis we conclude that Gaia provides a large amount of data which we can use for a better understanding of variability in quasar spectra. In our second research focus, we improve the prediction of astrometric microlensing events with Gaia data. When we predict such events precisely, we could plan to observe the corresponding photometric amplification simultaneously. To improve our published search for microlensing events (Proft et al. 2011), we increase the search radius around a potential lensing star and check once more the proper motion of the lenses. Due to the revision of our program, we find fifty new potential microlensing events. Six have estimated positional changes that could lead to a detectable Gaia signal. Currently, the errors of our calculated quantities are too large to follow up the events in real time. We will monitor whether our microlensing predictions are correct and with future Gaia data we can make more precise predictions in order to develop observational campaigns.

List of Acronyms

BAL	Broad Absorption Line
BEL	Broad Emission Line
BLR	Broad Line Region
BP	Blue Photometer
FWHM	Full Width at Half Maximum
GAVO	German Astrophysical Virtual Observatory
LSPM-North	Lepine and Shara Northern Stars Proper Motion (Lepine & Shara 2005)
NAL	Narrow Absorption Line
NEL	Narrow Emission Line
PPMX	Position and Proper Motions eXtended (Roeser et al. 2008)
PPMXL	PPMX Large (Roeser et al. 2010)
P2011	Proft, Demleitner, and Wambsganss 2011
PW2015	Proft and Wambsganss 2015
RP	Red Photometer
RVS	Radial Velocity Spectrograph
SDSS	Sloan Digital Sky Survey
SMBH	Supermassive Black Hole
SNR	Signal-to-Noise Ratio
SPHERE	Spectro-Polarimetric High-contrast Exoplanet REsearch
UCAC3	Third USNO CCD Astrograph Catalog (Zacharias et al. 2010)
VB2001	Vanden Berk et al. (2001)
VLT	Very Large Telescope
ZIMPOL	Zurich Imaging Polarimeter

Contents

Chapter 1

Introduction

For about four hundred years astronomers have been using telescopes to investigate the light of celestial objects. In the early stages only ground-based telescopes were technically realizable and their resolution was significantly improved over time. However, the resolution of earth-based telescopes is limited by atmospheric turbulences (called seeing). Additionally, the atmosphere of our earth absorbs a major fraction of infrared and ultraviolet radiation. For about sixty years now, astronomers have been using space telescopes to avoid the seeing and the influence of weather on earth. These days, we are even able to build space telescopes which orbit other planets in our solar system.

The current cornerstone mission of the European Space Agency is the Gaia satellite which successfully started to observe in 2014. The satellite is located in a stable position about 1.5 million kilometers away from earth. Gaia is an astrometry mission but the data obtained by the satellite is interesting for researchers working in many different astronomical research fields. The main goal of the satellite is to produce a three-dimensional map of our galaxy containing positions, proper motions, and parallaxes for about one billion stars and other celestial objects like quasars up to about 20th magnitude in G. Gaia's predecessor Hipparcos, which was observing about 25 years earlier, provided an astrometry with positional accuracy of about one milliarcsecond for about 118,000 bright stars ($V \lesssim 11\,\text{mag}$). Gaia's end-of-mission positional accuracy will be between 5 and 600 microarcseconds depending on the object type and magnitude[1]. Hence for bright stars ($V < 15\,\text{mag}$) Gaia's accuracy is about two orders of magnitude better than the one of Hipparcos.

The fact that the Gaia satellite provides different instruments performing astrometric, photometric, and spectroscopic observations allows us to study a variety of astronomical objects. Apart from contributing to the understanding of star formation history and the measurement of stellar distances, Gaia also gathers data useful for extragalactic astronomy. For example, Gaia investigates the dynamics, structure, and stellar populations in our local galaxy group and it determines constraints on the fraction of matter and dark energy from quasar microlensing (Perryman et al. 2001). In the end, the Gaia mission will provide processed data and archives with a size of about one petabyte and computer scientists have to think of new ways to offer the data to the scientific community.

---

[1]http://www.cosmos.esa.int/web/gaia/science-performance, accessed on April 13, 2016

1.1 Motivation

We focus on two very different research topics with respect to Gaia. First, we want to determine how quasar spectra appear in Gaia's low- and high-resolution wavelength range and what are the limits in detecting variability within the spectra. Second, we provide a prediction of astrometric microlensing events for nearby high proper motion stars in order to find promising events during the Gaia mission extending Proft et al. (2011). In the following, we motivate our two different research focuses.

Quasar Spectra

Quasars are one of the most luminous objects in the universe. Hence we can observe them until large redshifts (currently until $z \approx 7$) and study the early stages of many galaxies using quasar spectra. Different quasar spectra show some similar features like broad emission lines and a continuum that can be described by a power law. However, there are also many differences between the spectra of individual quasars. For example, different quasars show continua with various slopes, different line widths of broad emission lines, and they can contain broad absorption line features. Most likely, distinct quasar regions cause the various features visible in their spectra. The spectrum of a selected quasar varies with time. We can observe quasar variability in their broad emission lines, broad absorption lines, and continuum on a timescale between a few hours and some years. Furthermore, the different variability features can be dependent but also independent from each other. In this thesis, we study the abilities of Gaia's instruments for detecting quasar spectra that have different redshifts and magnitudes. In particular, we focus on the measurement of variability visible in quasar spectra with Gaia's blue and red photometers and with the radial velocity spectrograph.

Currently, the Sloan Digital Sky Survey (SDSS) provides the majority of quasar spectra. For most of them one spectrum, and for a somewhat smaller fraction a few spectra are available within SDSS. Only a small celestial region (SDSS Stripe 82) provides spectra of about 60 epochs for individual quasars (for example, MacLeod et al. 2010). The resolution of Gaia's low-resolution spectra is about one order of magnitude smaller than the resolution of SDSS spectra ($R_{SDSS} \sim 2,000$). However, we expect that Gaia is measuring three times more quasars than SDSS which additionally have 72 observations (on average) for the low-resolution spectra and 40 observations (on average) for the high-resolution spectra. In this context, Gaia provides the opportunity to investigate quasar variability for an immense amount of objects.

Astrometric Microlensing of Stars

When we observe distant source stars with Gaia, it can happen that a closer star deflects the light of the background star such that Gaia measures a slightly different source position. This effect, which is called astrometric microlensing, is reasonable due to Einstein's general relativity. Because Gaia's main goal is to measure precise positions of stars at different epochs, the satellite is very suitable for the detection of stellar astrometric microlensing events. In addition to a displacement of the source position, the source becomes brighter which we define as photometric microlensing effect. When we are able to observe both, the astrometric and the photometric microlensing event, we can calculate the mass of the lensing star to high accuracies of a few percent. In comparison to the positional shift, we can measure the magnitude amplification only to much smaller angular distances between lens and source. Due to this, the timescale

of astrometric microlensing events is much larger than for the corresponding photometric event. Gaia's scanning law is suitable to detect long-term variations between some weeks and a few years. Hence the satellite will miss the majority of source amplifications and complementary ground-based observations are ideal to add the photometric information. In this context, the prediction of stellar microlensing events is very helpful to improve the amount of microlensing data.

Currently, the Gaia community uses science alerts when the satellite measures a positional shift of stars. Due to Gaia's scanning law, some astrometric microlensing events will not be detected in time to cover the full light curve with ground-based telescopes. Furthermore, with the end of Gaia mission, we would need precise microlensing predictions in order to measure stellar astrometric and photometric microlensing events simultaneously.

1.2 Research Questions

In the first part of this thesis, we want to contribute to understand the kind of quasar variability that will be visible in Gaia's different quasar spectra. In this context, we want to give suggestions what astronomers have to consider or organize before the end-of-mission. For this, we plan to answer the following questions:

- *How do the quasar spectra appear in Gaia's low-resolution spectra?*
  For this analysis, we have to simulate those spectra considering technical details of the blue and red photometers.

- *How many quasars have observable spectral lines in Gaia's high-resolution spectra?*
  Due to the magnitude limit of the radial velocity spectrograph ($G_{\mathrm{RVS}} \lesssim 16\,\mathrm{mag}$), we expect only a small number of quasars with measurable lines.

- *What kind of quasar variability is detectable in the low- and high-resolution spectra?*
  Especially, we have to analyze variability of the quasar continuum, the broad emission- and broad absorption lines, and the narrow emission and narrow absorption lines.

- *How can we study the structure of quasars from Gaia's variability measurements?*
  For this question, we need to analyze potential reverberation mapping campaigns. Furthermore, we have to analyze the profile of spectral lines detectable in Gaia's high-resolution spectral range.

- *Are there possibilities for complementary ground-based observations in addition to Gaia's low- and high-resolution spectra?*
  We have to consider the information that we will obtain from Gaia's preliminary data releases. Additionally, we can look for known quasars with strong variable features.

Additionally, we plan to improve the number of microlensing detections that have the necessary astrometric and photometric information in order to calculate precise stellar masses. On the one hand we want to improve those detections within the Gaia mission. On the other hand we wish to contribute to establishing stellar microlensing as a common tool for precise mass measurements of stars. For these predictions, we want to answer the following three questions:

- *How can we extend our previous microlensing study (Proft et al. 2011) in order to predict new events?*
  Therefore, we need to analyze and improve the parameters of our previous microlensing program.

- *What are the expected centroid shifts and dates at closest approach between lens and source for these events?*
  The quantities are important in order to conclude whether Gaia is potentially able to detect the events.

- *Are there possibilities to improve the current uncertainties in our calculated quantities?*
  Due to the astrometric accuracies of current star catalogs, these microlensing quantities had large uncertainties in our published research.

In Chapter 8, we discuss whether the questions have been answered and the goals have been reached.

1.3   Outline

Starting with this introduction, we organize the thesis into eight chapters. In Chapter 2, we describe the different instruments of the Gaia satellite and emphasize their physical characteristics that are most important for our investigations. Furthermore, we explain Gaia's observing modes which influence the variability studies of quasar spectra and the detection of stellar microlensing events.

In Part 1 of this thesis, we investigate quasar spectra with Gaia. We published the results of this exploration in our paper Proft & Wambsganss (2015). We introduce this part by explaining the standard model of cosmology in Chapter 3. Moreover, we present the current understanding of quasars and their common distinction to other active galactic nuclei. Our quasar research comprises the simulation and study of their expected low- and high-resolution spectra for different redshifts and magnitudes with the Gaia satellite on the basis of a template spectrum and several SDSS spectra. Especially, we evaluate the potential quasar variability analyses using these spectra. We present our results on Gaia's quasar spectra and the variability within the spectra in Chapter 4. Afterwards, in Chapter 5, we search for individual SDSS quasars that have certain redshifts for which a broad emission line falls in the high-resolution spectrum produced by Gaia's radial velocity spectrograph. We apply this analysis for the originally proposed and for the revised magnitude limit of the instrument.

In Part 2 of this thesis, we analyze the stellar astrometric microlensing effect mainly with respect to Gaia but also with respect to the VLT instrument SPERE. For this analysis, we improve our microlensing predictions published in Proft et al. (2011) (see also Proft 2010). In Chapter 6, we describe the photometric microlensing effect, the astrometric microlensing effect, and Gaia's chance to detect both effects. In Chapter 7, we predict astrometric microlensing events during the Gaia mission using nearby stars as lenses that have proper motions larger than 0.15 arseconds per year. Furthermore, we evaluate the events that have centroid shifts that are theoretically observable with the satellite.

At the end, in Chapter 8, we summarize our quasar and astrometric microlensing investigations with Gaia. Additionally, we evaluate the use of preliminary data releases and the final catalog of the Gaia satellite for both science focuses.

Chapter 2

The Gaia Satellite

For about two years the satellite scans the night sky in a predefined pattern. To obtain reliable data distributed over the whole sky with sufficiently high accuracies, 18 months of data are necessary and their evaluation afterwards (Jordan 2008). Due to this, Gaia data is not available yet. The first data release is proposed for late summer this year (September 2016). It will contain information on right ascension, declination and the Gaia G magnitude (see next section). Furthermore, the first release will cover about 90% of the sky. For dense fields more measurements have to be taken for the evaluation. Additionally, for about 2.5 million Tycho 2 stars, the first data release offers proper motions and parallaxes. The next interesting data publication for our purpose is the third data release which is proposed for summer 2018. Among others, it contains the low- and high-resolution spectra generated by Gaia's instruments. We expect the final catalog at the earliest in 2022.[1]

In the following, we present Gaia's equipment and explain the functional principle of the main instruments. In addition to this, we describe how Gaia scans the sky and how many observations we can expect after the end of the mission.

2.1 The Equipment and its Functionality

The spacecraft Gaia has three major modules: the payload module, the mechanical service module, and the electrical service module. In the following, we will only focus on the payload module because it contains all optical instruments and it carries the telescopes. We find most of the technical details of the different instruments that we describe in this section on the main Gaia web pages.[2,3]

The satellite provides two telescopes which share one focal plane. Gaia's focal plane is largest ever developed for a space mission and it consists of 106 CCDs and about one billion pixel. In Figure 2.1, we show Gaia's focal plane. Its main instruments are the sky mapper, the astrometric field, the blue photometer (BP), the red photometer (RP), and the radial velocity spectrometer (RVS). On the focal plane, the light signals of stars and other objects transit the CCDs from left to right which we call along scan direction (perpendicular to this is the across scan direction). At first, the sky mapper detects the photons for all objects that have an apparent (visual) magnitude between $6\,\mathrm{mag} \lesssim G \lesssim 20\,\mathrm{mag}$ and it generates a window around them. In order to avoid large data volumes and to reduce the readout

---

[1]http://www.cosmos.esa.int/web/gaia/release, accessed on April 17, 2016.
[2]http://www.cosmos.esa.int/web/gaia, accessed on April 17, 2016.
[3]http://sci.esa.int/gaia/, accessed on April 17, 2016.
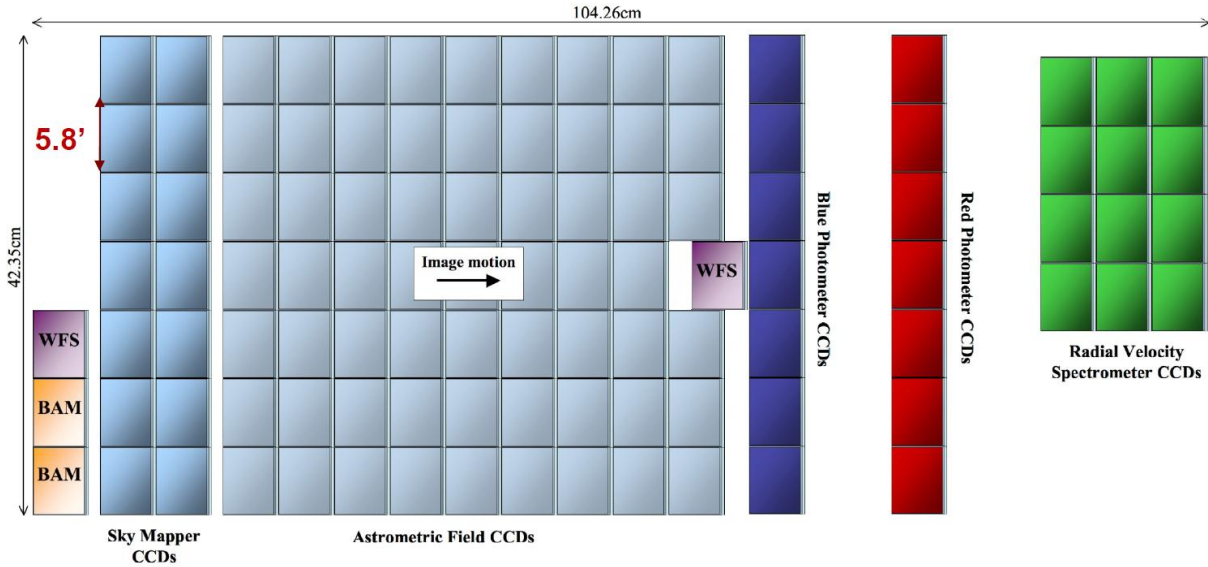
Figure 2.1: The two telescopes of Gaia share a focal plane with 106 CCDs. The main instruments are the sky mapper, the astrometric field, blue and red Photometer, and the radial velocity spectrograph (image: ESA).

noise, the focal plane CCDs only readout the information in this window. The Astrometric Field of the focal plane is responsible for the detection of object positions. Its unfiltered (white) light is defined as Gaia G magnitude. In addition to the astrometric field, the object image crosses the blue and then the red photometer CCDs. By using dispersive prisms, BP and RP generate low-resolution spectra. The integrated flux of the BP and RP spectra delivers the broad band magnitudes G_{BP} and G_{RP} (Jordi et al. 2010). After passing the photometers, the objects transit the RVS which provides a high-resolution spectrum. The integrated flux of this spectrum yields the magnitude G_{RVS} which has to be brighter than 16th magnitude in order to offer a spectrum for the individual objects (for example, Perryman et al. 2001, Jordan 2008, de Bruijne 2012).

The low-resolution spectra cover the wavelength range between $3,300\,\text{Å} < \lambda < 6,800\,\text{Å}$ (BP) and $6,400\,\text{Å} < \lambda < 10,000\,\text{Å}$ (RP), respectively. Their dispersion strongly depends on the wavelength and we will describe those values for both spectra in Chapter 4.2.1. The narrow wavelength interval of the high-resolution spectrum from the RVS is selected with respect to the CaII triplet of stars to $8,470\,\text{Å} < \lambda < 8,710\,\text{Å}$ (Jordi et al. 2010). Its high resolution amounts to $R = \lambda/\Delta\lambda = 11,500$ for bright stars ($m_V \lesssim 11\,\text{mag}$) and $R = \lambda/\Delta\lambda = 5,000$ for the faint magnitude limit. In Figure 2.2, we show the normalized photon response as a function of wavelength for Gaia's pass bands G (black line), G_{BP} (blue line), G_{RP} (red line), and G_{RVS} (green line). In the figure, the wavelength is plotted in unit nanometer. But throughout this thesis, we select the unit angstrom to describe the wavelength.

On the Gaia web page we find the scientific performances as a function of the visual magnitude m_V after the commissioning phase[4]. In Table 2.1, we show selected values of the astrometric, photometric, and spectroscopic accuracy for a solar like star at the end of the Gaia mission. The column astrometry lists the accuracy in measuring parallaxes, the column photometry shows the accuracy of detecting the integrated BP and RP flux, and the column spectroscopy presents the accuracy of radial velocity measurements for visual magnitudes $m_V \leq 12\,\text{mag}$, $15\,\text{mag}$, and $20\,\text{mag}$.

---

[4]http://www.cosmos.esa.int/web/gaia/science-performance, accessed on April 15, 2016.
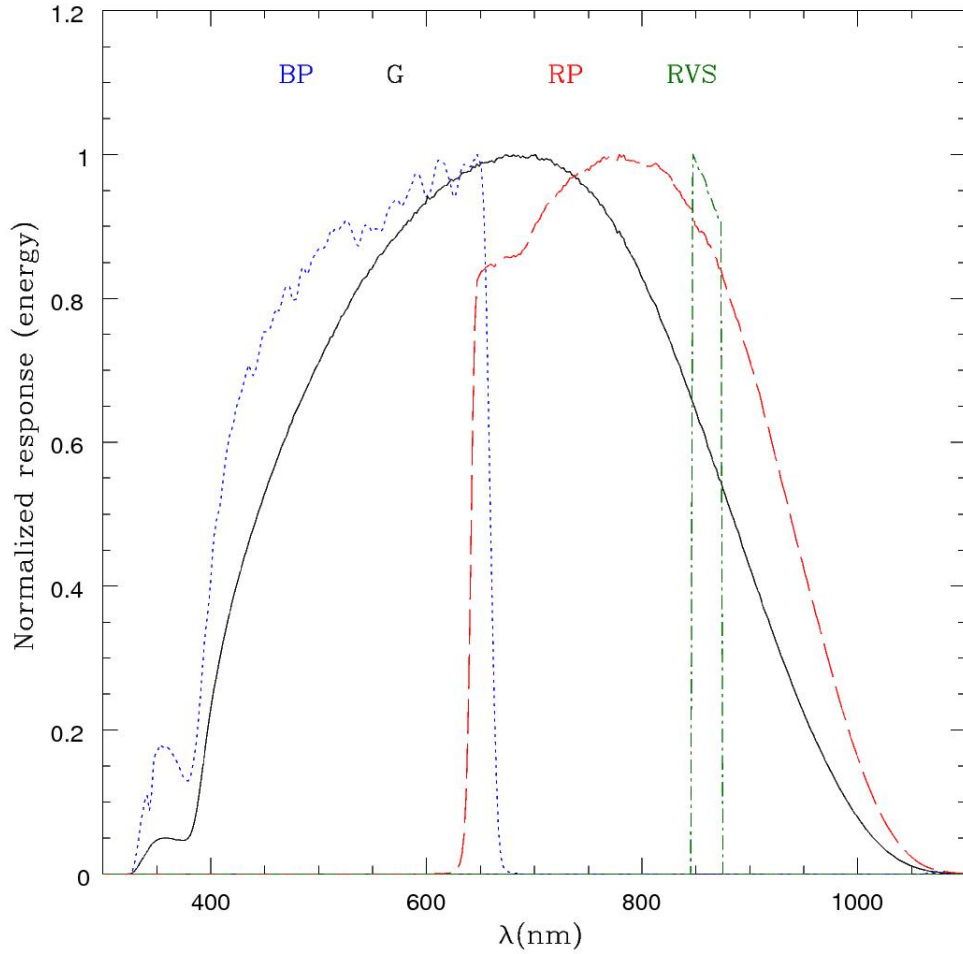
Figure 2.2: In the diagram, we show the normalized photon response as a function of the wavelength. The white light of the astrometric field results in the G-band magnitude (330 to 1050 nm) shown as black curve. The blue and red photometers (BP in blue, RP in red) produces pass bands between 330 to 680 nm and 640 to 1,050 nm, respectively. In comparison to BP and RP, the radial velocity spectrograph (RVS, green) provides a small wavelength range of 847 to 871 nm (Jordi et al. 2010).

Magnitude m_V	Astrometry	Photometry	Spectroscopy
≤ 12 mag	$5 - 14\,\mu$as	4 mmag	1 km/s
15 mag	$24\,\mu$as	4 mmag	15 km/s
20 mag	$540\,\mu$as	80 mmag (BP), 60 mmag (RP)	

Table 2.1: We list the current science performance for astrometry (parallax accuracy), photometry (BP/RP magnitude accuracy), and spectroscopy (radial velocity accuracy) after five years of Gaia's observations.
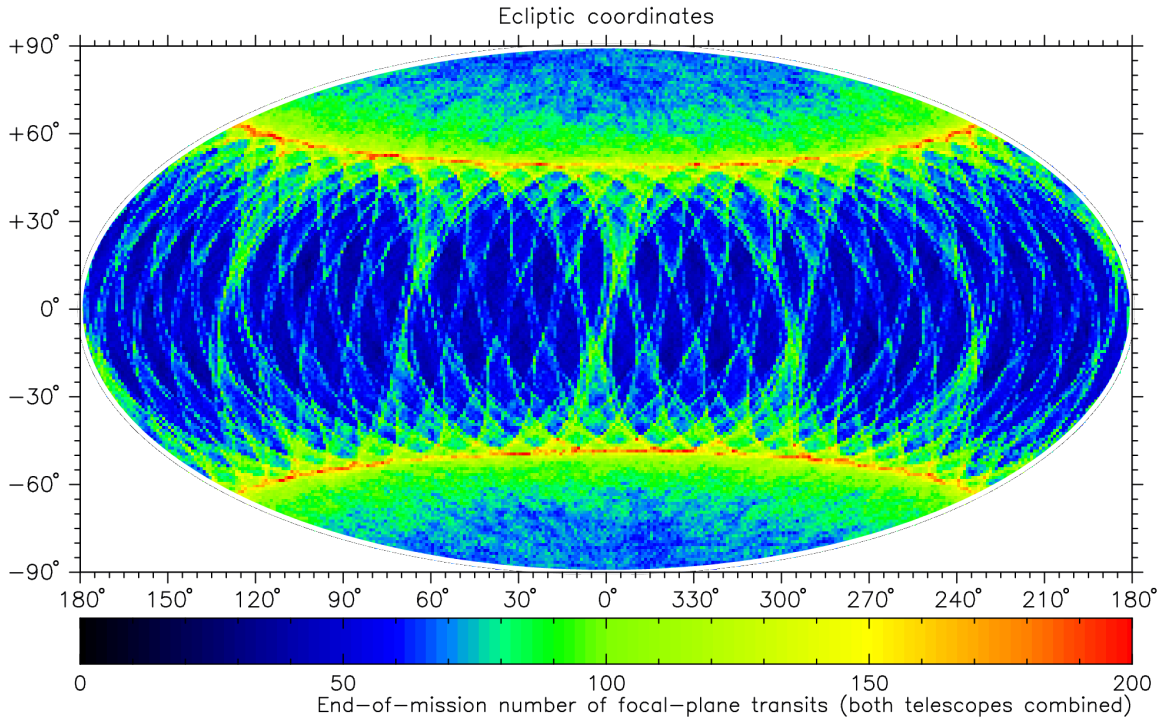
Figure 2.3: The image shows the number of focal plane transits as a function of ecliptic coordinates. The color gradient from black to red presents celestial regions that are getting between 40 and 200 observations after the end of the mission (image: ESA).

2.2 Nominal Scanning Law and Observing Modes

The two telescopes of Gaia observe simultaneously in two fields of view which have a separation, called basic angle, of 106.5 degrees. With a rotational period of six hours, Gaia moves around its axis which corresponds to 60"/s. In this way, the second field of view detects a particular image 106.5 minutes after the first field of view. Due to Gaia's rotations, called nominal scanning law, individual objects will be observed several times within a day. After several subsequent measurements, there is an observational gap of weeks or months depending on the sky field. Celestial objects have sets of subsequent measurements at three or more different epochs after six months of Gaia observations (Jordan 2008). There are about 50 million transits each day and for every observation we obtain astrometric field, BP, and RP information. In Gaia's lifetime of five years, each object will get 72 focal plane transits considering a combined field of view. Taking the focal plane design into account, we expect 72 measurements for the astrometric field, BP and RP but only 40 observations (combined field of view) for the RVS. In Figure 2.3, we present the number of focal plane transits of the combined field of view as a function of ecliptic coordinates. The color gradient (black to red) indicates the number of measurements within five years. We see that there are celestial regions, ecliptic latitudes of about $\pm 45°$, where the satellite observes individual objects about 200 times. However, some regions are only covered 40 times. Because of Gaia's scanning law, we assume five subsequent measurements for a single epoch for our research with BP and RP in this thesis (U. Bastian, priv. comm.). Due to the focal plane design, we select three subsequent measurements ($5 \cdot 4/7$) for the RVS accounting for four rows of CCDs instead of seven rows for all other focal plane instruments. Additionally, we consider observing gaps of typically two months in our discussions.

Subsequently to Gaia's commissioning, Gaia observed 28 days in a special scanning law which covered the region of the ecliptic poles. The results of this program are very useful for short-term variability measurements and we will discuss potential applications in this thesis. Directly after the particular ecliptic pole observations, the nominal scanning law has started to operate and it will last until the end-of-mission (Jordi 2015).

As explained in the introduction, we study two different celestial objects: quasars that show variability in their spectra and high proper motion stars that operate as lenses. For both type of objects, the nominal scanning law is important in order to detect short- or long-term variability within the spectra or to measure the microlensing signal in Gaia's data. For this, we will consider the nominal scanning law in our discussions and perspectives.

Part I

Analyzing Quasar Spectra with Gaia
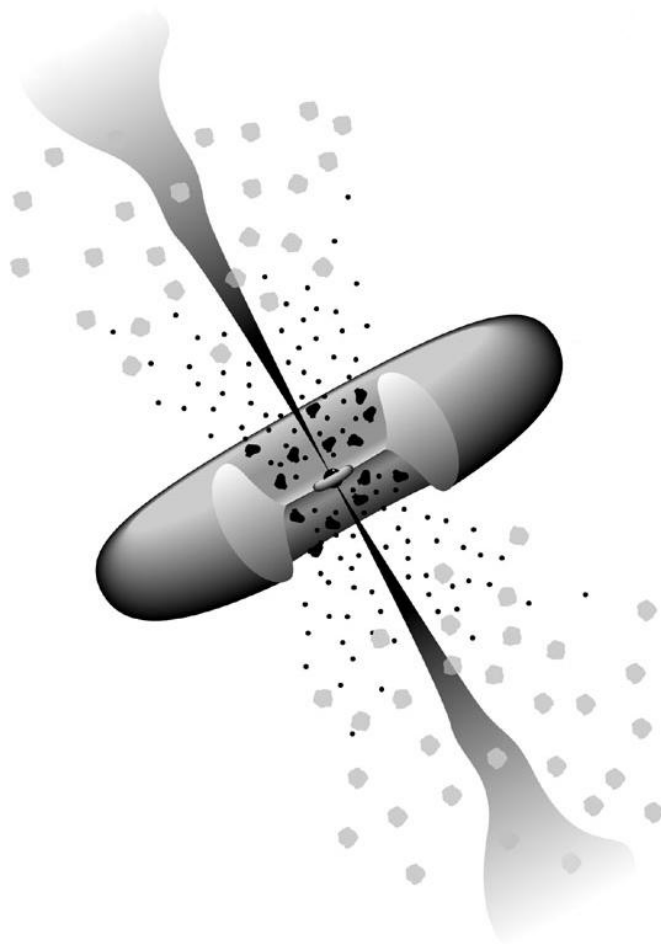
Chapter 3

Introduction

[1] The main research objects of our investigations are quasars. The name quasar ("quasi stellar radio source") refers to their first discovery in radio surveys in the 1950s (e.g., Peterson 1997). At first, quasars were thought to be stars with abnormal spectra due to their apparent brightness and point-like behavior. Maarten Schmidt (1963) was the first who explained the spectrum of the radio source 3C 273 and the important consequence for cosmology. He concluded that quasars have a huge distance to the earth and therefore their spectra are shifted towards higher wavelengths. Theoretically, the spectral lines observable in quasar spectra should have wavelengths λ_0, but the measured wavelengths λ are higher by a factor $1+z$ (Kembhavi & Narlikar 1999). The quantity z is the cosmological redshift,

$$z = \frac{\lambda - \lambda_0}{\lambda_0}, \tag{3.1}$$

which is interpreted as a consequence of an expanding space. Hence the observation of cosmological redshifts is consistent with the Big Bang theory and contradicts the Steady State theory which was competing with the big bang theory when Schmidt (1963) analyzed 3C 273. If we use Hubble's law to estimate the quasar distance in an expanding universe, we can estimate the distance locally ($z \ll 1$) by (Hubble 1929; Planck Collaboration et al. 2015)

$$d = \frac{c \cdot z}{H_0} \quad \text{with} \quad H_0 \approx 67.4 \frac{\text{km}}{\text{s·Mpc}}. \tag{3.2}$$

Therefore, 3C 273 has a distance of $d \approx 700\,\text{Mpc}$ considering its redshift of $z = 0.158$. In our work, $c = 299,792,458\,\text{m/s}$ is always the speed of light in vacuum. Furthermore, for small redshifts the factor $c \cdot z$ is equal to the Doppler velocity v. Considering Hubble's law and the distance modulus, the absolute magnitude of quasars would be

$$M = m - 5\log\frac{cz}{H_0} - 25. \tag{3.3}$$

The apparent magnitude m for quasar 3C 273 amounts to $m_V = 12.9\,\text{mag}$. Calculating its absolute magnitude, the source is about 100 times brighter than our Milky Way. Prior to Schmidt's discovery, researchers did not know energy phenomena that can produce such enormous radiation.

In the first section of this chapter, we describe the actual standard model of cosmology. Afterwards, in section two, we present the model of quasar structures and radiation processes that is most likely

---

[1]Part I cover image: https://ned.ipac.caltech.edu/level5/March04/Torres/Torres2_4.html

according to the current research. Furthermore, we give a short summary of the difference between quasars and other active galactic nuclei (AGNs). In the third section, we discuss the distinct variability scenarios observable in quasar spectra and their physical background.

3.1 Standard Model of Cosmology

In our universe there are four fundamental forces, but only gravitation and electromagnetic force are effective on large scales. On average the matter in space is electrically neutral and hence gravitation is the essential force. Albert Einstein described the gravitation in his general relativity (Einstein 1916). Shortly after, Friedman (1922) used the field equations of Einsteins theory to express the equations of motion of our universe. The Friedman equations

$$H^2 = \left(\frac{\dot{a}}{a}\right)^2 = \frac{8\pi G}{3}\rho - \frac{kc^2}{a^2} + \frac{\Lambda}{3}, \tag{3.4}$$

$$\frac{\ddot{a}}{a} = -\frac{4}{3}\pi G(\rho + 3p/c^2) + \frac{1}{3}\Lambda, \tag{3.5}$$

contain the scale factor

$$a = \frac{1}{1+z}, \tag{3.6}$$

the cosmological constant Λ, the curvature constant k, the gravitational constant G, the energy density ρ, and the isotropic (location-independent) pressure p. Depending on a positively curved, spatially flat, or negatively curved geometry of our space-time, the curvature could be $k = +1$, 0, or -1. The Hubble constant H_0, used in Equation 3.2, is equal to the Hubble parameter $H(a)$ for the scale factor $a = 1$ at the current time. We define a critical density

$$\rho_{\text{crit}} = \frac{3H^2}{8\pi G} \tag{3.7}$$

which allows to derive the curvature of the space-time. When observers measure an energy density in our universe that is larger than the critical density, k becomes positive and the universe could end in a big crunch. On the opposite, a density smaller or equal to the critical one leads to a negative curvature and a continuously expanding space.

To find the best fitting model that describes our universe, researchers have to explain many observed phenomena, the most important are (Schneider 2006):

- accelerated expansion,

- large scale structure (homogeneous and isotropic on scales larger than 100 Mpc),

- Cosmic Microwave Background (CMB) and its structure,

- Big Bang Nucleosynthesis (abundances of light elements).

Currently, the best model that explains the observations is the **ΛCDM** model (lambda cold dark matter). It considers a flat geometry ($k = 0$), a positive cosmological constant Λ, and cold dark matter (CDM). Current research interprets $\Lambda = 8\pi G\rho_{\text{vacuum}}/c^2$ as a constant vacuum energy density, associated with so called Dark Energy, that increases the acceleration of the universe (Carroll 2001). The name **cold**

dark matter reflects that we can not observe dark matter directly, we can only observe its gravitational interaction with "normal" matter. Furthermore, the CDM particles are not relativistic ($v_{cdm} \ll c$) and thus cold. In the ΛCDM model our universe is about 13.8 billion years old (for example, Planck Collaboration et al. 2015).

Considering the ΛCDM model, we can rewrite the first Friedman equation in a dimensionless formula to

$$H(a) = H_0 \sqrt{\Omega_m a^{-3} + \Omega_r a^{-4} + \Omega_\Lambda} \tag{3.8}$$

with

$$\sum_i^{m,r,\Lambda} \Omega_i = \sum_i^{m,r,\Lambda} \frac{\rho_i}{\rho_{crit}} = 1. \tag{3.9}$$

The three Ω_i are the energy density parameters of matter, radiation (neutrinos and photons), and dark energy normalized with the critical density. At current time, one expects a tiny radiation energy density of $\Omega_r \sim 10^{-4}$. Observations like Planck Collaboration et al. (2015) suggest a matter density of $\Omega_m = 0.31 = 0.05 + 0.26$ (baryonic matter plus cold dark matter). Hence the dark energy has the highest fraction ($\Omega_\Lambda = 0.69$). We have to emphasize that, if the model is correct, we know almost nothing about 95% of the content in our universe (dark matter and dark energy).

An important topic in cosmology is the question how far objects are away for a given redshift. If we know the distance of cosmological objects, we are able to infer the age and energy density of the universe. In addition to this, we would get a better understanding of dark energy. The Hubble Equation 3.2 is only valid for small redshifts ($z \ll 1$). For larger redshifts, we have to distinguish between several distances, for example, comoving, luminosity, and angular diameter distance. The comoving distance (Jackson 2015)

$$d_{com} = c \int \frac{dz}{H(z)} \tag{3.10}$$

is time independent and is the distance at which the signal is emitted. The angular diameter distance (Jackson 2015)

$$D_A = \frac{D_{com}}{1+z} \tag{3.11}$$

uses the observed apparent angular size of extended objects to estimate their distance. Furthermore, we can calculate an object distance that results from its luminosity (Schneider 2006; Jackson 2015),

$$D_L = \sqrt{\frac{L}{4\pi F}} \quad (z \ll 1), \tag{3.12}$$

and

$$D_L = (1+z)^2 \cdot D_A \tag{3.13}$$

where L defines the luminosity and F the flux. We can express all distances as a function of the comoving distance which in turn depends on the cosmological model used in Equation 3.8. For small redshifts $z \lesssim 0.1$ all distances are equal whereas for large redshift they diverge dramatically. To infer distances of objects with large redshifts and to test different cosmological models, we need distant objects that are suitable as standard candles or standard rulers. Standard candles are objects for which we know the luminosity and standard rulers are objects for which we are aware of the physical size. For example, type Ia supernovae are important standard candles in cosmology because they have nearly identical light

curves and they are visible up to redshifts of $z \approx 1.7$ (Watson et al. 2011). By using the distance measurements of these supernovae, Riess et al. (1998) and Perlmutter et al. (1999) discovered that the supernovae brightnesses are smaller than expected. Hence the expansion of the universe seem to be accelerated due to dark energy. If we want to study cosmological parameters for larger redshifts, one would need extremely luminous objects with very large redshifts. Therefore, quasars or other near-face-on AGNs are the most suitable candidates for this analysis (Watson et al. 2011). Currently, the accuracies of such AGN Hubble diagrams are not sufficient to use them as standard candles.

3.2 The Nature of Quasars

3.2.1 Quasars and Active Galactic Nuclei

Quasars are Type 1 AGN, characterized by broad emission lines (BELs) with line widths of several tens of Angstroms in the quasar rest frame. Figure 3.1 shows their typical spatial structure schematically and on a logarithmic scale. Quasars contain super-massive black holes (SMBHs) with masses of 10^6 to $10^{10} \, M_\odot$ that are surrounded by an accretion disk. The accretion disks are typically smaller than 0.01 pc (Morgan et al. 2010). The gravitational accretion of gas and dust on this accretion disk produces the continuum emission of quasars. The surrounding broad emission line region (BLR) is smaller than or equal to ~ 1 pc and consists of clouds excited by accretion disk radiation. Cloud velocities larger than 500 km/s cause the BELs in this region. Because of high gas densities in the BLR, only permitted and semi-permitted broad emission lines occur. Farther out, there is a narrow line region (NLR) with cloud velocities about ten times smaller. The relation between the radius R and velocity v is $R \sim v^{-2}$ (e.g., Peterson & Horne 2004). Hence, the size of the NLR is about 100 pc. Due to smaller gas densities in the NLR, the narrow emission lines (NELs) are forbidden lines. Farther out, an expanded dusty torus surrounds the NLR region in quasars. The surface brightness of quasar host galaxies sharply decreases with redshift and hence the host galaxy is only visible for small redshifts (e.g., Disney et al. 1995; Bahcall et al. 1995; Kotilainen et al. 2009).

Quasar spectra typically have a very blue continuum and a number of broad emission lines. The spectra vary a lot from quasar to quasar. Their typical features can be best seen in composite quasar spectra, like that of Vanden Berk et al. (2001). It considers about 2,200 quasars from the Sloan Digital Sky Survey (SDSS) with red magnitudes $r' \lesssim 19$ for $z \lesssim 2.5$ and $r' \lesssim 20$ for higher redshifts. Throughout this thesis, we use this composite quasar spectrum by Vanden Berk et al. (2001) as a template (from now on denoted as VB2001), covering a rest-frame wavelength range between 800 Å and 8,555 Å. Figure 3.2 shows the VB2001 spectrum together with the low-resolution (light blue area, 3,300 Å-10,500 Å) and high-resolution (dark blue area, 8,470 Å-8,710 Å) wavelength regions of Gaia. In the plot we label the significant broad emission lines Hα, Hβ, MgII, CIII], CIV, and Lyα. These BELs play an important role in our study.[2] We are primarily interested in these five lines because they are the most frequently analyzed BELs in literature which are visible over a wide redshift range.

The prominent features in quasar spectra are emission lines. However, many quasars show different kind of absorption lines as well. For example, Peterson (1997) describe three classes of absorption lines: broad absorption lines (BAL), narrow absorption lines (NAL) of heavy elements like carbon or oxygen,

---

[2]Until here, this Section is a slightly changed excerpt of Section 1.2 described in our paper Proft & Wambsganss (2015).
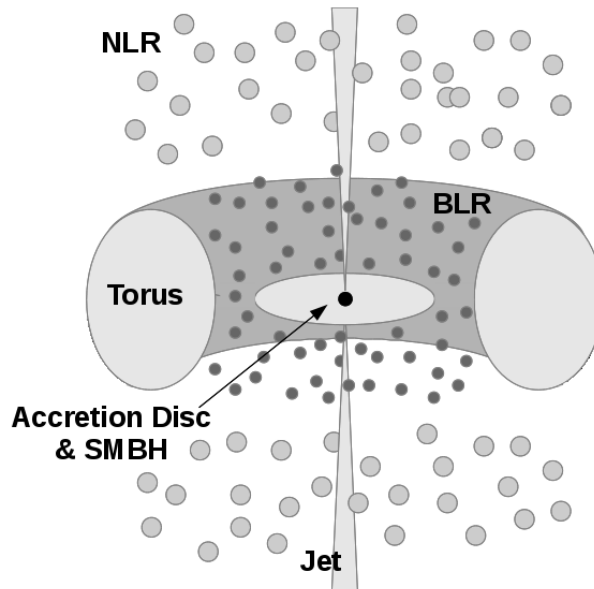
Figure 3.1: Sketch of the assumed geometry of a quasar on a logarithmic scale (based on Urry & Padovani 1995; Beckmann & Shrader 2012): from the inner to the outer parts quasars host a super-massive black hole (SMBH), an accretion disc, a broad line region (BLR), a narrow line region (NLR), jets, and a dusty torus. Image from PW2015.

and the Lyman-alpha forest. Most likely, ionized gas within the quasar is responsible for broad absorption lines. Furthermore, the host galaxy can absorb narrow lines which have a similar redshift as the quasar. If the redshift of a NAL is smaller than the emission line redshift, a galaxy or its halo between observer and quasar causes the absorption. A large number of neutral hydrogen clouds between quasar and observer at many different redshifts absorb quasar light shortwards of the Lyman-alpha BEL. For this reason, one calls these numerous absorption lines Lyα forest.

The origin of the quasar continuum is non-thermal but with thermal components. We can describe the spectral energy distribution (SED) of the continuum by a power law $f_\lambda \sim \lambda^{\alpha_\lambda}$ with wavelength index α_λ (VB2001). The region of optical and ultraviolet emission with wavelengths shorter than 4,000 Å is called "big blue bump". Another noticeable feature between $2,000\,\text{Å} < \lambda < 3,000\,\text{Å}$ (close to MgII) is the "small blue bump" which consists of blended singly ionized iron (FeII) emission lines. In addition to the UV and optical emission due to gravitational infall on the accretion disk, there are further contributions to the continuum. For example, the infrared radiation results from hot dust with temperature up to 2,000 K. In comparison to this, Synchrotron emission causes the flat and non-thermal radio continuum visible in about 10 % of all quasars (Peterson 1997). Moreover, in radio-loud quasars inverse Compton scattering plays an important role. In this scenario the low energy photons are scattered to higher energies by relativistic electrons located in a hot corona surrounding the accretion disk (Hsu & Blaes 1998).

Apart from quasars many different kind of active galactic nuclei (AGN) exist and there are several possibilities to divide distinct AGN types. Other AGN are, for example, Seyfert galaxies, Radio galaxies, and Blazars. Quasars are the most luminous of all AGN. Their luminosities are up to 1,000 times larger than the luminosity of our Milky Way. Current research explains the existence of several types of AGN not only with intrinsic phenomena, but also with orientation effects. The AGN spectra have different characteristics for objects where we can look through the inner regions or even in the jet than objects
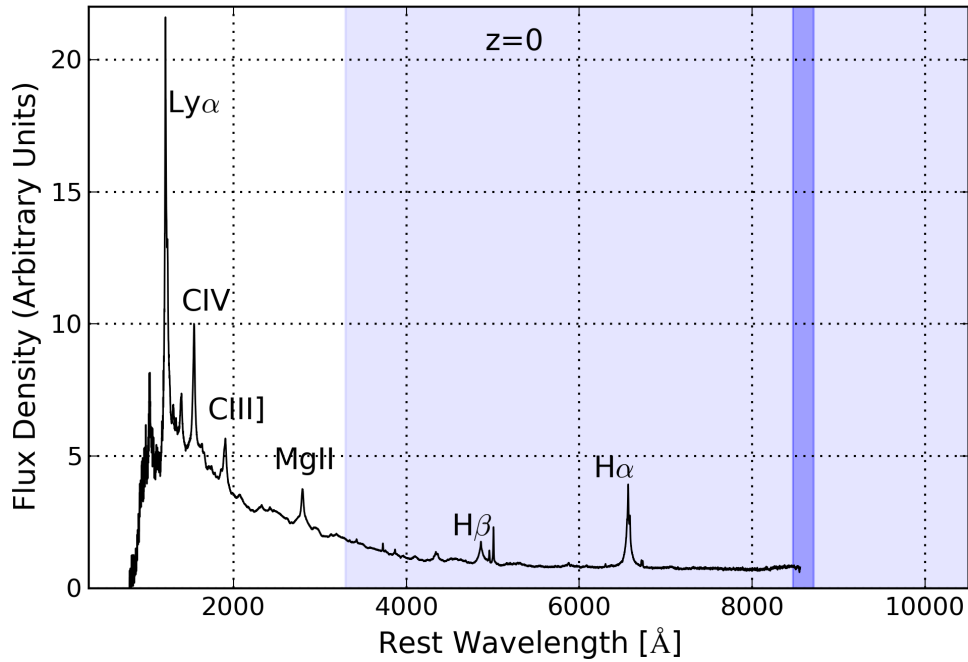
Figure 3.2: Rest frame ($z = 0$) composite quasar spectrum with data from Vanden Berk et al. (2001). Visible are the important broad emission lines Lyα, CIV, CIII], MgII, Hβ, and Hα. The blue areas indicate the low-resolution spectral region of Gaia (light shaded) and the region of Gaia's radial velocity spectrograph (dark shaded). Plot from PW2015.

where the NLR or torus hide the nucleus. Similar to quasars, Seyfert galaxies are also aligned near-face-on and hence they are type 1 AGN. Seyfert galaxies are Spiral galaxies that are less luminous than quasars. In comparison to them, Radio galaxies are elliptical galaxies with strong radio emission. Both Seyfert and Radio galaxies show narrow emission lines (NELs) and sometimes also BELs in their spectra depending on their viewing angle to us. If an AGN jet has an orientation close to the observer, we can measure strong polarized emission that is very variable on short timescales of order days. Such objects (called blazars) have strong radio emission due to the synchrotron mechanism.

3.2.2 Variability of Quasar Spectra

An important property of quasars is their variability which often occurs in the whole wavelength range, in the continuum, in the emission lines, and in the absorption lines. In many cases, the magnitude variations are larger than 0.1 mag (Peterson 1997). The investigation of quasar variability increases the knowledge about quasar structures and their energy processes.

The main reason for variability visible in quasar continua is not well understood. Reasonable explanations are instabilities of the accretion disk and a variable accretion rate. In principle, also gravitational microlensing, jet instabilities, or supernova bursts could be responsible for some spectral changes (Andrei et al. 2009; Popović et al. 2012). Because X-ray detected quasars are much more variable than others, Collin-Souffrin (1991), George & Fabian (1991), and Gil-Merino et al. (2012) suggest that reprocessed X-ray photons from the corona (into UV-optical continuum) could induce short or medium timescale variability. It exists a correlation between the variability that we can see in a quasar continuum

and in the BELs. Due to light travel-time effects, the accretion disk radiation arrives in a mean time τ (quasar rest-frame) at the BLR clouds. These clouds are thought to absorb the energy and then re-emit radiation visible as BELs in quasar spectra. If the continuum shows variability, we can observe these variations in the BELs because of the cosmological time-dilation after a time

$$\tau' = \tau \cdot (1+z). \tag{3.14}$$

Studying the BEL response to continuum variations is referred to as **reverberation mapping** (for example, Peterson 1993 and Chelouche et al. 2012). If we determine the time lag, we can estimate the size of the BLR separated from the continuum region by

$$R_{\text{BEL}} \approx c \cdot \tau. \tag{3.15}$$

The dimension of distinct quasar regions depends on the mass of the black hole. If we can measure the BEL full width at half maximum (FWHM) together with the time lag, it has been found that we can characterize the mass of the black hole to (Peterson et al. 2004; Chelouche et al. 2012)

$$M_{\text{SMBH}} = 2.7 \cdot 10^5 \cdot \left(\frac{\text{FWHM}}{10^3} \frac{\text{km}}{\text{s}} \right)^2 \cdot \left(\frac{\tau}{\text{days}} \right) \cdot M_{\odot}. \tag{3.16}$$

To study BELs and their variability, more often one determines the equivalent widths instead of the FWHM. In comparison to the FWHM, the BEL equivalent width does not depend on the resolution of the spectrograph. The equivalent width is defined as (Peterson 1997)

$$W_{\lambda} = \int \frac{F_{\text{l}}(\lambda) - F_{\text{cont}}(\lambda)}{F_{\text{cont}}(\lambda)} d\lambda \approx \frac{F_{\text{line}}}{F_{\text{cont}}(\lambda)} \tag{3.17}$$

with integrated line Flux F_{line}, line flux at distinct wavelength $F_{\text{l}}(\lambda)$, and continuum flux underneath the BEL $F_{\text{cont}}(\lambda)$.

The time lags in quasar spectra discovered by reverberation mapping are between hours and years (Vanden Berk et al. 2004). But in many cases, the timescale lies between days and some years. For example, MacLeod et al. (2012) analyzed a large sample of SDSS quasars and measured optical continuum variability timescales between $5\,\text{days} < \tau < 2,000\,\text{days}$. Kembhavi & Narlikar (1999) define the variability amplitude by the root mean square dispersion

$$\sigma = \frac{1}{<F>} \sqrt{\frac{1}{N-1} \sum_{i=1}^{N} (F_i - <F>)^2} \tag{3.18}$$

with mean flux

$$<F> = \frac{1}{N} \sum_{i=1}^{N} F_i, \tag{3.19}$$

whereby N is the number of data bins.

The most important continuum and BEL variability dependencies are (Peterson et al. 2004; Meusinger et al. 2011):

- the variability amplitude decreases with wavelength

- the time lag increases with wavelength

- the variability amplitude decreases with luminosity

- the anti correlation of BEL equivalent widths with the luminosity of the close-by continuum).

Baldwin (1977) first discovered the latter effect by studying the CIV line equivalent width. This anti correlation ($W_{CIV} \sim L_\lambda^{-0.17}$) is called **Baldwin effect** and could be detected also for other BELs, but the physical background is still not understood (Wilhite et al. 2006). Wilhite et al. (2005) analyzed a sample of 315 SDSS quasars spectroscopically and explored that the strongest BEL equivalent widths vary only 30% as much as the close-by continuum.

About 10% of all quasars have broad absorption lines, too. Variability within BALs could be due to gas movement across the line of sight or variations in the outflow ionisations. An analysis of BAL variability provides knowledge about quasar outflows like their kinematics, size, or sub-structures. In rare cases and in contrast to BELs, BALs can appear and vanish. BAL variability is only detectable in some troughs. Furthermore, it can occur in an individual line without corresponding changes in other lines (Capellupo et al. 2012).

3.2.3 Quasars with Gaia

During the Gaia mission more than 500,000 quasars will be detected. Out of these objects we know about one third and hence the majority of quasars will be new discoveries. Moreover, Finet et al. (2012) expect that Gaia discovers about 3,000 multiply imaged quasars with the help of strong gravitational lensing. Quasars are necessary for Gaia, because of their huge luminosity together with their large distance to the observer. Due to this, nearly all quasars have negligible parallaxes and a pointlike appearance. Hence Gaia uses these objects for a quasar-based celestial reference frame in order to obtain a high positional accuracy. In detail, roughly 10,000 bright uniformly distributed quasars are necessary to build the reference frame (Andrei et al. 2012; Mignard 2002).

There are several possibilities to identify quasars among other objects. First, one consideres the typical blue quasar spectra with variable features for detection. However, faint quasars with low equivalent width BELs have low signal-to noise ratio (SNR) spectra and hence the spectral signatures are not unique. For example, the colors of white dwarfs, F stars, and red dwarfs are similar to quasar colors for redshifts of $z < 0.5$, $z \sim 2.5$, and $z > 3$, respectively (Claeskens et al. 2006). Second, the fraction of quasars in comparison to stars is much lower in the Galactic plane of our Milky way than at higher Galactic latitudes. These two points together with the lack of proper motions and parallaxes enable to distinguish quasars easily from stars (Mignard 2012). Furthermore, we can compare observed quasars with known AGN catalogs.

The design of Gaia's instruments is perfect for analyzing stellar properties. Additionally, the Gaia mission is a survey and does not distinguish between stars and quasars. Therefore, we get a large amount of quasar data automatically that we can use in addition to the production of the reference frame. In the next chapter, we investigate the possibilities and limits of the data expected to be obtained by Gaia to learn more about quasar spectra and the variability within the spectra.

Chapter 4

Exploration of Quasars with the Gaia Satellite

Gaia will produce an all-sky catalog of 500,000 quasars up to a magnitude limit of $G \approx 20.7\,\text{mag}$ in a redshift range between $0 < z < 5$. Today we know only about 184,000 quasars mainly from the **S**loan **D**igital **S**ky **S**urvey (SDSS) which has a sky coverage of about one third. Together with the huge number of new discovered quasars, Gaia delivers broad band photometry for all observed objects and high-resolution spectra of a small number of bright quasars. As mentioned in Chapter 2, the satellite detects every object on average 70 times in the blue and red photometers (BP and RP) and 40 times in the radial velocity spectrograph (RVS). While the satellite is designed for stars, the huge amount of quasar data together with a large number of observations over a period of five years will enable a promising quasar investigation. In this work, we investigate the scientific output that we can infer from these data as preparation for the first Gaia data releases and the final catalog.

In Figure 4.1 we plot the redshift distribution of all quasars discovered by SDSS in red. For this, we combine the information from data release seven (dr7: Schneider et al. 2010) and data release nine (dr9: Pâris et al. 2012) which have biases to certain redshifts. The quasars are brighter than $r < 22.2\,\text{mag}$ and have redshifts between $0 \lesssim z \lesssim 7$. SDSS uses a 2.5 meter telescope in New Mexico that offers photometry of five optical bands (u', g', r', i', and z') and spectroscopy in a wavelength range of $3{,}600\,\text{Å}$ to $10{,}500\,\text{Å}$ with an average resolving power of about 2,000. Additionally, we present the redshift distribution of quasars from the simulated Gaia catalog (Robin et al. 2012) in blue which contains about 1,000,000 quasars. In reality we expect that Gaia discovers 500,000 quasars or more due to the fact that the simulation reflects what Gaia is able to potentially measure. Robin et al. (2012) did not consider the instrumental effects and error models in their statistical study. To produce the quasars in the simulated Gaia catalog, they considered similar statistical properties as SDSS (for example, redshifts and colors) together with an extrapolation to fainter quasars (Slezak & Mignard 2007). Gaia will obtain a quasar sky coverage of about two third. Due to a huge fraction of stars in the galactic plane, quasars are less observable in this celestial area. In the histogram we can see that the majority of quasars have redshifts between $z = 1$ and $z = 2$ which reflects the quasar history. At the current age of $z = 0$, we do not observe quasars at all. It could be that many galaxies or even all pass a quasar period in their life before achieving its current galaxy phase. Despite the fact that quasars are very faint at high redshift, the number of observed quasars is still too small for a large quasar population at high z and hence it most likely that it
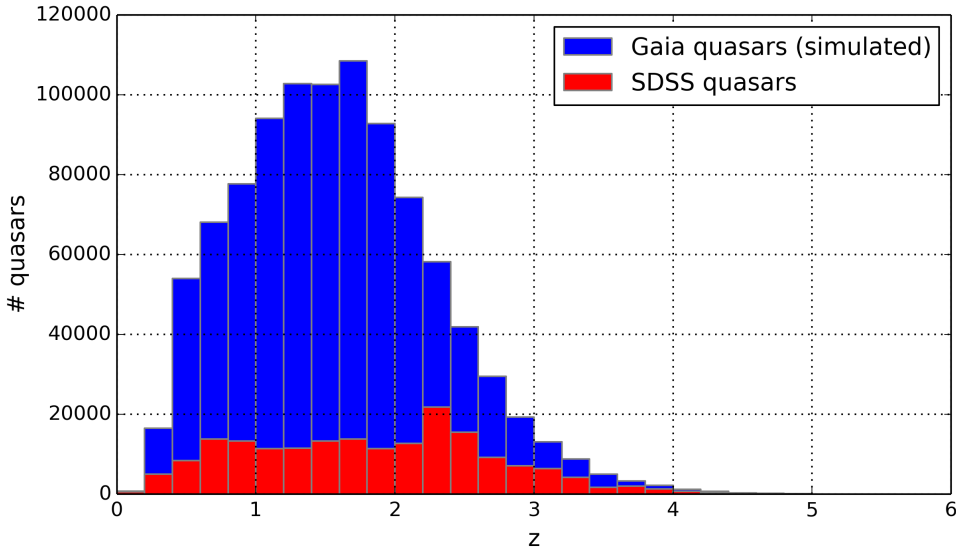
Figure 4.1: In the histogram we plot all known quasars from the SDSS survey in red. For this, we concatenate the objects from data release 7 together with the new quasars from data release 9. The different data releases are biased to certain quasar redshifts. In blue we show the quasar redshift distribution of simulated Gaia quasars presented in Robin et al. (2012). We see that the majority of Gaia quasars have redshifts between $1 < z < 2$.

took a while to form them.

In this chapter, we first present the magnitudes that we mainly use in this thesis and estimate correlations between these magnitudes. Then we use the composite quasar spectrum from VB2001 to simulate quasar low-resolution spectra considering Gaia's facilities (Section 4.2). Afterwards, in Section 4.3, we improve the quasar spectra for the blue and red photometers by selecting various redshifts and magnitudes. Typically quasar spectra show variable spectral lines and continua. Hence, in Section 4.4, we consider spectral variability in our simulations and investigate prospects to observe them with Gaia. In addition to low-resolution spectra, the Gaia satellite records a high-resolution spectrum for bright objects as well. In Section 4.5, we explore bright quasars that have broad emission lines in the radial velocity spectrograph and make a statement on potential variability measurements with Gaia. For completeness, we shortly summarize astrometric quasar analysis from literature together with our conclusions on their detectability with Gaia in Section 4.6. At the end of this chapter, in Section 4.7, we present a short conclusion of our quasar analysis.

We published most of the results on the investigation of quasars with Gaia in our paper Proft & Wambsganss (2015). From now on, we denote our paper as PW2015.

4.1 Magnitude Transformation Between G, V, and r'

In our work, we use three different photometric systems to indicate magnitudes of quasars. Gaia measures the magnitudes G, G_{RVS}, G_{BP}, and G_{RP}. In literature the quasar magnitudes are often given in Johnson magnitudes (U, B, V, R, I) or in SDSS magnitudes mentioned above. We derive rough correlations between the magnitudes V and G and between G and r' that we often use in our work. For this, we
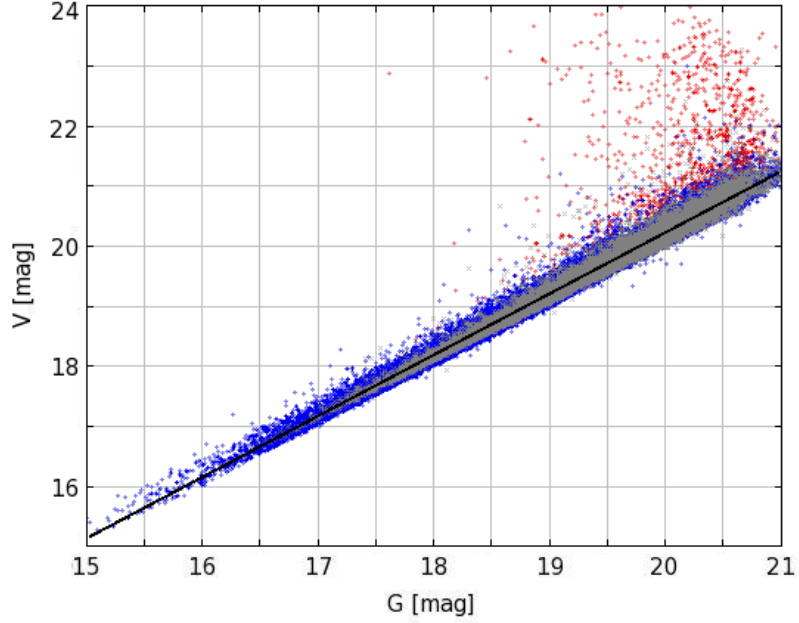
Figure 4.2: We show the Johnson magnitude V in dependence on the Gaia magnitude G for all SDSS dr7 quasars. The different colors represent three redshift intervals of the objects. Blue dots are quasars with redshifts $z \leq 2.1$, gray dots are quasars having redshifts between $2.1 < z < 4.0$, and red symbols indicate those quasars with large redshifts $z > 4.0$. The black line is a linear regression for $z < 4$ quasars.

first calculate V by using SDSS magnitudes following (Jester et al. 2005):

$$V = g' - 0.52(g' - r') - 0.03. \tag{4.1}$$

This equation has the smallest standard deviation ($\sigma = 0.05$) for $z \leq 2.1$ quasars. Then we derive G with SDSS magnitudes g' and i' (Jordi 2013):

$$G - g' = -0.1142 - 0.5216(g' - i') - 0.0835(g' - i')^2 + 0.0005(g' - i')^3, \quad (\sigma = 0.06). \tag{4.2}$$

Now we can plot V against G for all quasars from SDSS dr7 (Figure 4.2). We consider three redshift ranges: $z \leq 2.1$ (blue dots), $2.1 < z < 4.0$ (gray dots), and $z > 4.0$ (red dots) and make use of a linear regression (black line in Figure 4.2) for quasars with redshifts $z < 4$. The linear regressions for $z \leq 2.1$ and $z < 4.0$ quasars deliver similar results. We derive

$$V = 1.022 \cdot G - 0.244 \, \text{mag} \quad (\text{for } z \leq 4) \tag{4.3}$$

with a residual standard error of $\Delta V = 0.108 \, \text{mag}$. In the same way, we apply a linear regression for all SDSS dr7 quasars with calculated G magnitude (Equation 4.2) and available SDSS r' magnitude. We approximate

$$G = 0.973 \cdot r' + 0.390 \, \text{mag} \quad (\text{for } z \leq 3) \tag{4.4}$$

with a residual standard error of $\Delta G = 0.110 \, \text{mag}$.

23

4.2 Simulating Gaia's Low-Resolution Spectra of Quasars

4.2.1 Convolution of the Composite Quasar Spectrum VB2001

The first step to simulate quasar spectra is to convolve a realistic spectrum with a Gaussian kernel. As template we use the composite quasar spectrum from VB2001 because it shows the typical spectral features that are in general visible in all quasar spectra. The convolution of two functions $f\colon \mathbb{R} \to \mathbb{R}$ and $g\colon \mathbb{R} \to \mathbb{R}$ is defined as

$$(f \otimes g)(\lambda') = \int f(\lambda) \cdot g(\lambda' - \lambda) d\lambda. \tag{4.5}$$

In our setting, f assignes a wavelength λ to its flux density. Our choice of a gaussian kernel,

$$g(\lambda) = \frac{1}{\sqrt{2\pi\sigma^2}} \cdot e^{-\frac{1}{2}\left(\frac{\lambda}{\sigma}\right)^2}, \tag{4.6}$$

reflects that many emission lines have gaussian shapes. We only have discrete wavelengths values $\lambda_0, ..., \lambda_N$. Hence the integral in our convolution becomes a sum:

$$(f \otimes g)(\lambda_i) = \sum_{j=0}^{N} f(\lambda_j) \cdot g(\lambda_i - \lambda_j). \tag{4.7}$$

For a realistic spectrum we need to consider the spectral dispersion of the two photometers (BP and RP). The dispersion of both photometers strongly depends on the wavelength λ. The BP dispersion in the wavelength range of $3,300\,\text{Å}$ to $6,800\,\text{Å}$ increases from $30\,\text{Å}$/pixel to $270\,\text{Å}$/pixel. In the same wavelength range the line width in the BP changes from 1.3 to 1.9 pixel. The RP dispersion in the wavelength range of $6,400\,\text{Å}$ to $10,500\,\text{Å}$ increases from $70\,\text{Å}$/pixel to $150\,\text{Å}$/pixel. The corresponding line width in the RP varies between 3.5 and 4.1 pixel (de Bruijne 2012). Figure 7 in de Bruijne (2012) displays the exact distribution of the dispersion for both photometers. By using the program Dexter (Demleitner et al. 2001)[1], we extract the data points and interpolate the dispersion function necessary for our convolution. Additionally, we consider a linear interpolation of the line width and convert the FWHM to a standard deviation. Hence we use a standard deviation of

$$\sigma = \frac{\text{dispersion} \cdot \text{line width}}{2.35}. \tag{4.8}$$

4.2.2 Noiseless Low-Resolution Quasar Spectra

In the next step we apply the Gaia photon response from Jordi et al. (2010) to our simulation. A function that describes the photon response curve is not available and hence we fit the given data points. We plot our photon response curve fits in Figure 4.3. The upper panel shows the resulting fit for the BP in blue and the lower panel the fit function for the RP in red.

The VB2001 template considers a quasar redshift of $z = 0$. To simulate a spectrum with a certain redshift, we multiply the wavelength by the cosmological time dilation factor $1 + z$. By doing so, the spectrum is shifted to a higher redshift and it is stretched. At this point, we use the template with arbitrary flux density units. In the next section, when we simulate the spectra for different magnitudes, the flux density has to change as well. Due to the time dilation, the wavelength position for an individual

---

[1] http://dc.zah.uni-heidelberg.de/sdexter
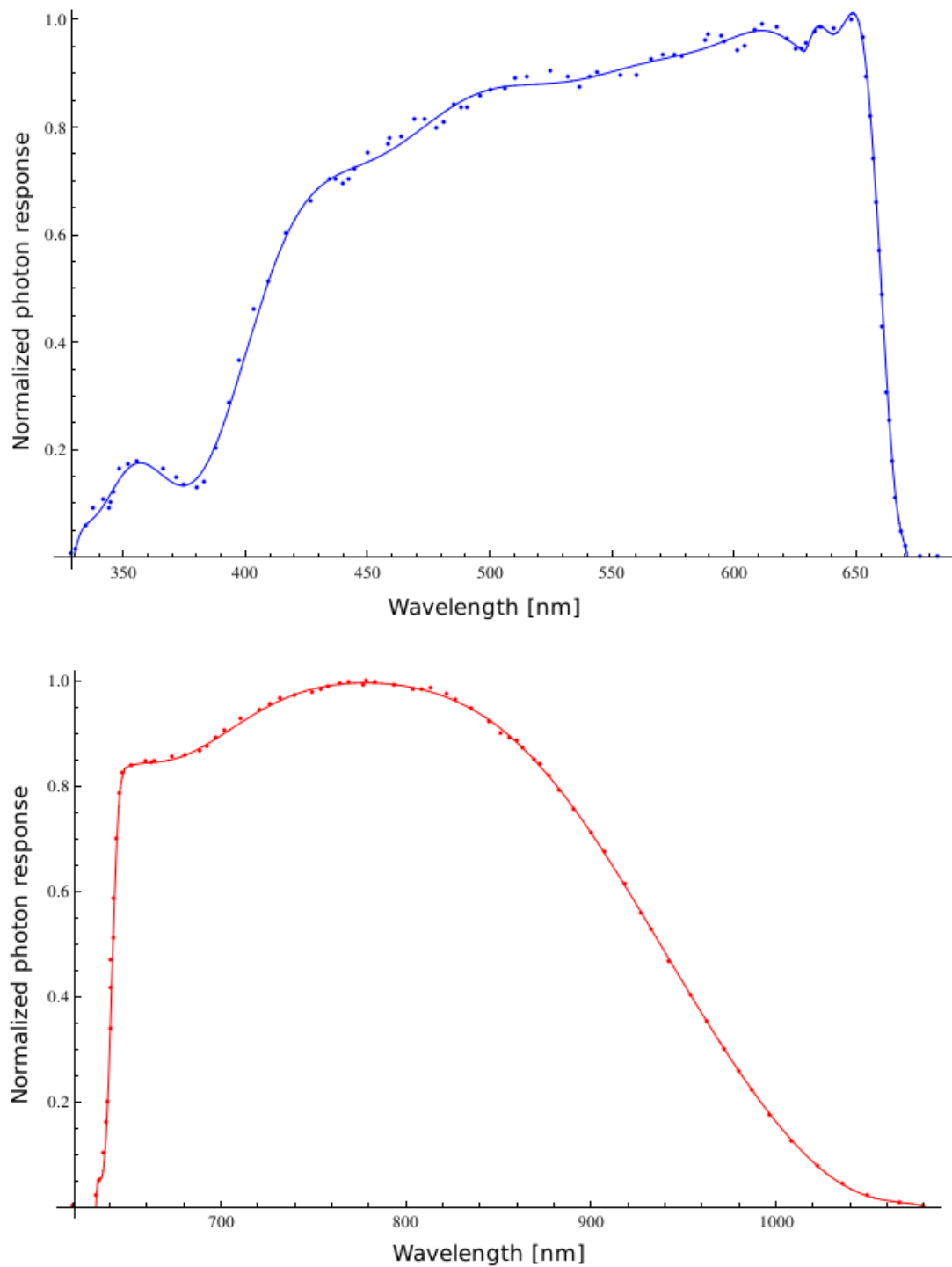
Figure 4.3: We interpolate the data of the photon response curve from Jordi et al. (2010). The top diagram shows our fitted photon response for the blue photometer and in the bottom diagram we fit the photon response for the red photometer. In the following simulations, we apply these photon response curves to every spectrum.
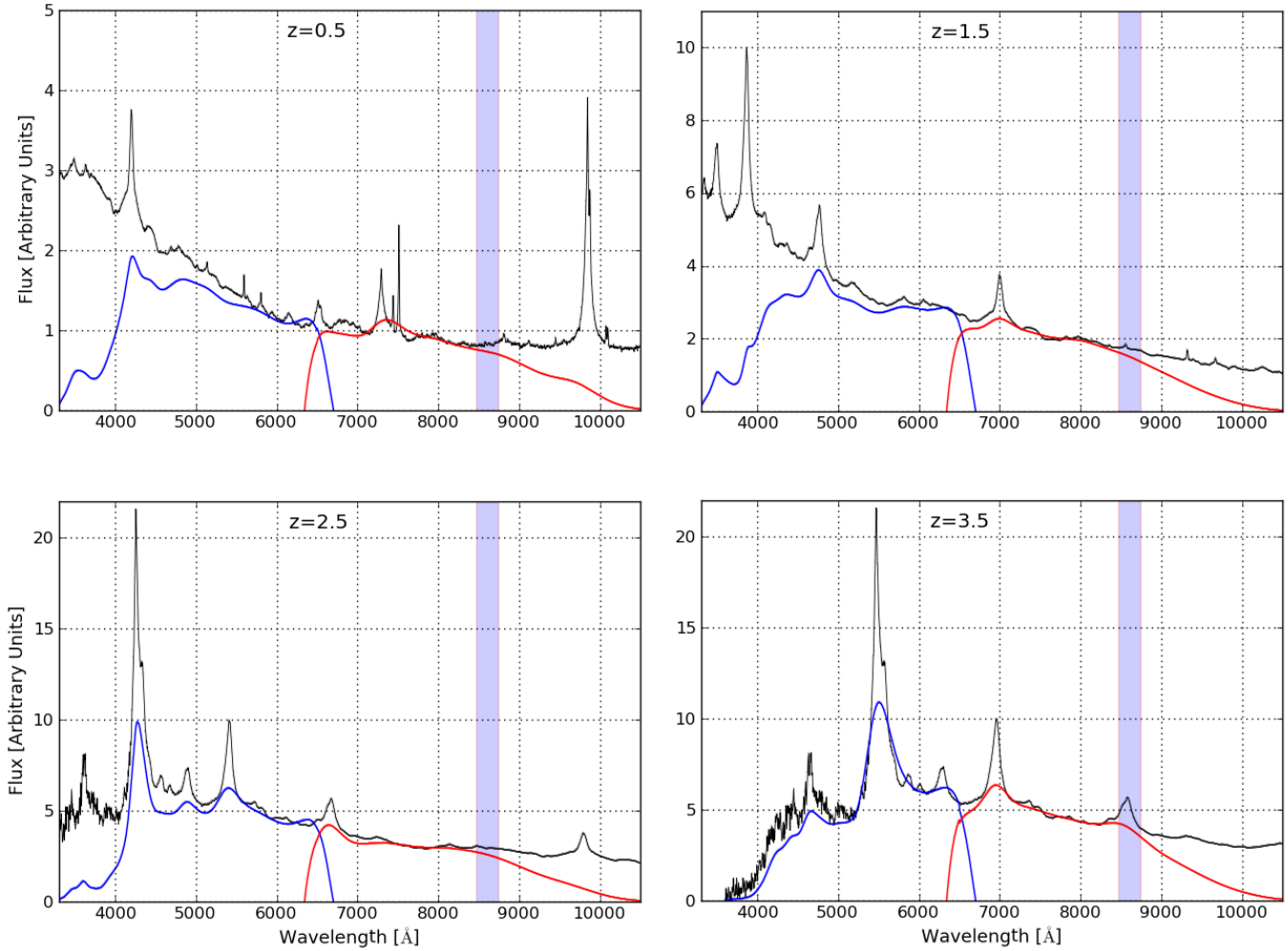
Figure 4.4: The four images show our simulated low-resolution quasar spectra in arbitrary flux density units considering Gaia's photon response curve and the redshifts $z = 0.5$, 1.5, 2.5, and 3.5. For a better visibility of the spectra, we adjust the flux density interval for every image. The full wavelength interval corresponds to Gaia's BP and RP measurements and the wavelength range of the blue shaded region defines the RVS high-resolution spectral area. The black curve is the VB2001 template spectrum at the corresponding redshift. The blue curve is the BP low-resolution spectrum and the red curve the RP low-resolution spectrum. Due to Gaia's photometer dispersions, the convolved BELs are broader than the template lines. The spectral dispersion strongly depends on the wavelength and hence this line broadening is different for distinct BELs.

26

			redshift		
BEL	0	0.5	1.5	2.5	3.5
Hα	6565	9858	16,413	22,978	29,543
Hβ	4853	7280	12,133	16,986	21,839
MgII	2800	4,200	7,000	9,800	12,600
CIII]	1906	2,859	4,765	6,671	8,577
CIV	1546	2,319	3,865	5,411	6,957
Lyα	1216	1,824	3,040	4,256	5,472

Table 4.1: We present the different wavelengths positions in unit Å of the BELs Hα, Hβ, MgII, CIII], CIV, and Lyα for the redshifts $z = 0$, 0.5, 1.5, 2.5, and 3.5.

BEL depends on the redshift. In order to identify the location for every BEL at distinct redshifts in our following figures (or outside of them), we calculate the wavelengths for the BELs Hα, Hβ, MgII, CIII], CIV, and Lyα for the selected redshifts $z = 0.5, 1.5, 2.5, 3.5$ and in the quasar rest frame ($z = 0$) in Table 4.1.

In Figure 4.4, we simulate our first low-resolution spectra of the VB2001 spectrum considering the photon response curve and four selected redshifts ($z = 0.5$, $z = 1.5$, $z = 2.5$, and $z = 3.5$). We plot the template spectrum at certain redshift in black, the low-resolution spectrum of the blue photometer in blue, and the low-resolution spectrum of the red photometer in red. Referring to both photometers, we select the wavelength interval to $3,300\,\text{Å} \leq \lambda \leq 10,500\,\text{Å}$. The blue shaded area indicates the wavelength range of potential high resolution spectra resulting from Gaia's radial velocity spectrograph ($8,470\,\text{Å} \leq \lambda \leq 8,710\,\text{Å}$). In our following spectra simulations, we always select the same wavelength intervals and always plot the template spectrum in black. We can see that the prominent features like the BELs or the "small blue bump" are still observable with Gaia. However, due to a changing spectral dispersion, the lines are broadened in a different manner for different wavelength areas. In case of redshift $z = 0.5$ quasars, MgII is visible in the blue photometer and the BELs Hα and Hβ in the red photometer. But because of the lower RP resolution at long wavelengths, Hα is hardly observable. In the second image ($z = 1.5$), we can still see the MgII and CIII] lines in the convolved spectrum but we can not see the CIV line which falls in the photon response curve gap around $3,800\,\text{Å}$. In $z = 3.5$ quasar spectra we clearly see the prominent lines Lyα, CIV and CIII]. At this redshift, MgII lies in the RP but is not measurable for the same reason as Hα in $z = 0.5$ spectra. In the last panel, $z = 3.5$, the BELs CIII], CIV, and Lyα are very prominent in the convolved spectra. Additionally, we can see that MgII falls in the high-resolution spectral range which we discuss later in Section 4.5.

In order to generate realistic quasar spectra, we have to consider noise in our simulations. Furthermore, Gaia does not produce a smooth spectral distribution like shown in Figure 4.4 but a spectrum that consists of 75 data bins. In the next section, we take the noise and data bins into account to qualitatively investigate quasar low-resolution spectra for different magnitudes and redshifts.

4.3 Realistic Low-Resolution Spectra of Quasars

4.3.1 Signal-to-Noise Ratio of the Blue and Red Photometers

In this section, we analyze the contributions of the signal-to-noise ratio (SNR) to Gaia's low-resolution quasar spectra. For this, we first analyze the paper by Carrasco et al. (2006). They derived the SNR per sample (Gaia term for data bins) for different magnitudes and various stellar types. In their calculations they had to consider several effects, for example, the total detection noise per sample, the calibration errors and the sky background contribution. They showed that for bright objects calibration errors have the strongest contribution to Gaia's BP/RP spectra and that the impact of further effects is negligible. Because the noise investigations are only done for stars, we choose a stellar spectrum that looks similar to a quasar spectrum in the low-resolution spectral range. But we have to keep in mind, even quasar spectra at identical redshift and magnitude could look very different from each other. Quasars with redshifts of $z \approx 2.5$ have similar spectral shapes as F stars. Therefore, we explore the F star SNR diagrams for the available magnitudes $V = 10, 13, 16 \, \text{mag}$ and the two calibration errors $\sigma_{\text{cal}} = 10$ and $40 \, \text{mmag}$. We compare the individual diagrams and recognize that the influence of calibration errors to faint objects with $V \gtrsim 16 \, \text{mag}$ (low SNR samples) is negligible. Hence for faint objects like quasars, one does not need to consider calibration errors. We calculate the number of known SDSS quasars brighter than $G = 16 \, \text{mag}$ by considering Equation 4.4. Only about 700 out of 184,000 quasars are brighter than this magnitude limit. In Carrasco et al. (2006) we find that the SNR per individual sample for F stars with a magnitude of $V = 16 \, \text{mag}$ and large calibration errors of $\sigma_{\text{cal}} = 40 \, \text{mmag}$ is approximately between 25 and 150 for BP and between 50 and 125 for RP. If we scale the SNR to fainter quasars, we find that photon (Poisson) noise from the quasar source is the major contribution visible in the spectra. In this case, the SNR is proportional to the square root of the flux (Bailer-Jones et al. 2008). For example, $G = 19 \, \text{mag}$ quasars have SNR that are about four times smaller than $G = 16 \, \text{mag}$ quasars. Hence for F stars or redshift $z = 2.5$ quasars, we estimate a SNR per data bin larger than four at 20th G magnitude (except for the first five bins with low photon response).

The photon noise exists due to the uncertainty of light. It implies that the number of light photons from an individual quasar varies even if the wavelength is the same. We can calculate the photon noise by the Poisson distribution

$$f(k, \lambda) = \frac{\lambda^k \cdot e^{-k}}{k!}, \tag{4.9}$$

which gives the probability of k photons falling in a wavelength interval λ. The flux density of our template VB2001 spectrum is given in arbitrary units. To convert the flux density in photons/Å, we first search for SDSS quasar spectra that have similar signatures as our template spectrum together with selected redshifts and a magnitude of $G = 18 \, \text{mag}$. We transform the SDSS magnitudes into Gaia's G magnitude by Equation 4.2. The chosen quasars are SDSS 155742.23+105615.6 ($z = 0.5$), SDSS 142658.98+520504.6 ($z = 1.5$), SDSS 121451.19+275309.1 ($z = 2.5$), and SDSS 082535.19+512706.3 ($z = 3.5$). Second, we convert the SDSS unit erg/s/cm^2/Å into photons/Å like explained on the SDSS III web page.[2] Third, we consider Gaia's single CCD exposure time of $4.42 \, \text{s}$ and the mirrow aperture of $1.45 \, \text{m} \times 0.5 \, \text{m}$ as described in Hestroffer et al. (2010). Furthermore, due to Gaia's scanning law, the objects always have a few subsequent passages on the CCDs within a few days. As a result of typically

---

[2]https://www.sdss3.org/dr9/algorithms/spectrophotometry.php#dr7

five individual exposures, we scale the exposure time by a factor of five to simulate one spectrum. But if we generate end-of-mission quasar spectra, we consider 72 combined field of view transits (Holl et al. 2012).

4.3.2 Low-Resolution Quasar Spectra for Different Redshifts

Following the procedure explained above, we plot various realistic low-resolution spectra with the VB2001 spectrum as template. First, in Figure 4.5, we select the magnitude $G = 18\,\mathrm{mag}$ and redshifts $z = 0.5$, 1.5, 2.5, and 3.5. For the simulated spectra we apply 37 data bins for the blue and 38 data bins for the red photometer instead of a smooth distribution (Brown 2006). The wavelength intervals and colors of composite, BP, and RP spectra in this and in the next diagrams are the same as used in Figure 4.4. Additionally, we apply five single field of view passages. In the plots we see that different BELs fall in the two photometric ranges of BP and RP depending on the selected redshift. At the chosen quasar magnitude and redshifts, we detect enough BELs to infer the quasar redshift. For such objects, which additionally have large equivalent widths BELs similarly to the VB2001 spectrum, it is easy to identify them as quasar from Gaia's BP and RP spectra alone. We emphasize that the bin widths increase with wavelength in BP and RP spectra. The bin widths of the BP (RP) spectra in our plots are roughly between $30\,\text{Å}$ and $240\,\text{Å}$ ($70\,\text{Å}$ and $140\,\text{Å}$). Therefore, the appearance of noise in our spectra depends on the wavelength.

Claeskens et al. (2006) present an extensive quasar redshift analysis with Gaia's previously planned photometers. However, they considered photometric systems which consisted of 5 broadband and 14 medium-band filters instead of the actual blue and red photometer. The authors found that due to the redshift dependent position of strong broad emission lines, it should be simple to infer the quasar redshift. Due to the changes of Gaia's photometry in 2007 (Jordi & Carrasco 2007), we do a qualitative redshift analysis by looking at five different redshift intervals. Similarly to Claeskens et al. (2006), we take into account that at least two broad emission lines should fall in the photometer wavelength range between $3,300\,\text{Å}$ and $10,500\,\text{Å}$ in order to calculate reliable quasar redshifts. For our redshift analysis, we simulate end of mission coadded low-resolution quasar spectra at magnitude $G = 20\,\mathrm{mag}$ and redshifts $z = 0.5$, 1.5, 2.5 and 3.5 in Figure 4.6. In Gaia's lifetime of five years, there are on average 72 observations of the two combined fields of view. In the appendix, we present the same coadded spectra but for interesting redshift values of $z = 0.15$, 0.35, 1.0, 1.2, 1.7, 2.0, and 2.3. In all of these figures, we use the same colors, axes, and intervals as shown in Figure 4.5. By shifting these generated low-resolution spectra between $z = 0$ and $z = 5$, we always observe two or more BELs in Gaia's BP or RP. However, the opportunity to calculate the redshift is different for diverse redshift regions. For redshifts smaller than $z \lesssim 0.4$, the line Hα is prominent and reliably measurable (Figures 8.1 and 8.2). In contrast, the following redshift interval ($0.4 \lesssim z \lesssim 1.2$) is the most complicated area. This is obvious, for example, in Figure 8.3 which shows the most difficult redshift $z \approx 1$. We can detect two BELs out of Hβ, MgII, and CIII], but no clearly detectable features. By additionally using Gaia's astrometry, one can identify these quasars and calculate their redshift. However, this redshift area is very sensitive to noise. In the redshift range $1.2 \lesssim z \lesssim 1.7$, we can prominently see two lines out of MgII, CIII],and CIV in our Figures 4.6, 8.4, and 8.5. Between $1.7 \lesssim z \lesssim 2.3$ the lines MgII, CIII], and Lyα are within the two photometers and the emission line CIV is very dominant. As example for this redshift interval, we show end of mission Gaia low-resolution spectra of a faint quasar with redshift $z = 2.0$ (Figure 8.6) and $z = 2.3$ (Figure 8.7) in the appendix. For large redshifts, $z > 2.3$, the emission line Lyα is dominant in BP or RP. Hence it is
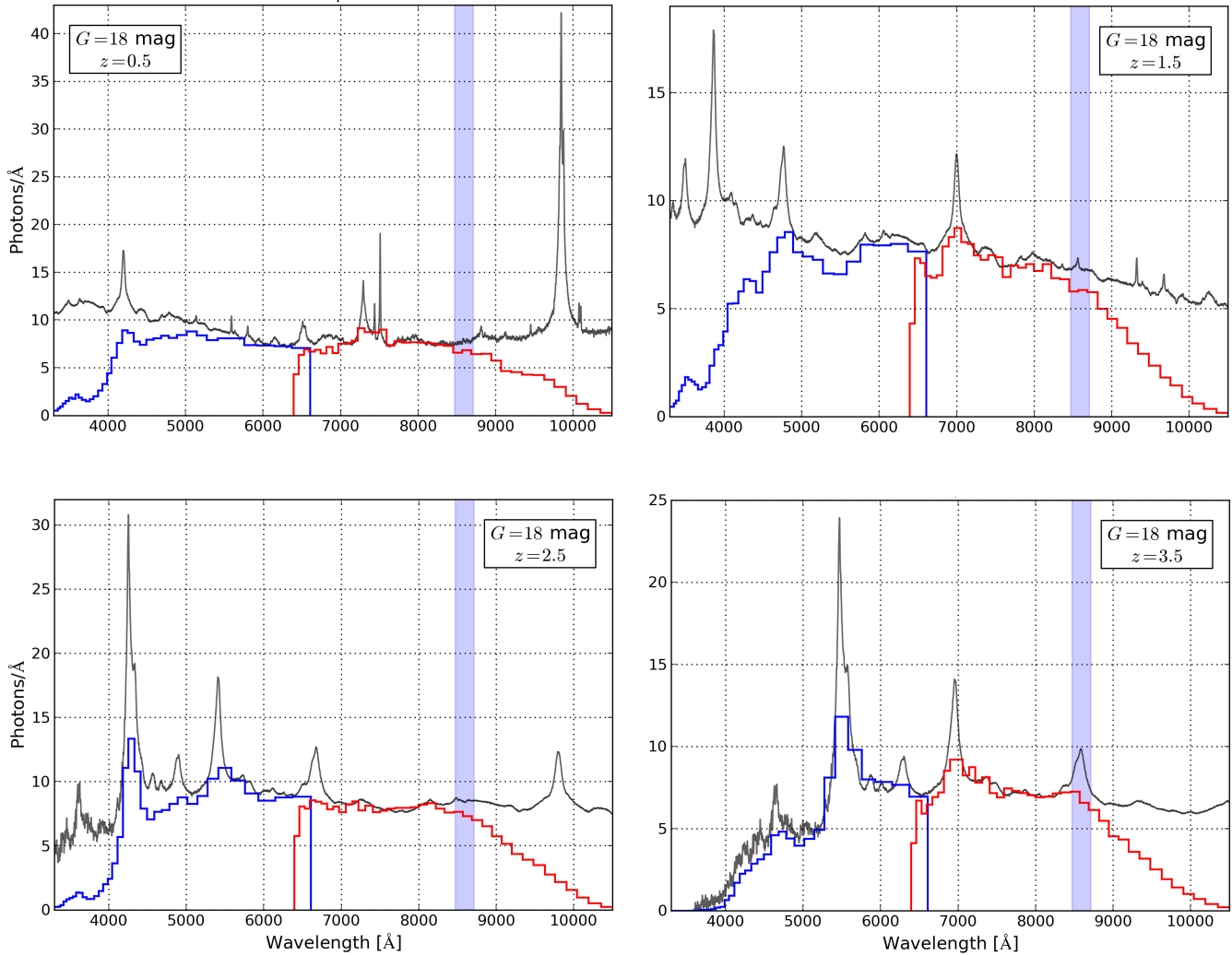
Figure 4.5: We show our convolved realistic low-resolution quasar spectra at fixed magnitude $G = 18\,\mathrm{mag}$ for redshifts $z = 0.5$, 1.5, 2.5 and 3.5. The different wavelength intervals and spectra with colors black, blue, and red are the same as in Figure 4.4. We take the photon noise into account and plot the flux densities in units photon/Å. For this, we considered the typical five single field of view transits in order to obtain the total exposure time. Once again, the flux density interval is different for the individual images. Additionally, we applied the 75 data bins, 37 for BP and 38 for RP. Plot from PW2015.
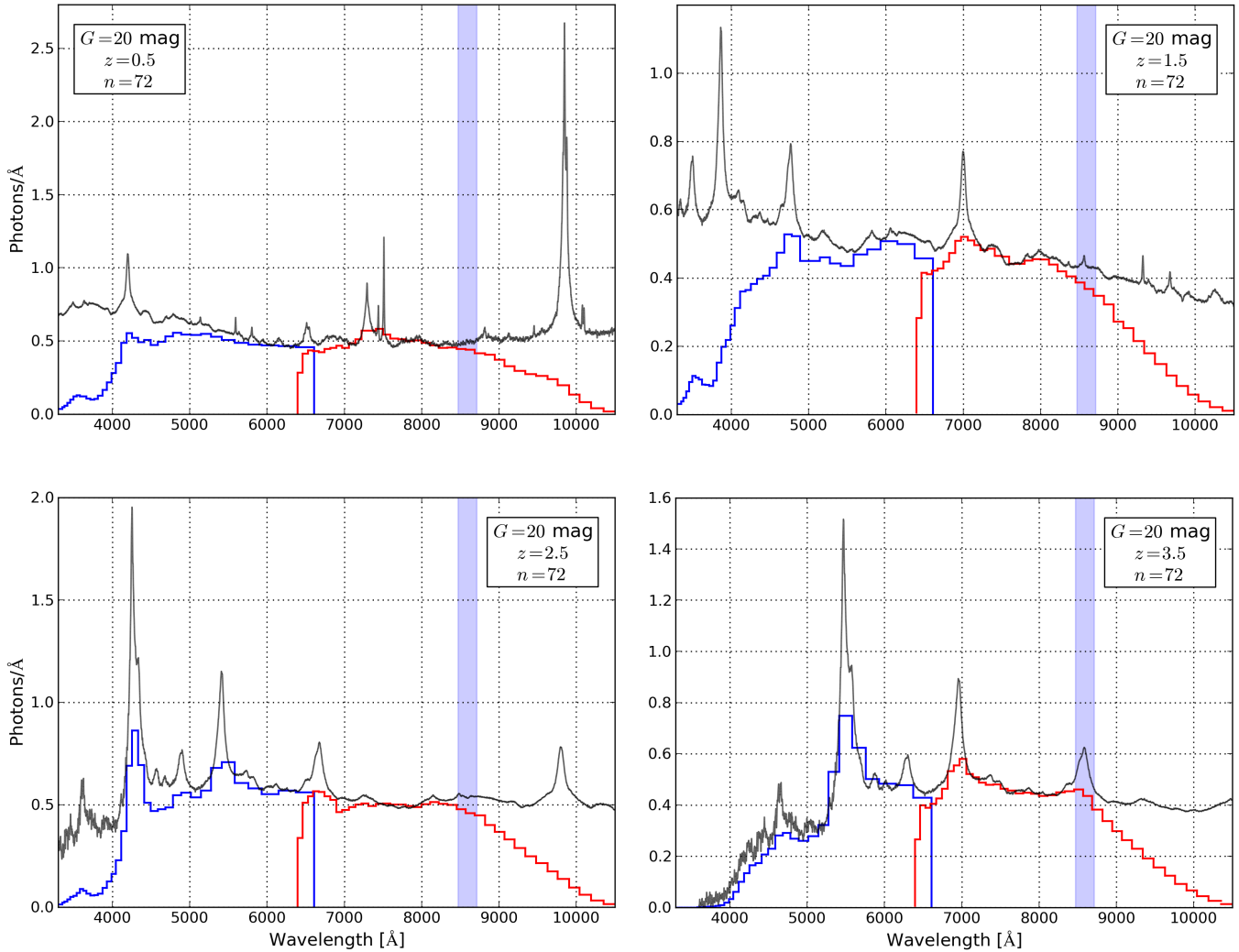
Figure 4.6: Plotted are the expected coadded end of mission low-resolution quasar spectra at magnitude $G = 20$ mag for redshifts $z = 0.5$, 1.5, 2.5, and 3.5. We select the same axes, colors, and intervals as shown in Figure 4.5. To account for five years of observations, we consider 72 measurements of the combined fields of view. We see that the feasibility to infer precise redshifts from Gaia's data depends on the redshift region. Plot from PW2015.

the easiest region to infer quasar redshifts, which we can clearly see in Figure 4.6 for redshifts $z = 2.5$ and $z = 3.5$.

For all of our Gaia spectra simulations, we use the VB2001 composite spectrum, but in reality the quasar spectra could substantially differ from this template. For example, redshifts of quasars with low equivalent width BELs are very difficult to determine especially at the faint end. For quantitative redshift studies, Claeskens et al. (2006) had to apply techniques like spectral principal component analysis or artificial neural networks on the previously planned photometric system. As mentioned before, the detectability of quasar redshifts is different for distinct redshift regions and in addition to this, it changes with magnitude. But the redshift errors are in general below $\Delta z = 0.1$ also for faint magnitudes (Delchambre 2014).

4.3.3   Low-Resolution Quasar Spectra for Different Magnitudes

In order to see the evolution of photon noise with decreasing brightness, we generate quasar spectra at fixed redshift but for the three magnitudes $G = 16\,\text{mag}$, $18\,\text{mag}$, and $20\,\text{mag}$. We transform the quasar flux density f related to the magnitude m by

$$m - m_0 = -2.5 \cdot \log \frac{f}{f_0}, \tag{4.10}$$

which results in $f_{20\,\text{mag}} = f_{18\,\text{mag}} \cdot 0.1585$ and $f_{16\,\text{mag}} = f_{18\,\text{mag}}/0.1585$, respectively.

First, we select a redshift of $z = 0.5$ in Figure 4.7. The following Figures 4.8, 4.9, and 4.10 present the same simulated BP and RP low-resolution spectra but for the fixed redshift $z = 1.5$, 2.5, and 3.5, respectively. In all four figures we can see that the noise level at magnitude $G = 16\,\text{mag}$ is very low. All BELs that are clearly detectable in the noiseless low-resolution spectra (Figure 4.4) are also obviously visible in these four plots. By increasing the magnitude to $G = 18\,\text{mag}$, we can see the higher noise level in all BELs and continua. However, we still can detect all prominent features by eye that are obvious in the corresponding noiseless spectra. But the last panel in the Figures 4.7, 4.8, 4.9, and 4.10 displays a strong noise level for magnitude $G = 20\,\text{mag}$. Some of the prominent spectral features are hardly visible by eye. For example, it is difficult to infer $H\beta$ in the bottom panel of Figure 4.7 or CIII] in the bottom panel of Figure 4.8 in comparison to the upper and middle panels.

In the next section, we simulate further low-resolution spectra with Gaia's BP and RP instrument to predict potential variability measurements with Gaia. Moreover, we simulate low-resolution spectra of variable SDSS quasars.

4.4   Studying Quasar Variability from Low-Resolution Quasar Spectra

4.4.1   Continuum and BEL Variability

In the last sections, we simulated quasar low-resolution spectra of Gaia's two photometers for different redshifts and various magnitudes. In order to make a statement whether individual BELs, spectral features like the "small blue bump" or variability within the features are detectable up to Gaia's magnitude limit ($G \approx 20\,\text{mag}$), we generate a number of noisy low-resolution spectra for a fixed magnitude and redshift. In this way, we can compare flux variations visible in individual samples. In Figure 4.11, we start with a quasar redshift of $z = 0.5$ and select four different magnitudes ($G = 16\,\text{mag}$, $18\,\text{mag}$, $19\,\text{mag}$, and $20\,\text{mag}$). In each panel, we show three simulated BP and RP spectra. Due to the photon noise, they are slightly different from each other. In every panel, we plot theses noisy quasar spectra for individual simulations in blue, red, and black. Apart from these representations, the axes and the plotted composite quasar spectrum are the same as used in the last diagrams. We consider five subsequent measurements to produce these individual quasar low-resolution spectra. The following Figures 4.12, 4.13, and 4.14 present the same approach but for redshifts $z = 1.5$, 2.5, and 3.5, respectively. When we compare the three low-resolution BP and RP spectra at magnitude $G = 16\,\text{mag}$ for every redshift (first panel in all four figures), we detect only small impact of the SNR to the individual samples in the spectra. All BELs, the "small blue bump" redshifted to around $6,000\,\text{Å}$ in Figure 4.12, and the continua are very similar to the noiseless spectra (Figure 4.4). By increasing the magnitude to $G = 18\,\text{mag}$, the SNR decreases substan-
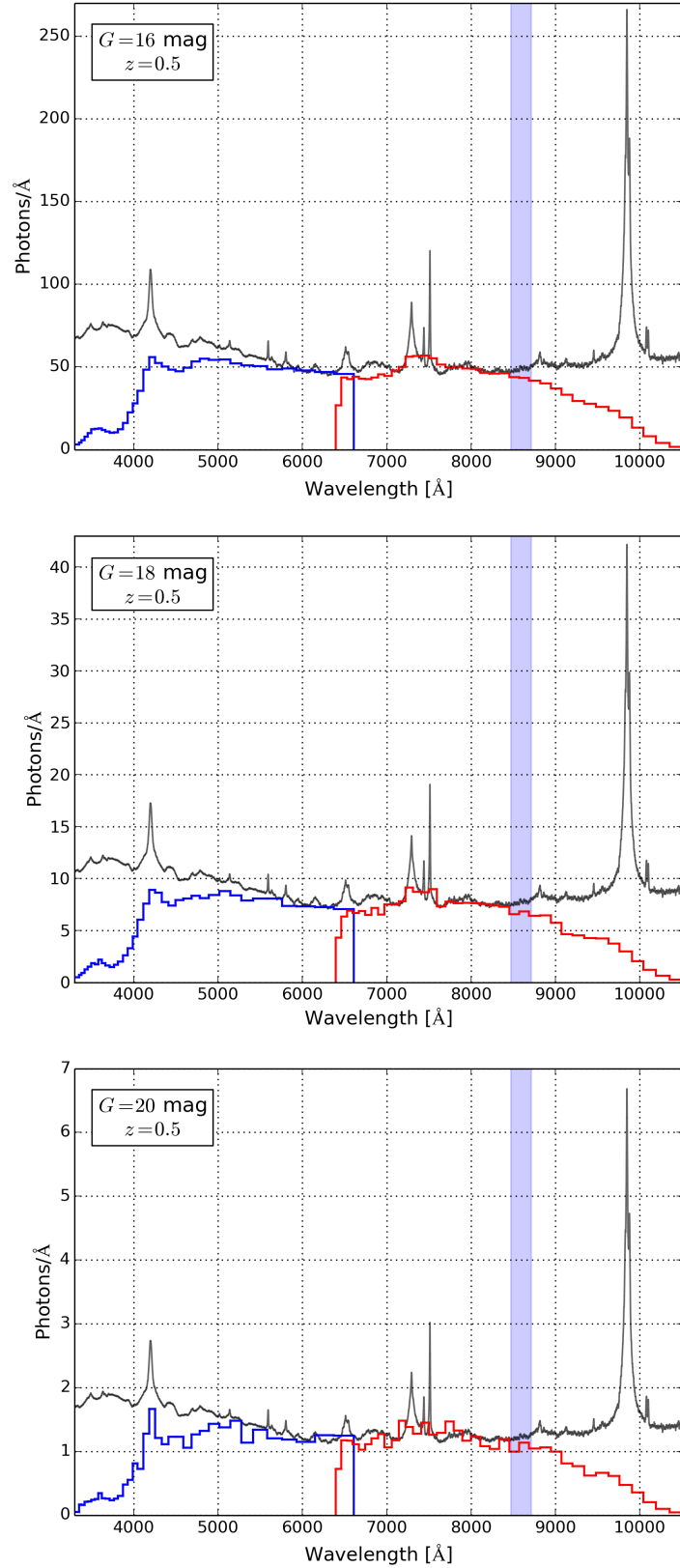
Figure 4.7: We show low-resolution quasar spectra at magnitudes $G = 16\,\text{mag}$, $18\,\text{mag}$, and $20\,\text{mag}$ for the redshift $z = 0.5$. We took the same data treated in the same manner as in Figure 4.4. The three panels show the tendency of increasing Poisson noise with fainter magnitudes.
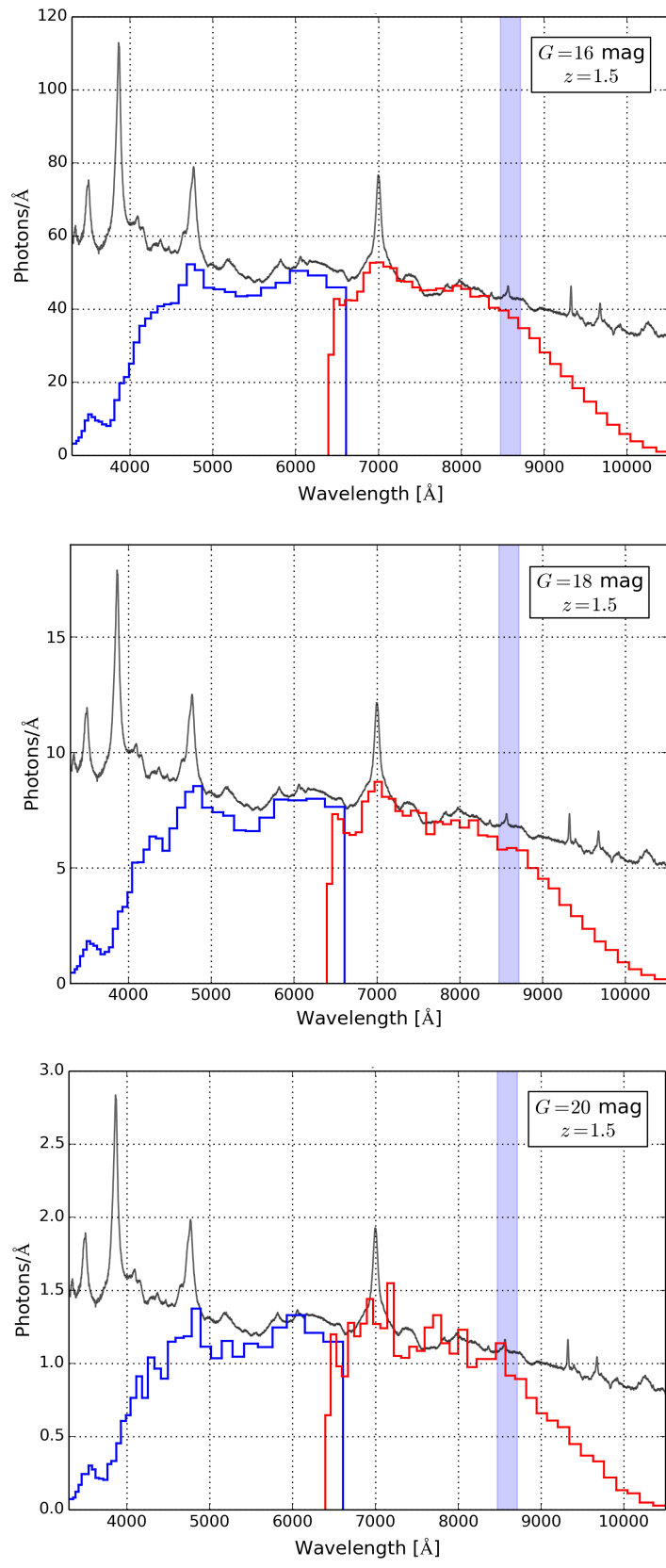
Figure 4.8: Same as Figure 4.7 but we considered a redshift of $z = 1.5$.

34
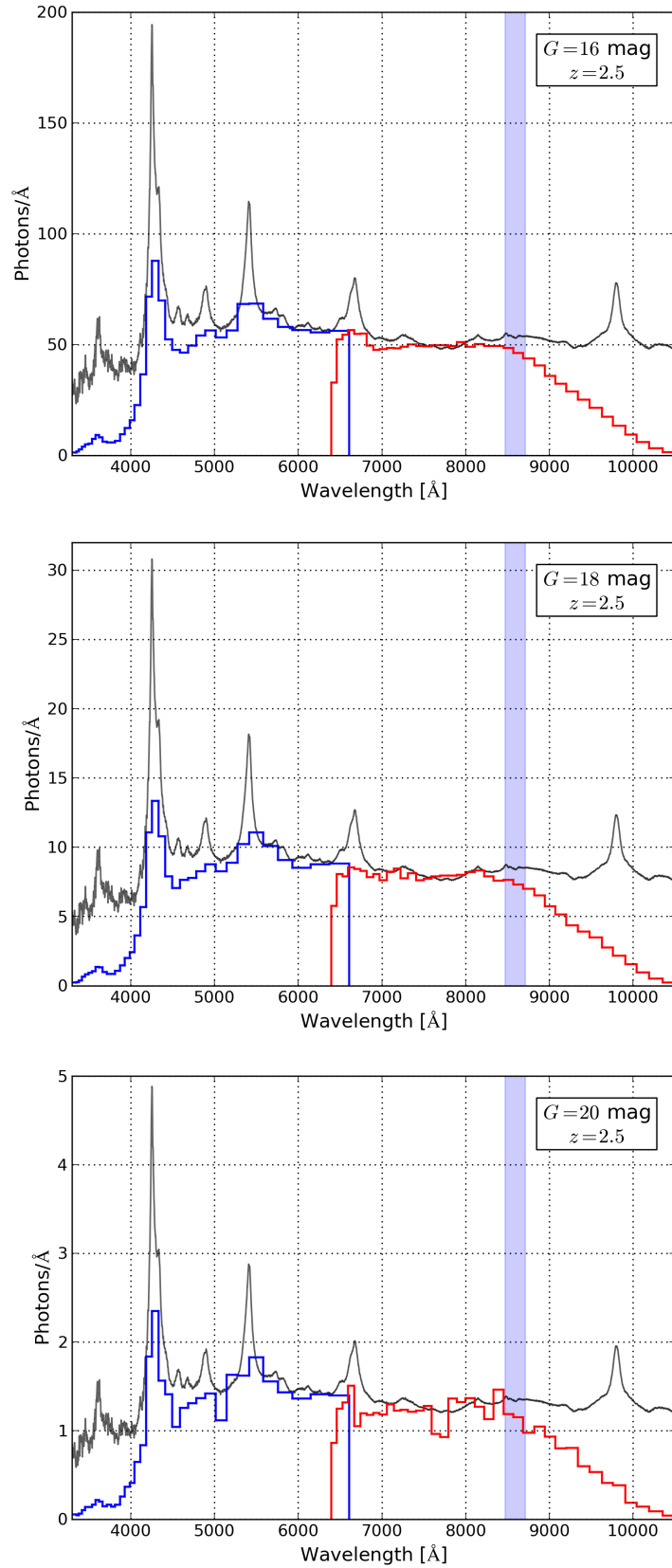
Figure 4.9: Same as Figure 4.7 but we considered a redshift of $z = 2.5$. Plot from PW2015.
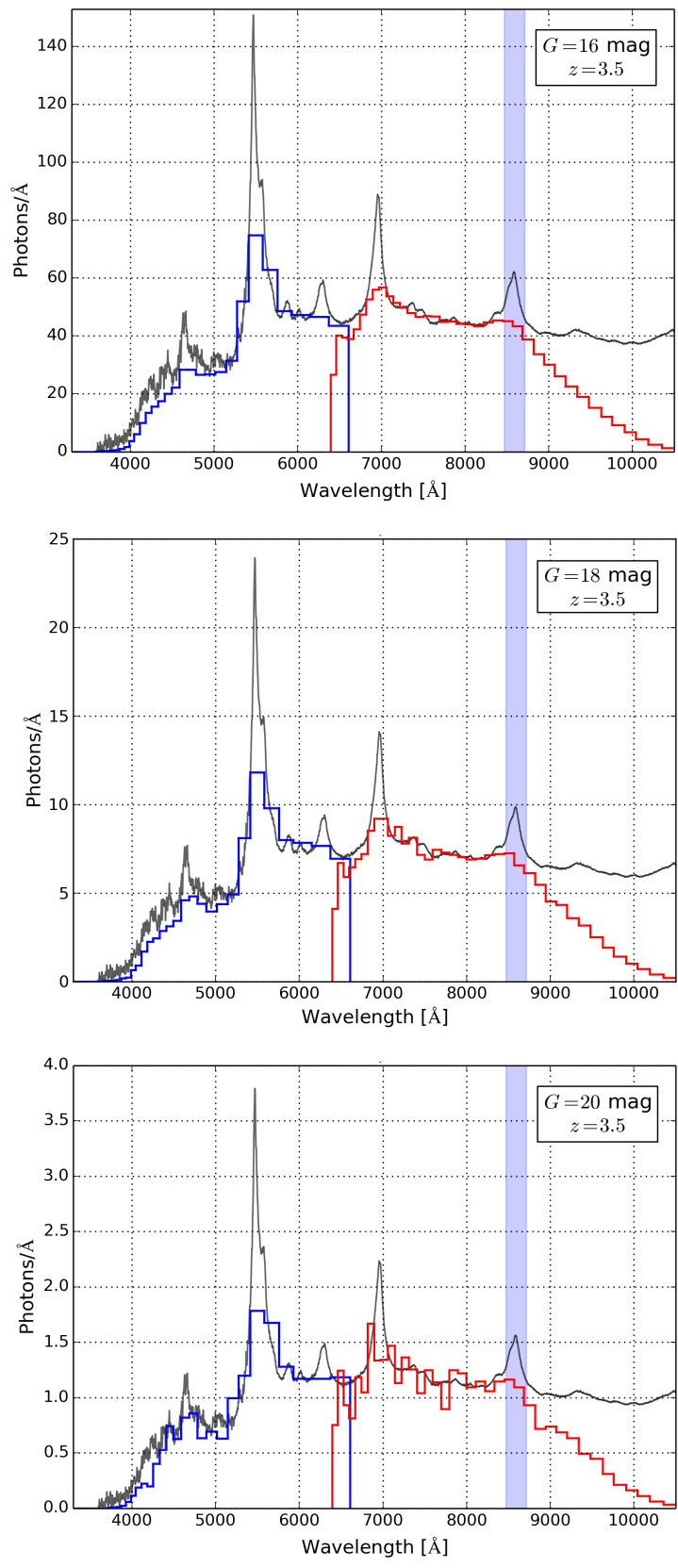
Figure 4.10: Same as Figure 4.7 but we considered a redshift of $z = 3.5$.

36

tially. For quasar spectra that are similar to this VB2001 template spectrum, the magnitude $G \approx 18\,\text{mag}$ represents a limit for reliable variability studies. In fact, we can detect all mentioned spectral features at $G \approx 18\,\text{mag}$. However, to investigate variability within the individual samples, we would need: (i) more subsequent measurements within a day or a few days, (ii) additional information from ground-based telescopes, or (iii) strong flux changes. We will discuss these three possibilities in the next subsections.

By increasing the magnitude to $G \approx 19\,\text{mag}$ and $G \approx 20\,\text{mag}$ (applied in all four figures), the SNR decreases significantly and variability studies of BELs or the quasar continuum are in general not possible for single spectra (five subsequent measurements). In these single spectra at a magnitude of $G = 20\,\text{mag}$ spectral features like the "small blue bump" or the MgII line, both visible in Figure 4.12, are hardly detectable. In the Figures 4.11, 4.12, 4.12, and 4.12, we additionally find that the variability study does also depend on the redshift and not only on the noise. At large redshifts, especially for $z \gtrsim 2.3$, strong BELs dominate the quasar spectrum and we have higher SNRs in BELs, for example, $\text{Ly}\alpha$. Additionally to the SNR and the redshift, the individual quasar spectrum can be very different to the template spectrum and its individual signals can have further influence on observable variability detections.

4.4.2 Variability Analysis with the Help of Convolved SDSS Quasar Spectra

In order to improve our predictions of continuum and broad line variability observable with Gaia, we study spectral changes of SDSS quasars. For this investigation, we search for bright SDSS quasars that have at least two variable spectra in the SDSS bulk search tool. We select 18 SDSS quasars that have redshifts between $0.3 < z < 3.5$ and magnitudes of $r' \leq 17.6\,\text{mag}$. All of them exhibit clear continuum variations like flux jumps or slope changes. We convolve each spectrum of every selected quasar in the same way as we treated the template spectrum above. By studying the multiple spectra of the 18 SDSS quasars in Gaia's low-resolution BP and RP range, we discover that Gaia is able to detect:

- strong continuum flux changes of $\Delta f = \dfrac{f_{\text{high}}(\lambda) - f_{\text{low}}(\lambda)}{f_{\text{high}}(\lambda)} > 5\%$ in each sample,

- strong changes in the equivalent widths of broad lines (dependent on the line and on Δf),

- strong slope changes (related to Δf),

for quasars brighter than $G = 18\,\text{mag}$. For strong BELs like $\text{Ly}\alpha$ the (flux dependent) SNR is higher than for weaker BELs like MgII and much higher than for BALs. Hence the accuracy of equivalent width measurements is dependent on the kind of line.

In Section 4.3.1, we determined that only about 700 quasars are brighter than $G = 16\,\text{mag}$. These 700 quasars have very high SNR and hence it is very likely that Gaia detects smaller flux changes even below 5% for many of them. Out of the 18 variable quasars, we show the two available spectra of SDSS 154757.71+060626.6 in the upper panel of Figure 4.15. This strongly variable quasar has a magnitude of $r' = 17.5\,\text{mag}$ and a redshift of $z = 2.03$. The spectrum in black represents the measurement in May 25, 2011, and the red signals show the observed spectrum in October 6, 2004. The bottom panel presents the convoled Gaia low-resolution spectra. We detect changes in the equivalent widths of broad absorption and broad emission lines in the low-resolution spectra of SDSS 154757.71+060626.6. Additionally, we observe strong variations up to $\Delta f \sim 20\%$ in its continuum. We conclude that Gaia can easily measure such kind of changes.
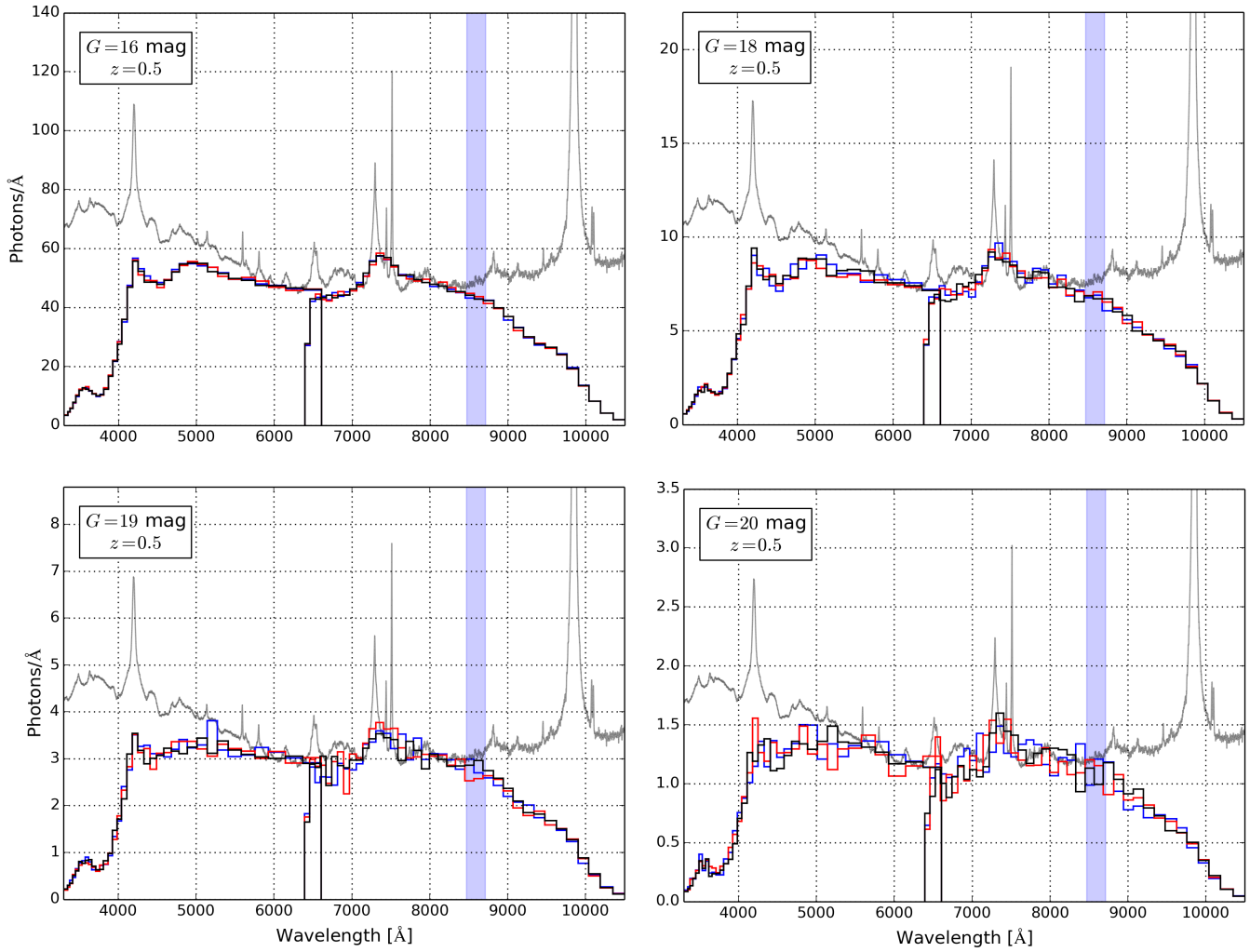
Figure 4.11: Similarly to Figure 4.7, we show our simulated low-resolution spectra at redshift $z = 0.5$ for different magnitudes. In this figure we select $G = 16$ mag, 18 mag, 19 mag and 20 mag. Additionally, we present three realizations of each spectrum to show the influence of noise to the individual spectra. We use different colors (blue, red, and black) together for the BP and RP spectra. The axes, wavelength ranges and the quasar template are the same as used above (e.g., Figure 4.7). In the four panels, we only see a small impact of noise at magnitude $G = 16$ mag, but a a strong influence at $G = 20$ mag.
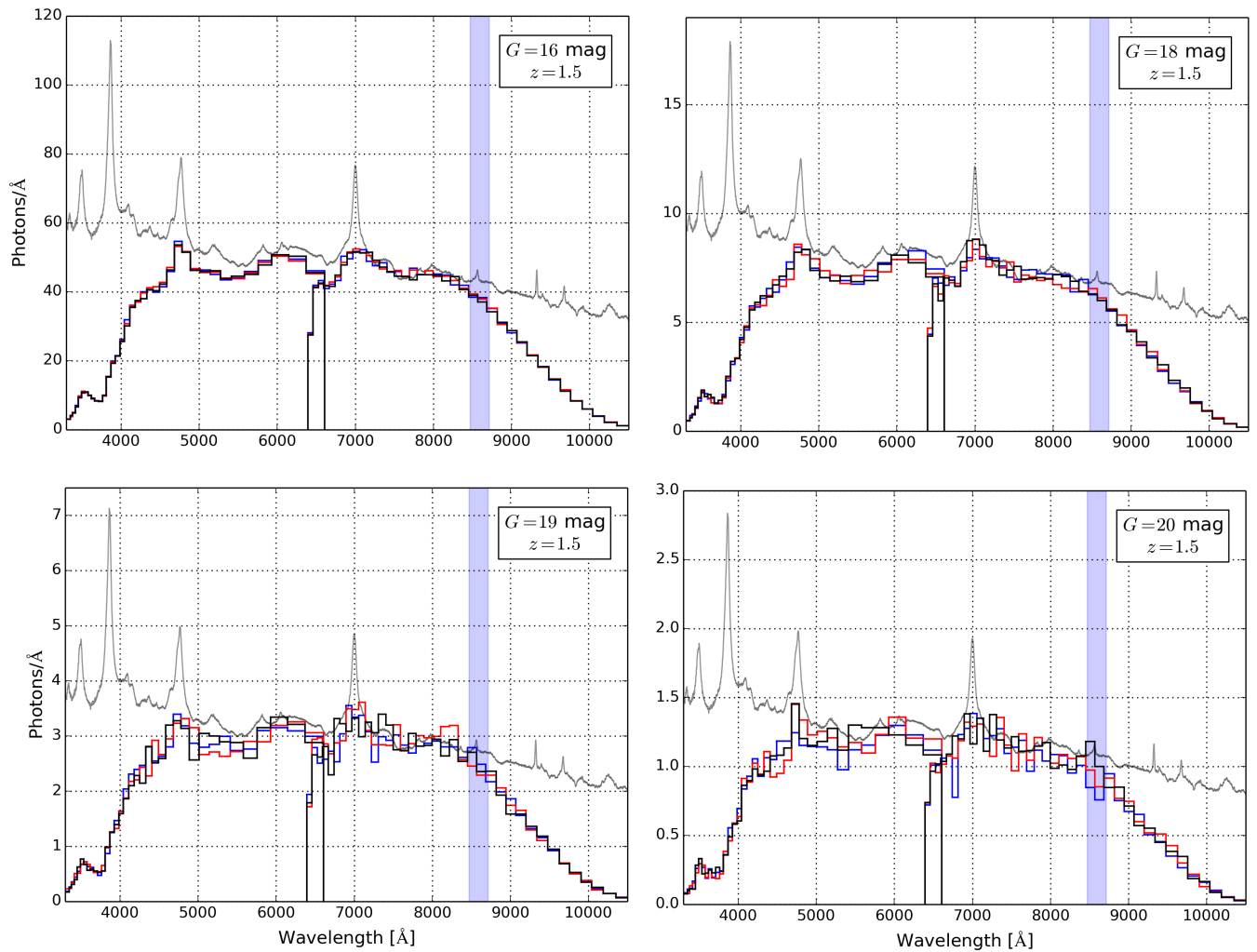
Figure 4.12: Same as Figure 4.11 but we considered a redshift of $z = 1.5$.
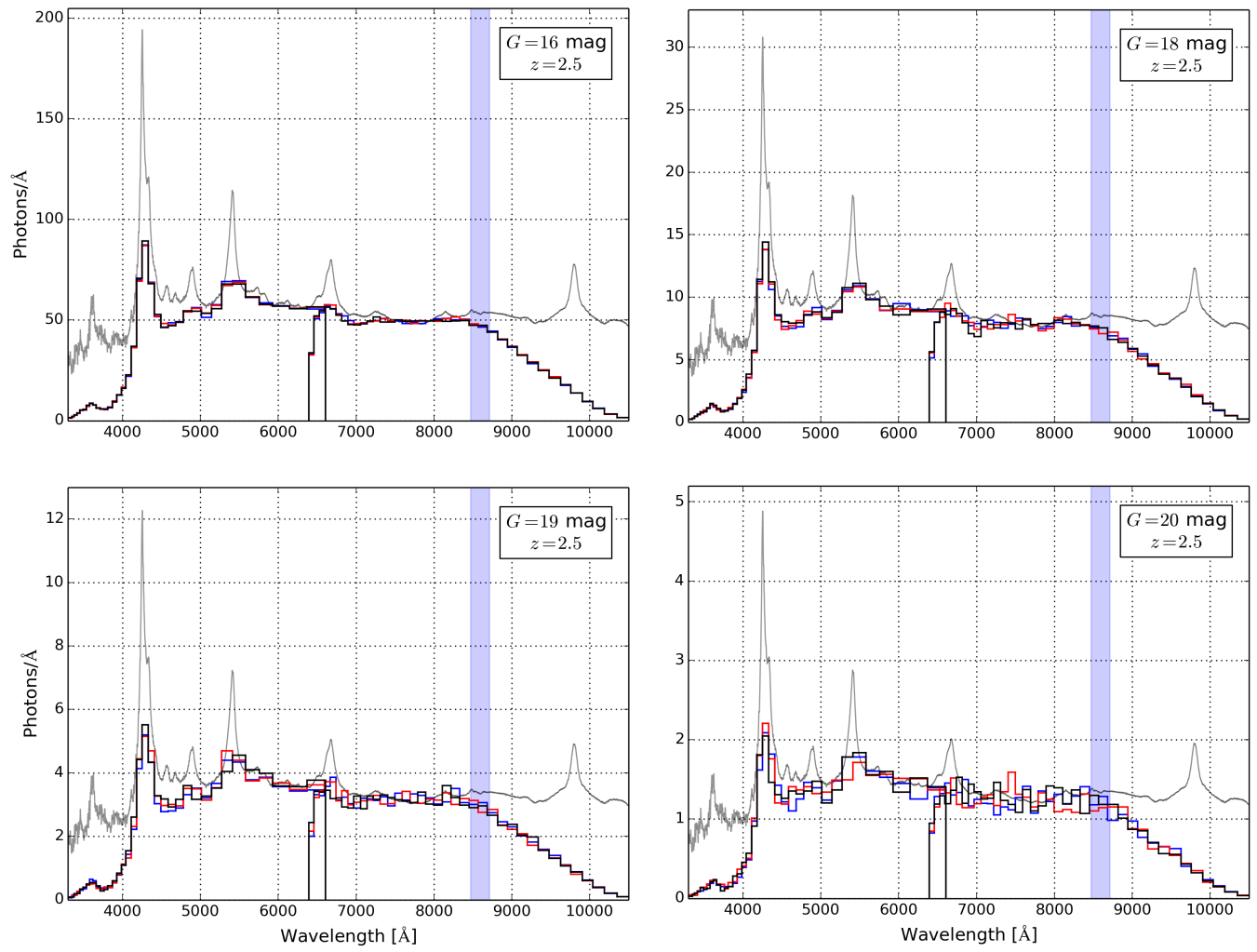
Figure 4.13: Same as Figure 4.11 but we considered a redshift of $z = 2.5$.
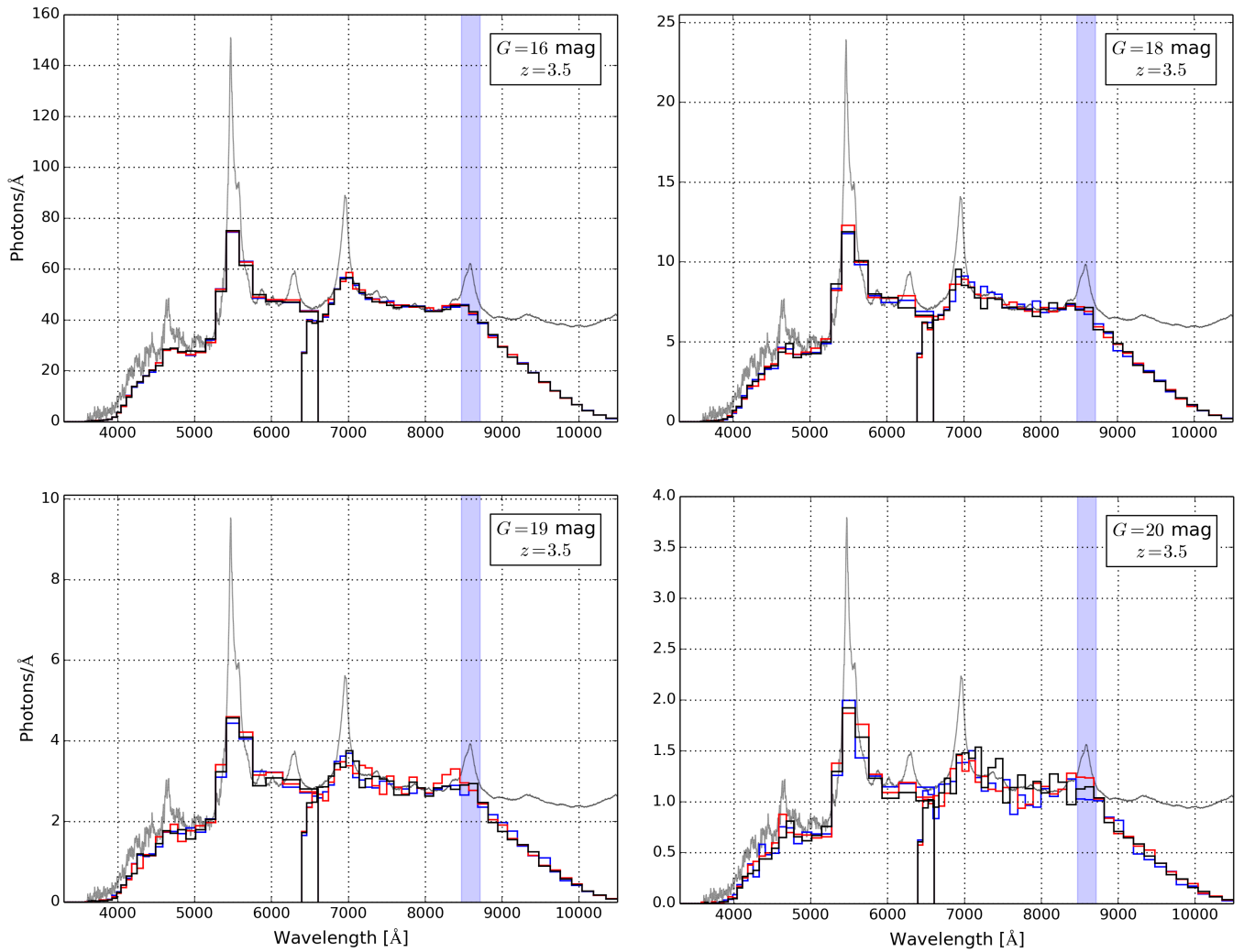
Figure 4.14: Same as Figure 4.11 but we considered a redshift of $z = 3.5$.
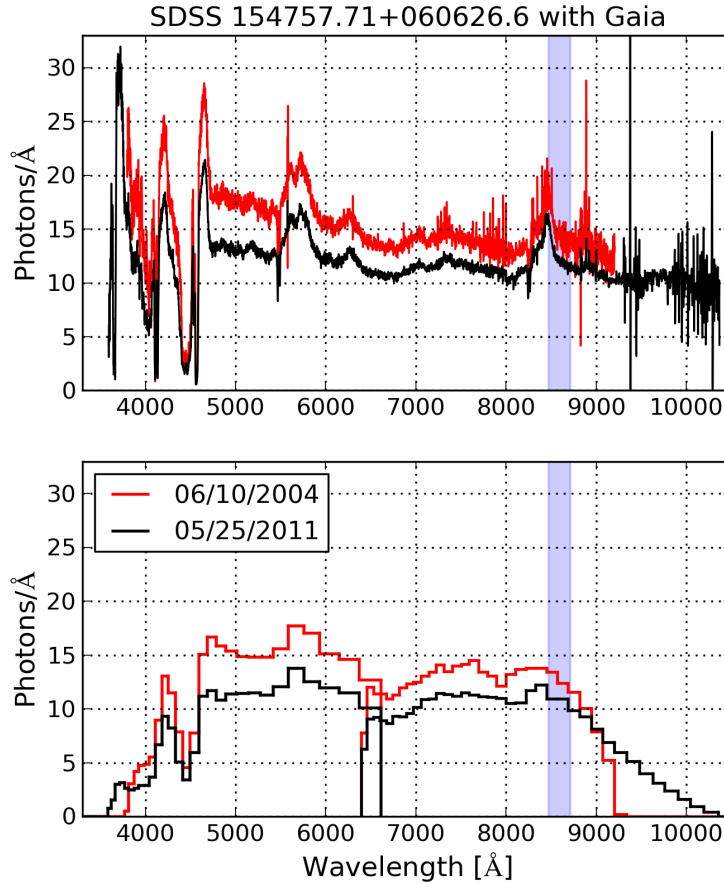
Figure 4.15: The upper panel shows the two spectra of quasar SDSS-15475771+0606266 at two epochs (red: October 6, 2004, black: May 25, 2011). In the bottom panel, we present the corresponding Gaia low-resolution spectra considering five single-field-of-view measurements and the photon noise. We see that Gaia can easily measure such strong spectral changes. Plot from PW2015.

4.4.3   Prospects of Quasar Variability Detections with Gaia

Short-Term and Long-Term Variability

In the last sections, we investigated continuum and broad line variability detections with Gaia. Apart from these spectral variations, we can also explore short-term and long-term variability. We define short-term variability as variations within a day or up to a few days and long-term variations as changes that we can observe within weeks or even years. In principle, Gaia could observe both, short-term and long-term spectral changes. However, Gaia's scanning law is not suitable to follow up intraday variability. After a few subsequent measurements of an individual object, the satellite has a measurement gap of typically two months. For short-term variability analyses, we would need quasars with high observational cadence that is obtained by many intraday observations. Furthermore, these quasar spectra have to exhibit large SNRs. To obtain sufficiently high SNR, the objects have to be brighter than $G = 18$ mag. In the last section, we simulated VB2001 low-resolution spectra for magnitude $G = 18$ mag. Theses spectra got sufficiently high SNR by combining five subsequent measurements that are typical for Gaia BP and RP measurements. When we study intra-day variability, we have to use single quasar observations and we only coadd two spectra (accounting for both fields of view). Apart from very large spectral changes ($\Delta f > 10\%$), the realistic quasar magnitude limit for intra-day investigations is $G \lesssim 16$ mag. The precise

magnitude limit for short-term variability investigations depends on the analyzed variability (continuum, BAL, or BEL changes) and on the quasar redshift.

Spectral changes of long-term timescales are easy to measure with Gaia. Especially long-term variability between two months and a few years is suitable to observe because of Gaia's scanning law. A promising small subsample of objects for exploring long-term variability are quasars at ecliptic latitudes around $\pm 45°$. These quasars have much more than the 72 observations that are typical within Gaia's lifetime. Although many of them have extra observations within a few days, some quasars will get additional measurements outside the intraday mode. An important application of quasars with this kind of information is a reverberation mapping campaign. In this scenario, we determine the time lag between BELs and continuum to study the broad line region of quasars (see Section 3.2.2).

Reverberation Mapping

As suggested by Watson et al. (2011), we could use a large (BEL) reverberation mapping campaign also to derive cosmological luminosity distances with the help of quasars or other AGN. The idea is that the luminosity of the quasar depends on the BLR size. If we are able to measure the time lag between continuum and BEL variations, we can infer the BLR size and hence the absolute quasar luminosity. In contrast to current distance measurements, we could reliably estimate the distance up to large redshifts of about $z = 4$. As explained in Section 3.1, we can infer the luminosity distance with the help of supernovae Ia only up to redshifts of $z \approx 1.7$. Additionally, it would be possible to check dark energy and different gravity theory options by the reverberation mapping approach. Czerny & Hryniewicz (2011) give a theoretical explanation of the relationship between the monochromatic flux of AGN and their BLR size. The time lag between BEL responses to continuum variations is typically of order weeks to months. But current or previous BEL reverberation mapping projects use data of high cadence, for example, every few days in order to reliably estimate its value. We already explained that, apart from the ecliptic poles, Gaia's scanning law is not ideal for this kind of frequent measurements. However, in some cases, the time lag is sufficiently high to be observable with Gaia. In fact, the observed time lag rises with redshift (Equation 3.14) and also with broad line region size. Furthermore, the BLR radii increase with quasar luminosity and for lower ionisation lines. The determination of time lags in quasar spectra is a difficult approach. In case of large redshifts, quasar magnitudes are often very faint which leads to small SNRs. On the other hand Kaspi et al. (2007) describe that quasars with large luminosities show only weak continuum changes and additionally have large redshifts (faint magnitudes). Still, very likely Gaia will be able to discover time lags at least for a small sample of quasars which very likely have high luminosities and large redshifts. The conditions which influence the success of reverberation mapping campaigns are the measurement accuracy, the mathematical method to calculate the time lag, and the chosen BEL (Czerny et al. 2013).

Another reverberation mapping approach is the scenario when the quasar continuum responds to variability within the continuum itself. The temperature of an accretion disk (blackbody) is a function of its radius $T \sim r^{-3/4}$. This accretions disk reprocesses the energy radiation of the central continuum source (Collier et al. 1999). Due to the reprocessing there is a time lag which is a function of the wavelength ($\tau \sim \lambda^{4/3}$). At large wavelength (8,000 Å) the time lag is only of order days (short-term variability) because of the small accretion disk dimension. If we can determine this time lag, we would be able to investigate the structure of the accretion disk and to calculate cosmological parameters (for example, the

Hubble constant). By using this method, Collier et al. (1999) suggest to measure luminosity distances to quasars or other AGN that are independent of the redshift. As explained above, to detect short-term variability with Gaia, we would need spectra with high SNRs and hence objects that are brighter than $G = 18$ mag or even brighter than $G = 16$ mag. Additionally, we can obtain more precise time lags when Gaia offers many intraday observations.

Analysis of Spectral Lines

In our work, the mainly analyzed spectral lines are BELs because they dominate quasar spectra and only about ten percent of quasars show some BALs. As described in Chapter 3, if a quasar shows strong broad absorption line characteristics like SDSS-15475771+0606266 in Figure 4.15, we can study quasar outflows. In addition to broad lines, quasar spectra show many narrow emission lines or narrow absorption lines. Due to the very low dispersion of Gaia's BP and RP spectra, we can not detect narrow lines in the low-resolution spectra. Hence we are not able to analyze these features with these two instruments.

There are further opportunities to analyze broad lines of quasars with Gaia's low-resolution spectra. We are able to determine the equivalent widths of broad emission and broad absorption lines as a function of time. The resolution of the low-resolution BP and RP spectra is only about ~ 100, but the equivalent width is independent of the resolution of the selected spectrograph. Therefore, we can derive the equivalent widths of quasar broad lines and with this, we are able to analyze the Baldwin effect. In contrast to the equivalent width, the FWHM of a spectral line is dependent on the resolution of the spectrograph. When we reliably want to estimate the FWHM of BELs in the blue and red photometers, the lines have to be at the wavelength location with the highest resolution. Both photometers (BP and RP) achieve the best resolution at their short wavelength range. Additionally, the FWHM has to exhibit a value of several 1,000 km/s. When we are able to approximate the FWHM, we can calculate the black hole mass by Equation 3.16. The FWHM as well as the equivalent width of BELs depend on the SNR of the low-resolution spectra. We can determine these two quantities for a magnitude limit of about $G = 18$ mag considering five subsequent measurements for the low-resolution spectra. When we are only interested in the end-of-mission FWHM or equivalent width, we can coadd the spectra and we will obtain reliably values also for faint $G = 20$ mag quasars.

4.5 Gaia's High-Resolution Quasar Spectra

In addition to the two low-resolution spectra, Gaia produces a high-resolution spectrum for bright objects but in a very small wavelength interval of $\Delta\lambda = 240\,\text{Å}$ between $8,470\,\text{Å}$ and $8,710\,\text{Å}$. The vast majority of quasars is too faint or have no prominent features in the wavelength range of the radial velocity spectrograph. However, for some bright quasars narrow or broad absorption lines and narrow or broad emission lines fall in the RVS. In such cases, the high-resolution spectra in principal allow to receive knowledge on the broad line region by investigating line variability and line profiles. This information is important because of the small BLR size. We can not spatially resolve the BLR with Gaia or other currently observing telescopes. In this section, we first analyze the profiles that we observe for quasar BELs. Then we explore the number of bright quasars that have lines in the RVS wavelength interval considering the SNR of the high-resolution spectra. Additionally, we study research prospects for these

BEL	Redshift z	Δz
Hα	0.291 - 0.326	0.035
Hβ	0.742 - 0.791	0.049
MgII	2.027 - 2.110	0.083
CIII]	3.440 - 3.565	0.125
CIV	4.480 - 4.633	0.153

Table 4.2: We list the five redshift intervals for which the BELs Hα, Hβ, MgII, CIII], and CIV are within the RVS wavelength range. The interval is stretched with increasing redshift due to the time dilation effect.

quasars. Before Gaia's commissioning and in the beginning of our work, a magnitude limit of $G_{RVS} = 17$ mag was proposed. Because of the mentioned stray light problem of the satellite, the actual limit is $G_{RVS} = 16$ mag. Due to this, we first present the comprehensive results for $G_{RVS} < 17$ mag and in addition to this, we explain our revisions for $G_{RVS} < 16$ mag.

4.5.1 Quasar Broad Emission Lines in the Radial Velocity Spectrograph

The most prominent BELs in quasar spectra are Hα, Hβ, MgII, CIII], CIV, and Lyα. By scaling the wavelength λ with the time dilation factor $1 + z$, we shift each of these lines in such a way that they fall into the RVS wavelength interval. We plot all six BELs from the VB2001 composite spectrum in Gaia's RVS wavelength range (blue shaded band) in Figure 4.16. To optimally see the individual lines in the diagrams, we scale the flux in every panel differently. The line shapes of all six BELs are distinguishable from each other. For example, obscuration effects, the geometry of the BLR, cloud velocities, and superimposed BELs from distinct quasar areas influence the different BEL profiles (Kollatschny & Zetzl 2013). We can explain the Gaussian shape of many line profiles by the Doppler effect. For example, Peterson & Wandel (1999) describe Gaussian profiles by rotational motions of the BLR clouds which emit the emission lines. Otherwise, Blumenthal & Mathews (1975) explain Logarithmic line profiles by outflowing gas. Moreover, Goad et al. (2012) interpret Lorentzian line shapes by turbulent motions in the outer accretion disk. Hence various velocity components influence the observed line shapes. If one can measure the ration between turbulent motion and rotational velocity, it is possible to estimate the thickness of the accretion disk (Kollatschny & Zetzl 2013).

We find that quasars with Lyα in the RVS interval would have a redshift of about $z = 6$. However, it is very unlikely that Gaia measures a very bright quasar ($G_{RVS} < 16$ mag) at such a large redshift. Hence we do not consider this BEL in our following studies. For the other five emission lines, we give the wavelength interval for which the BEL maxima always are within the blue shaded band (Figure 4.16) in Table 4.2. Additionally, we list the increasing interval width in the table to show the effect of time dilation with redshift.

4.5.2 The Signal-to-Noise Ratio of RVS Spectra

In order to investigate variability of spectral lines in the RVS, we have to consider the SNR of its high-resolution spectra. We want to determine the SNR in dependence on quasar brightness when Hα, Hβ, MgII, CIII], or CIV fall into the RVS. For this, we consider a diagram of the SNR per sample (Gaia term
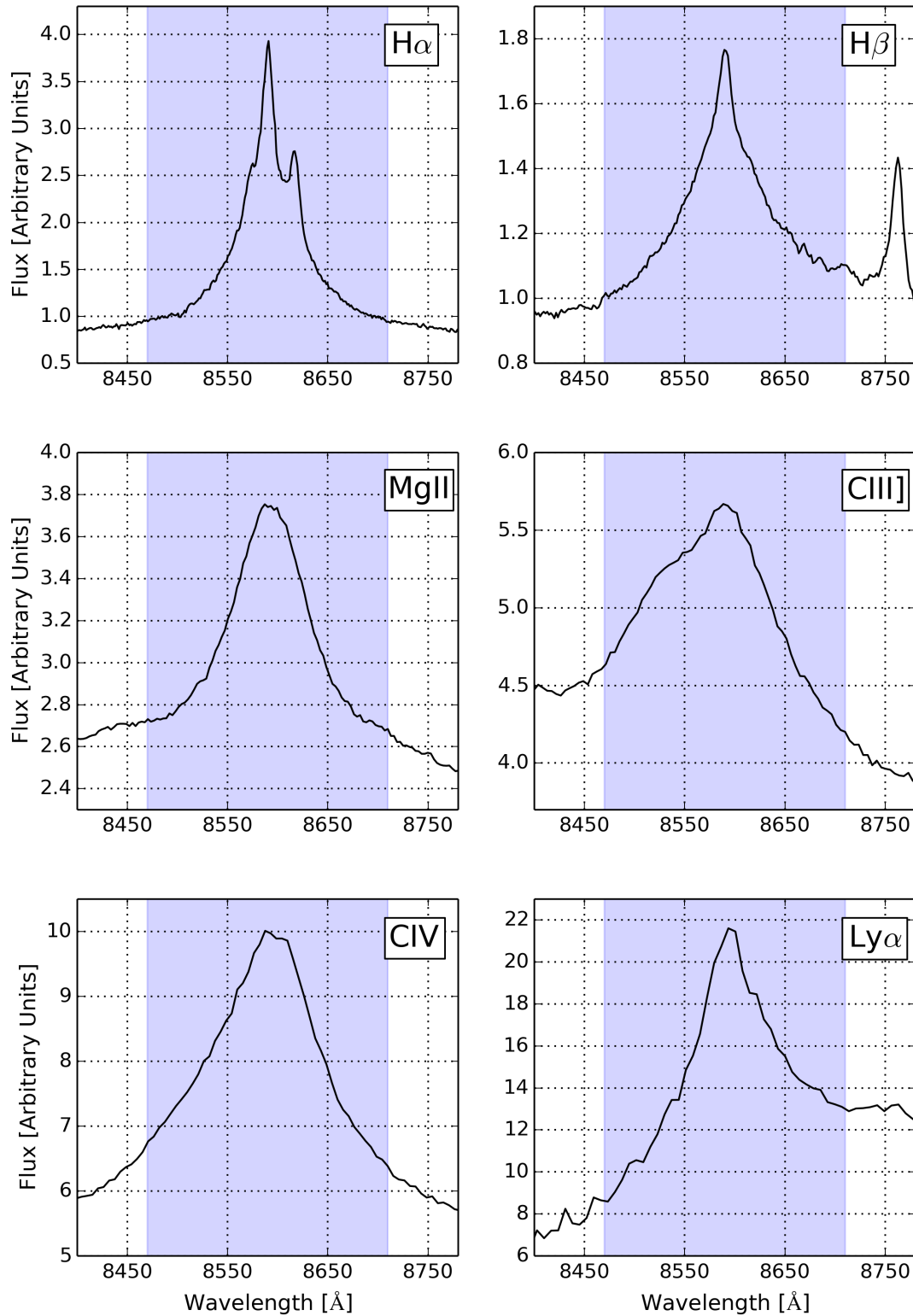
Figure 4.16: The six diagrams show the spectra of Hα, Hβ, MgII, CIII], CIV, and Lyα of the VB2001 template in Gaia's RVS wavelength range (blue shaded area). We adjust the arbitrary flux units in such way that the individual BELs are optimally visible. We can see that the line profiles are very different from each other.
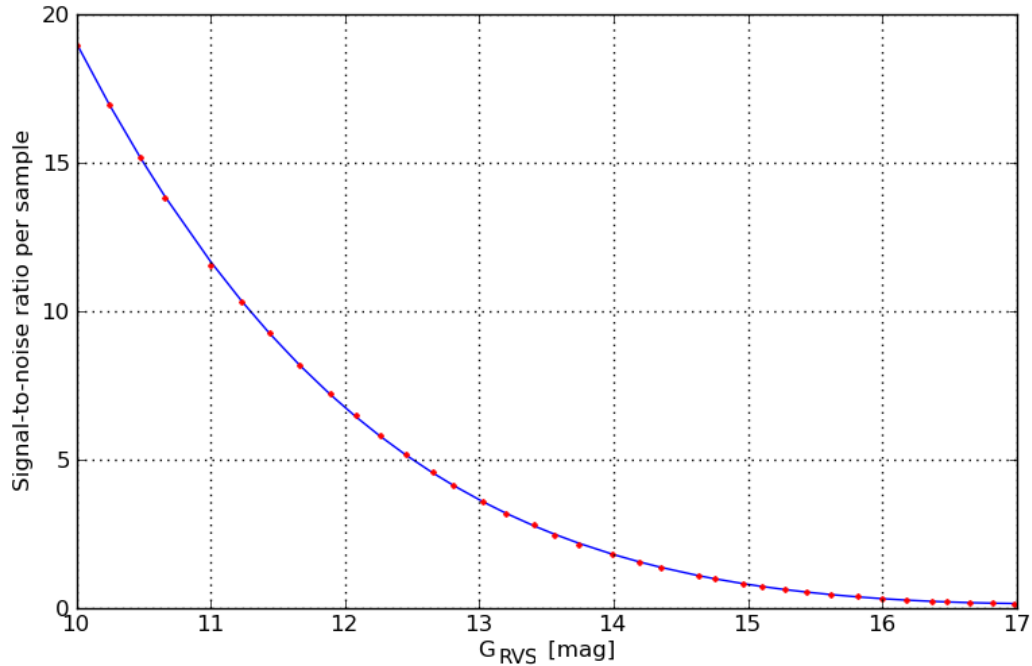
Figure 4.17: We plot the SNR per sample (single CCD) of stellar continuum level spectra as a function of magnitude G_{RVS}. The red dots are data points that we determine by the help of Dexter from the original plot[3]. Additionally, the blue line is our fit of the data. The diagram shows that the SNR per samples for $G_{RVS} > 15$ mag and for single CCDs is smaller than one.

for data bins) of single CCDs as a function of G_{RVS}. This SNR data is given for the continuum level of stellar spectra on the Gaia web page[4]. We fit these SNR data and present the resulting plot in Figure 4.17. It is visible that the RVS has a very low SNR per sample (single CCD) of less than one for objects fainter than $G_{RVS} \approx 15$ mag. However, the RVS covers about 1,000 samples and we can obtain much higher SNRs when we rebin the samples that comprise the individual quasar lines. If a broad emission line falls in the RVS wavelength range, the signals are very different to a continuum. But a continuum was assumed for the plot, that we show in Figure 4.17. We have to apply an approximation in order to make conclusions on the SNR for quasar lines in the high-resolution spectrum. Our idea is to assume a constant SNR in the FWHM of the selected spectral line and to rebin the samples that cover the FWHM of a spectral line.

The FWHM of each considered BEL and hence also the number of samples that cover the FWHM is different. Therefore, we count the samples for every BEL-FWHM using the VB2001 template spectrum at individual BEL redshift. We consider that, similarly to the quasar spectrum, the FWHM of every spectral line increases with redshift:

$$\text{FWHM}(z) = (1+z) \cdot \text{FWHM}(z=0). \tag{4.11}$$

The values of the FWHM($z=0$) are available in VB2001 for every BEL. Furthermore, we infer the expected magnitude ($m_{\text{FWHM,line}}$) in the five different FWHM(z) using the (magnitude transformation) Equation 4.10. For this, we calculate Vega's flux as reference f_0 in the FWHM wavelength interval for all five BELs. Although a quasar would have a magnitude of $G_{RVS} \approx 17$ mag, the magnitude in the

---

[4]http://www.cosmos.esa.int/web/gaia/snrwithoriginal, accessed on April 1, 2016.

emission line peak (we use the FWHM wavelength interval) is always brighter than G_{RVS}. Because the VB2001 spectrum has arbitrary flux units, we select several SDSS quasars with magnitudes between $14 \lesssim G_{\mathrm{RVS}} \lesssim 17$ for each BEL redshift to scale the template flux. Now we convert the FWHM magnitude of the BELs to their instrumental RVS magnitude by

$$G_{\mathrm{RVS}} = m_{\mathrm{FWHM,line}} + \Delta m_{\mathrm{FWHM,line}}. \tag{4.12}$$

We estimate magnitude differences $\Delta m_{\mathrm{FWHM,line}}$ to 0.81 mag (Hα), 0.36 mag (Hβ), 0.35 mag (MgII), 0.04 mag (CIII]), and 0.09 mag (CIV). The magnitude transformation is necessary in order to infer the values of the SNR per sample SNR$_s$ in Figure 4.17. Now we can calculate the SNR in the FWHM for the five emission lines by

$$\mathrm{SNR}_{\mathrm{FWHM,BEL,1}} = \sqrt{3} \cdot \mathrm{SNR}_s \sqrt{\#s}. \tag{4.13}$$

The quantitiy #s is the number of samples covering the FWHM. The factor $\sqrt{3}$ accounts for the three CCDs in the along-scan direction of the RVS that measure spectra for every single observation. In Figure 4.18, we plot our calculated SNRs of broad emission line FWHM against the RVS magnitude G_{RVS}. In this process, we present the results for Hα (blue dots), Hβ (red triangles), MgII (green pluses), CIII] (purple crosses), and CIV (black squares) individually. The vast majority of quasars with BELs are fainter than $G_{\mathrm{RVS}} = 15$ mag. Hence we only show these SNRs for magnitudes between $15 \, \mathrm{mag} \leq G_{\mathrm{RVS}} \leq 17 \, \mathrm{mag}$. The SNR results are slightly different for the distinct BELs. At the faint end, all SNRs are only between five (Hβ) and seven (CIV). The SNR increases to twelve (Hβ) until sixteen (Hα) at magnitude $G_{\mathrm{RVS}} = 16$ mag. For bright quasars with $G_{\mathrm{RVS}} = 15$ mag the SNRs of all BEL-FWHM are at least thirty. Hβ shows the smallest value of the SNR because this line has the smallest equivalent width.

In the following, we determine the SNR in the FWHM by following an alternative approach to confirm our previous approximations. In this way, we calculate the SNR initially in every sample for every BEL. Then we determine the SNR in the FWHM by the formula

$$\mathrm{SNR}_{\mathrm{FWHM,BEL,2}} = \sqrt{3} \frac{\sum_m f_m}{\sqrt{\sum_m (f_m/\mathrm{SNR}_m)^2}}. \tag{4.14}$$

In this equation, we choose the sample number as index m, the sample flux as f_m, and the SNR of sample m as SNR_m. We calculate $\mathrm{SNR}_{\mathrm{FWHM,BEL,2}}$ for different magnitudes between $14 \, \mathrm{mag} \leq G_{\mathrm{RVS}} \lesssim 17 \, \mathrm{mag}$. To infer the flux at different magnitudes, we scale the VB2001 template spectrum with SDSS quasars. We present the results of our second SNR approach in Table 4.3. When we compare both SNR approaches (Figure 4.18 and Table 4.3), we find similar values for the SNR in the FWHM of Hα, Hβ, MgII, CIII], or CIV. Hence we can use our SNR calculations to analyze research prospects when BELs fall into the RVS.

Due to four CCD rows of the RVS on the focal plane (Figure 2.1) in comparison to the seven CCD rows of the blue and red photometers, the number of subsequent observations is smaller than for the blue and red photometers. As explained in Chapter 2, we estimate that there are typically three subsequent RVS observations within a few day. In case we coadd three subsequent measurements, the SNR in the FWHM of BELs increases by a factor of $\sqrt{3}$.

The RVS of Gaia does not reach the proposed magnitude limit of $G_{\mathrm{RVS}} = 17$ mag, but a limit of
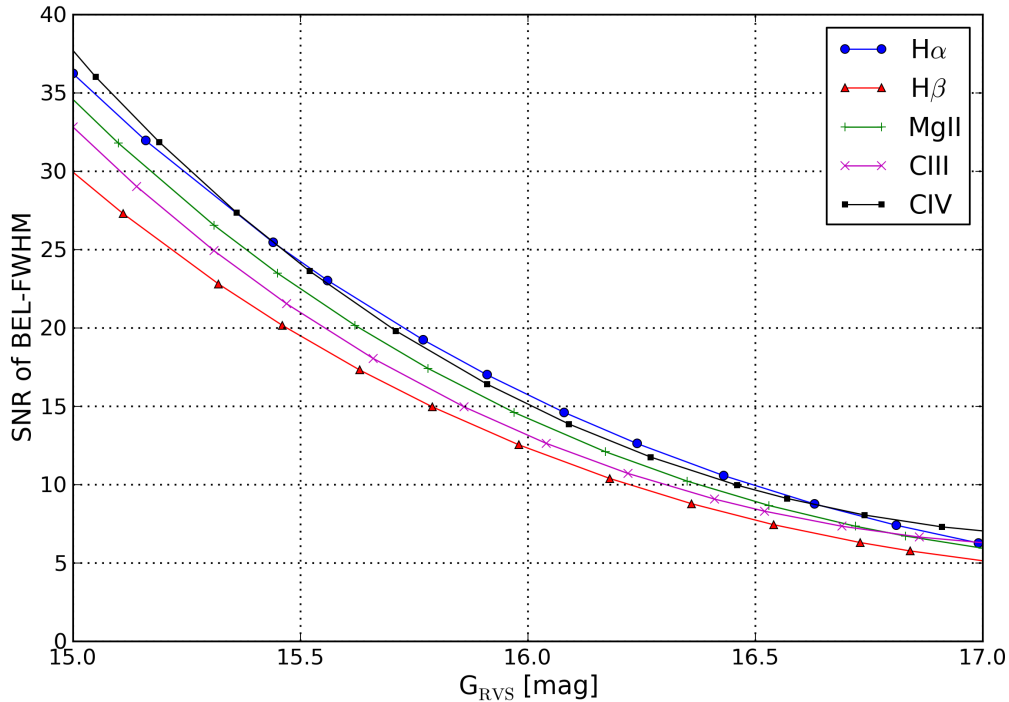
Figure 4.18: For the BELs Hα, Hβ, MgII, CIII], and CIV we calculate the SNR of their FWHM as function of G_{RVS}. Because quasars are faint objects, we show the results for magnitudes $G_{RVS} > 15$ mag. The SNR of all emission lines is only between five and seven at $G_{RVS} = 17$ mag. Diagram from PW2015.

$G_{RVS} \approx 16$ mag[5]. Therefore, we have to study the revised plot of the SNR per sample which we find on the Gaia web page[6]. This time, the diagram is only available for the end-of-mission (composite) spectra but again for the continuum level of stars. Additionally, the plot of the SNR per sample is only shown until a magnitude of $G_{RVS} \approx 15$ mag. To reach the revised magnitude limit of $G_{RVS} = 16$ mag, we extend the revised function of the SNR per sample linearly in the logarithmic plot. From this plot, we infer the revised values of the SNR per sample for $G_{RVS} = 15$ mag and $G_{RVS} = 16$ mag. Additionally, we divide the revised SNRs per samples by $\sqrt{40}$ to obtain the value for a single measurement. Now we can compare the previous SNR per sample (Figure 4.18) with these two values. We find that the values of the SNR per sample (single measurement) for $G_{RVS} = 15$ mag and $G_{RVS} = 16$ mag are about 0.33 and 0.13, respectively. Hence they are similar to the previous values but for 1 mag fainter magnitudes ($G_{RVS} = 16$ mag and $G_{RVS} = 17$ mag) in the previous SNR per sample plot. At least for faint magnitude $G_{RVS} \gtrsim 15$ mag, we can use our previous estimations but shifted towards 1 mag brighter objects.

Next we consider the revisions due to Gaia's magnitude shift and three subsequent RVS measurements within a few days in order to plot the final diagram of the SNR per sample in the FWHM for all five BELs (Figure 4.19). In contrast to Figure 4.18, we only show magnitudes between 15 mag $\lesssim$ $G_{RVS} \lesssim 16$ mag but we use the same range of the SNR on the ordinate. Our final values of the SNRs in the FWHM are between nine (Hβ) and twelve (CIV) for $G_{RVS} = 16$ mag and between 21 (Hβ) and 27 (Hα) for $G_{RVS} = 15$ mag.

---

[5]http://www.cosmos.esa.int/web/gaia/science-performance, accessed on April 3 2016
[6]http://www.cosmos.esa.int/web/gaia/sn-rvs, accessed on April 3 2016

line	G_{RVS} [mag]	$\text{SNR}_{\text{FWHM,line}}$
Hα	16.9	6
	16.3	11
	15.0	33
	14.0	71
Hβ	17.1	5
	16.5	7
	15.9	12
	14.8	32
MgII	16.9	6
	16.3	9
	16.1	11
	15.3	23
CIII]	17.0	6
	16.2	12
CIV	16.9	8

Table 4.3: We show the RVS signal-to-noise ratios in the FWHM of Hα, Hβ, MgII, CIII], or CIV for several magnitudes between $14\,\text{mag} \leq G_{\text{RVS}} \lesssim 17\,\text{mag}$). In this SNR analysis, we determine G_{RVS} by equation 4.14.

4.5.3 Quasar Research when Spectral Lines fall in the RVS

Before we study potential quasar research with Gaia's high-resolution spectra, we want to know how many quasars have redshifts for which the BELs Hα, Hβ, MgII, CIII], or CIV are within the wavelength range of the RVS. For this, we first search for all quasars brighter than $G_{\text{RVS}} = 16\,\text{mag}$ (in the beginning of our study $G_{\text{RVS}} = 17\,\text{mag}$) that are given in the simulated Gaia quasar catalog (Robin et al. 2012). We find 5153 quasars for the previously proposed magnitude limit and 584 quasars for the revised magnitude limit. Out of these objects, only a small fraction will have BELs in Gaia's high-resolution spectral range. In Table 4.4, we list the number of bright quasars with BELs in the RVS for both magnitude limits. For the magnitude limit of $G_{\text{RVS}} = 17\,\text{mag}$, we determine 579 quasars with lines in the RVS. However, due to the revised 1 mag brighter magnitude limit, the number of quasars decreases by about one order of magnitude to 70 objects. Out of these quasars, the majority will have Hα in the RVS. In Figure 4.20, we present the redshift distribution of expected quasars (Robin et al. 2012) brighter than $G_{\text{RVS}} = 17\,\text{mag}$ (red) using a redshift bin width of 0.2. Moreover, we plot the fraction of quasars that additionally have BELs in the RVS in black. For the latter quasars, we select a redshift bin width for which the maxima of the individual BELs are within the RVS. We list the redshift intervals (bin width) for Hα, Hβ, MgII, CIII], and CIV in 4.4.

The SNR per sample in the RVS is extremely low at the faint magnitude limit of $G_{\text{RVS}} = 16\,\text{mag}$. We need strong BEL signals for useful measurements. Additionally, we rebin the samples that cover the width of an emission line. Although we increase the SNR by using the FWHM of broad emission lines, the SNR is still only about nine and twelve at the revised RVS magnitude limit. Hence it is not possible to investigate absorption lines or narrow emission lines with Gaia's RVS that would have much
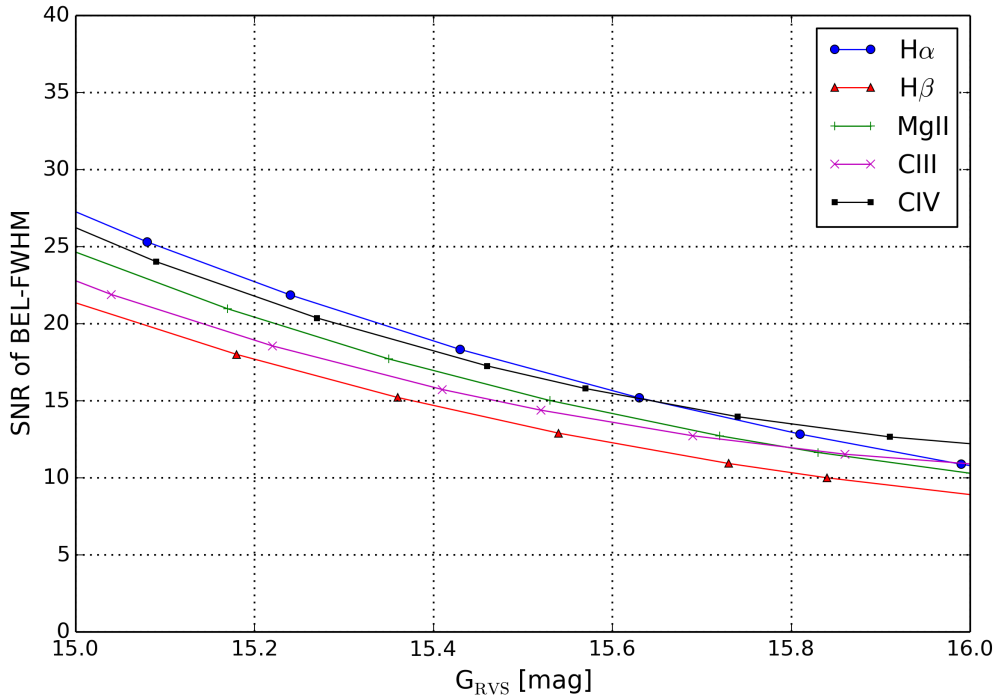
Figure 4.19: We show the revised SNR in the FWHM of the BELs Hα, Hβ, MgII, CIII], or CIV as function of G_{RVS}. For this, we considered the magnitude limit $G_{RVS} = 16$ mag and three subsequent measurements. The colors are the same as used in Figure 4.18.

smaller SNRs than the FWHM of Hα, Hβ, MgII, CIII], or CIV. Even when the SNR in some samples of narrow emission lines is as large as twenty (for example), the quasar magnitude G_{RVS} would be fainter than the RVS magnitude limit. We expect about seventy quasars (Table 4.4) that will get high-resolution spectra of a broad emission line. For these quasars we can explore the dynamics or the geometry of the broad emission line region by analyzing the line profile and variability. However, at the faint end ($G_{RVS} = 16$ mag) the uncertainties would be very high due to the small SNR. The combination of high- and low-resolution quasar enables further quasar studies. For example, we can measure the FWHM of individual broad emission lines with the RVS. To identify the BEL (the quasar redshift), we need the information of Gaia's blue and red photometers. If we are able to infer the time lag between BEL and continuum radiation from Gaia's low-resolution spectra together with the FWHM from the high-resolution spectrum, we could approximate the black hole mass by Equation 3.16. Because of Gaia's scanning law with observational gaps of typically two months, especially quasars with large time lags and high observational cadence are suitable for black hole mass estimations.

4.6 Astrometric Quasar Analysis with Gaia

In this section, we summarize potential astrometric investigations of quasars from the literature. Furthermore, we give an outlook whether it is possible to detect the potential astrometric shifts with the Gaia satellite. We presented this section also in our paper PW2015.

Taris et al. (2011) describe an interaction between flux variability and photocenter changes in quasars. Based on this investigation, Popović et al. (2012) simulate the variability of the photocenter related to

BEL	z range	$G_{\mathbf{RVS}} \leq 17\,\mathbf{mag}$	$G_{\mathbf{RVS}} \leq 16\,\mathbf{mag}$
Hα	0.291 - 0.326	349	47
Hβ	0.742 - 0.791	94	11
MgII	2.027 - 2.110	103	8
CIII]	3.440 - 3.565	18	1
CIV	4.480 - 4.633	15	3
Σ		**579**	**70**

Table 4.4: We present the number of quasars from the simulated Gaia quasar catalog which have BELs in Gaia's RVS. Furthermore, we show the results for the previous and the revised magnitude limit ($G_{\mathrm{RVS}} \leq 17\,\mathrm{mag}$ and $G_{\mathrm{RVS}} \leq 16\,\mathrm{mag}$).
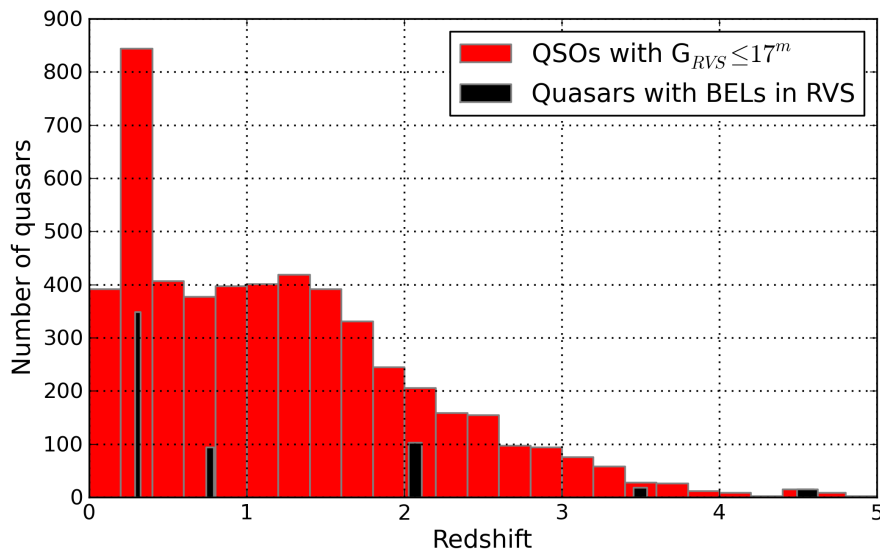
Figure 4.20: We plot the redshift distribution for simulated Gaia quasars that are brighter than $G_{\mathrm{RVS}} = 17\,\mathrm{mag}$ (red) in redshift bin width of 0.2. Furthermore, we show the fraction of these bright quasars with BELs in the RVS (black). The changing bin widths for Hα, Hβ, MgII, CIII], and CIV (left to right black bins) represent the redshift interval when at least the BEL maxima are within the RVS. Histogram from PW2015.

variations in the accretion disk and the dust torus of quasars. They estimate that accretion disk perturbations of low-redshifted AGNs with huge black hole mass ($\gtrsim 10^9 M_\odot$) may induce photocenter shifts of a few milliarcseconds. In addition, torus related photocenter offsets, which result from illuminations when dust covers the central region, could be as large as several milliarcseconds. Hence both effects would be observable with Gaia. Furthermore, Popović et al. (2012) emphasize that Gaia's quasar sample for construction of the reference frame should not contain objects with photocenter variability.

Shen (2012) explores the opportunity of astrometric reverberation mapping. In case of a non-spherically symmetric BLR in spatial structure and velocity distribution, photocenter offsets are induced by different BLR arrival times of continuum variations. In addition to common reverberation mapping, astrometric reverberation mapping offers independent limitations on geometry and kinematic configuration of BLRs like inclination or rotation angles. For typical quasar luminosities and a redshift of $z \approx 0.5$ the author determines expected photocenter offsets of some tens of microarcseconds. The amount would be slightly larger for dust tori astrometric reverberation mapping. Hence Gaia's astrometric accuracy for

a single-observation of quasars is not sufficient to measure astrometric reverberation mapping of their BLR and it is unlikely to measure the event for dust tori of quasars.

Another application of astrometry with quasars is astrometric microlensing. This effect causes a small positional shift of quasars, which are gravitationally lensed by small stellar mass foreground objects. Astrometric microlensing in multiply lensed quasars or in single quasars can cause center-of-light (centroid) displacements (Lewis & Ibata 1998). This centroid is the weighted sum of all unresolved microimages produced by microlensing, and it can be displaced due to creation of a bright pair of microimages during a caustic crossing. The photocenter shift in quasars by astrometric microlensing of stellar mass objects in the lensing galaxy could be of order tens of microarcseconds and has a timescale of months or years (Treyer & Wambsganss 2004). Even if Gaia might not be able to measure the astrometric microlensing effect in quasar sources by single stars, microlensing induced by small mass stellar clusters in the lensing galaxy could cause centroid shifts of several milliarcseconds. This would be detectable with Gaia or complementary satellites (Popović & Simić 2013).

4.7 Conclusions

The Gaia mission provides two low-resolution spectra from Gaia's blue and red photometric instruments (BP and RP) that have wavelength dependent dispersion. In this chapter, we studied these photometers to investigate the quasar spectra detected by the satellite. For this, we simulated Gaia's low-resolution quasar spectra by convolving the composite quasar spectrum VB2001 with a gaussian kernel. In addition to a noiseless spectrum, we analyzed the important noise contributions (photon noise) to produce a series of low-resolution quasar spectra at different magnitudes and redshifts for individual observations (five single field-of-view measurements) and for the end-of-mission (72 combined field-of-view measurements).

By analyzing individual low-resolution quasar spectra for magnitudes $G = 16\,\mathrm{mag}$, $18\,\mathrm{mag}$, $19\,\mathrm{mag}$, and $20\,\mathrm{mag}$, we observed the influence of noise to the spectra. In these spectra, we could detect spectral features like the broad emission lines, broad absorption lines, or the "small blue bump" for all bright quasars $G \lesssim 18\,\mathrm{mag}$. For fainter objects, the redshift is relevant to detect the features in the VB2001 template spectra. When we increase the magnitude to $19\,\mathrm{mag}$ or even $20\,\mathrm{mag}$, the SNR decreases significantly and we can not observe several spectral characteristics in individual spectra. For quasars that are very different to the composite quasar spectrum, the equivalent widths and shapes of their broad lines are important as well to make realistic predictions. Additionally, we produced low-resolution VB2001 quasar spectra after five years of observations to study the detectability of quasar redshifts with Gaia. At the end of the mission, we are able to calculate quasar redshifts even at the faint end. In each analyzed redshift interval, there are at least two BELs. However, some redshift areas are more difficult (resulting in higher uncertainties) due to the absence of very prominent lines like Hα or Lyα. For large redshifts ($z \gtrsim 2.3$), we obtain the easiest region to measure the redshift.

Afterwards, we studied our low-resolution quasar spectra at different redshifts and magnitudes to investigate potential variability measurements with Gaia. Due to Gaia's scanning law, we found that the satellite is very suitable to analyze long-term continuum and BEL variability of order months to a few years for bright quasars with magnitudes $G \lesssim 18\,\mathrm{mag}$. By measuring equivalent widths of BELs, we will be able to study the Baldwin effect for these quasars. Those quasars, which have much more

than the 72 average number of observations, are promising candidates for a large reverberation mapping campaign. By determining the time lag between the continuum and the BEL response, we can study the geometry of the broad line region. Additionally, we could follow the suggestions of Watson et al. (2011) and infer cosmological luminosity distances for these quasars to test different cosmological models. For this approach, we need sufficiently large time lags detectable with Gaia. Therefore, the most suitable quasars have large redshifts, large BLR radii (large luminosities), and we should select low-ionisation lines as they are emitted at larger radii than high-ionisation lines.

In addition to Gaia's low-resolution spectra, there is a radial velocity spectrograph which records high-resolution spectra ($R \sim 11,500$) in a small wavelength range ($8,470\,\text{Å} \leq \lambda \leq 8,710\,\text{Å}$). We analyzed bright quasars that have redshifts for which the broad emission line Hα, Hβ, MgII, CIII], or CIV falls in this interval. We determined 70 quasars brighter than $G_{\text{RVS}} = 16\,\text{mag}$ that have a BEL in this wavelength band. But to make reliable predictions on potential variability studies with these objects, we calculated the SNR in the FWHM of the important BELs. For the 70 objects with BELs in the RVS wavelength range, we could study the line profile and its variations with time, to better understand the structure and the dynamics in the BLR. For these objects we should use information from BP and RP as well, for example, to infer the quasar redshift. However, the SNR in the FWHM is extremely low at the faint end. Hence the analysis of BAL or all kind of narrow lines is not possible with Gaia's RVS.

Chapter 5

SDSS Quasars with Broad Emission Lines in the Radial Velocity Spectrograph

In the last chapter, we searched through the simulated Gaia catalog (Robin et al. 2012) and found 579 quasars that have BELs in the wavelength interval for which Gaia provides a high-resolution spectrum and which are brighter than the originally proposed magnitude limit of $G_{\mathrm{RVS}} = 17\,\mathrm{mag}$. Due to the revision of the limiting RVS magnitude to $G_{\mathrm{RVS}} = 16\,\mathrm{mag}$, the number of objects decreased to 70. In this chapter, we search for those bright quasars that are already known from SDSS and which additionally have BELs that will fall into Gaia's RVS wavelength interval. By analyzing the spectra of these SDSS objects, we can identify interesting BEL variations. But for this, we need at least two quasar spectra (the majority has only one spectrum) available within SDSS. If so, they are promising candidates for line variability studies which can be induced by continuum responses or by variations in the BLR itself. As mentioned above, the resolution of SDSS spectra $\lambda/\Delta\lambda$ is about 2,000 and the wavelength interval is somewhat smaller than the wavelength range of Gaia's low-resolution spectra.

5.1 Number of SDSS Quasars with BELs in the RVS

We use the SDSS bulk search tool[1] in order to identify those quasars that are brighter than the previous (later on the revised) G_{RVS} magnitude limit and that have redshifts for which BELs fall into the wavelength range of the RVS. To infer the magnitude limit of SDSS quasars, we determine the magnitude G_{RVS} for a series of SDSS quasars by integrating the line flux between $8,470\,\text{Å} \le \lambda \le 8,710\,\text{Å}$ for these individual quasars and for the star Vega as reference. Therefore, we consider a few quasars for every BEL that falls in the wavelength range of the RVS. For each line, we select several quasars at different magnitudes. Then we use Equation 4.10 to calculate G_{RVS}. The G_{RVS} magnitude strongly depends on the quasar redshift and we can not find simple magnitude transformation equations like between G and V or G and r' in Chapter 4.1. Our approach delivers that the SDSS magnitude z' is typically between 0.5 mag and 0.7 mag (only for some objects even 1.0 mag) fainter than the corresponding magnitude G_{RVS}. Hence we select SDSS quasars with $z' = 17.5\,\mathrm{mag}$ (later on $z' = 16.5\,\mathrm{mag}$) to find SDSS quasars with BELs in the RVS that should get high-resolution spectra from Gaia.

In Table 5.1, we present the estimated amount of bright SDSS quasars, emphasized in blue, for

---

[1] http://skyserver.sdss.org/dr12/en/tools/search/sql.aspx, accessed on April 10, 2016

BEL	z range	$G_{\mathrm{RVS}} \leq 17\,\mathrm{mag}$	$z' \leq 17.5\,\mathrm{mag}$	$G_{\mathrm{RVS}} \leq 16\,\mathrm{mag}$	$z' \leq 16.5\,\mathrm{mag}$
$H\alpha$	0.291 - 0.326	349	341	47	37
$H\beta$	0.742 - 0.791	94	90	11	7
MgII	2.027 - 2.110	103	96	8	8
CIII]	3.440 - 3.565	18	6	1	0
CIV	4.480 - 4.633	15	2	3	0
Σ		**579**	**535**	**70**	**52**

Table 5.1: We list the number of quasars from SDSS in comparison to the simulated Gaia quasar catalog which have BELs in Gaia's RVS. We present the numbers for the previous and the revised magnitude limit ($G_{\mathrm{RVS}} \leq 17\,\mathrm{mag}$, $z' \leq 17\,\mathrm{mag}$, $G_{\mathrm{RVS}} \leq 16\,\mathrm{mag}$), and $z' \leq 17\,\mathrm{mag}$.

the individual redshift intervals. For this list, we check the spectra of about 600 quasars in the SDSS bulk search tool by eye and delete about 70 objects because they were misidentified mainly as stars. Additionally, we repeat the resulting numbers from the simulated Gaia quasar catalog in the table to compare the number of quasars for both catalogs. As expected, both numbers are very similar but we miss some SDSS quasars at the faint magnitude limit. However, due to the low SNR at $G_{\mathrm{RVS}} = 17\,\mathrm{mag}$ ($G_{\mathrm{RVS}} = 16\,\mathrm{mag}$), those quasars would be very difficult to investigate with Gaia's RVS. We expect that Gaia is detecting 535 (52) SDSS quasar spectra for which we could analyze $H\alpha$, $H\beta$, MgII, CIII], or CIV. In the following, we analyze these 535 (52) quasar spectra in order to find promising candidates for a line variability study.

5.2 Selected SDSS Quasars with Variable Spectra

To study interesting and variable SDSS quasar spectra, we search for all bright quasars (first $z' \leq 17.5\,\mathrm{mag}$, later on $z' \leq 16.5\,\mathrm{mag}$) that have at least two spectra available in the SDSS dr7 database (Schneider et al. 2010) and a BEL in the RVS wavelength range. In this process, we produce a preliminary candidate list. We analyze the variablity features of these objects and validate their flux variations by studying stellar spectra with same Julian Date and Plate information. From this, we obtain a final candidate list that contains six interesting quasars from SDSS. They show either strong BEL changes or continuum variations in a timescale of weeks or months which should additionally lead to BEL variability. Figure 5.1 shows the individual line spectra of those quasars in the wavelength interval of Gaia's RVS (blue). Moreover, we present their magnitudes, the detected BEL, and the dates of individual spectra in Table 5.2. Because the spectra of the individual quasars change, G_{RVS} varies with time and we have to select one spectrum to calculate this magnitude in Table 5.2. We see that two candidates (1 and 2) exhibit strong continuum shifts within months or even weeks. In contrast, candidate 3 produces strong BEL variability, but only very small continuum variations. Whereas candidates 4 and 6 show variability in BEL and continuum. The spectrum of candidate 5 is more complicated, because we find a jump in its continuum flux below $\lambda = 6,000\,\text{Å}$. We detect this jump also in parallel spectra of stars. However, the variability of its BEL at larger wavelengths most likely is true. Candidate 1 and 5 have $H\beta$ in the RVS wavelength range (line with lowest SNR in FWHM) and in addition to this, G_{RVS} amounts to 16.3 mag and 16.3 mag, respectively. Hence their spectra would be more noisy than the spectra of candidates 2,3,4,

	BEL	z' [mag]	G_{RVS} [mag]	Dates of Spectra
1	Hβ	17.0	16.3	2002-Nov-30, 2000-Sep-22, 2000-Dec-06, 2000-Sep-23, 2001-Oct-18
2	MgII	15.8	15.2	2000-Sep-28, 2001-Sep-24, 2000-Sep-23
3	Hα	16.3	15.4	2000-Sep-05, 2002-Sep-01
4	Hα	17.0	16.6	2001-Mar-28, 2000-Sep-25
5	Hβ	17.1	16.4	2011-May-24, 2004-May-11
6	Hα	17.4	16.5	2000-Apr-27, 2001-Feb-14

Table 5.2: We list the affected BEL in the RVS, the magnitudes, and the epochs of spectra observations for candidates 1 to 6 (see Figure 5.1). The dates, written from left to right, correspond to the spectra from top to bottom.

	BEL	z' [mag]	G_{RVS} [mag]	Dates of Spectra
1b	MgII	15.8	15.4	2012-May-26, 2008-Jan-13
2b	MgII	15.8	15.3	2012-Apr-15, 2007-Mar-24
3b	Hβ	15.6	14.6	2002-Oct-07, 2002-Mai-30
4b	MgII	15.8	15.1	2000-Sep-28, 2000-Sep-23

Table 5.3: We give the affected BEL in the RVS wavelength interval, the magnitudes z' and G_{RVS}, and the epochs of spectra measurements for quasars 1b to 4b in Figure 5.2. The dates, written from left to right, correspond to the spectra from top to bottom.

and 6.

Apart from SDSS quasars, we find a (physical) binary quasar (LBQS1429-008) and a bright multiply lensed quasar (HE2149-2745) in the CASTLE Survey (Kochanek et al. 2013) which have suitable redshifts for our study[2]. But we have not enough spectral information to analyze the potential variability of their BELs. For both objects, we could study the MgII line with Gaia's RVS. The quasars have magnitudes of $H = 15.79\,\mathrm{mag}$ (LBQS1429-008) and $I = 16.29\,\mathrm{mag}$ (HE2149-2745).

Because the magnitude limit for detecting objects in the RVS changed, we have to repeat the search for variable SDSS quasars. Only four of the 52 SDSS quasars with suitable redshift and $z' \leq 16.5\,\mathrm{mag}$ have two available spectra. Hence we have not enough information to select the most promising quasar candidates that exhibit strong variable BELs. However, these four quasars have interesting line spectra and hence we plot their BELs signatures in Figure 5.2. Quasar candidates 1b and 2b have variable BELs within a few years, whereas the quasar candidates 3b and 4b show variations within six weeks (3b) and five days (4b). We determine the G_{RVS} magnitude for all of these four SDSS quasars. For this, we select the spectrum that corresponds to a fainter magnitude. As mentioned above, the spectra and magnitudes of the individual quasars vary with time. For example, for the first object 1b, we determine a magnitude of $G_{RVS} = 14.9\,\mathrm{mag}$ in the red spectrum and $G_{RVS} = 15.4\,\mathrm{mag}$ in the black spectrum. In Table 5.3, we present the affected BEL, the SDSS z' magnitude, and our calculated G_{RVS} magnitude (selected spectrum) for all four quasars.

---

[2]http://cfa-www.harvard.edu/glensdata/
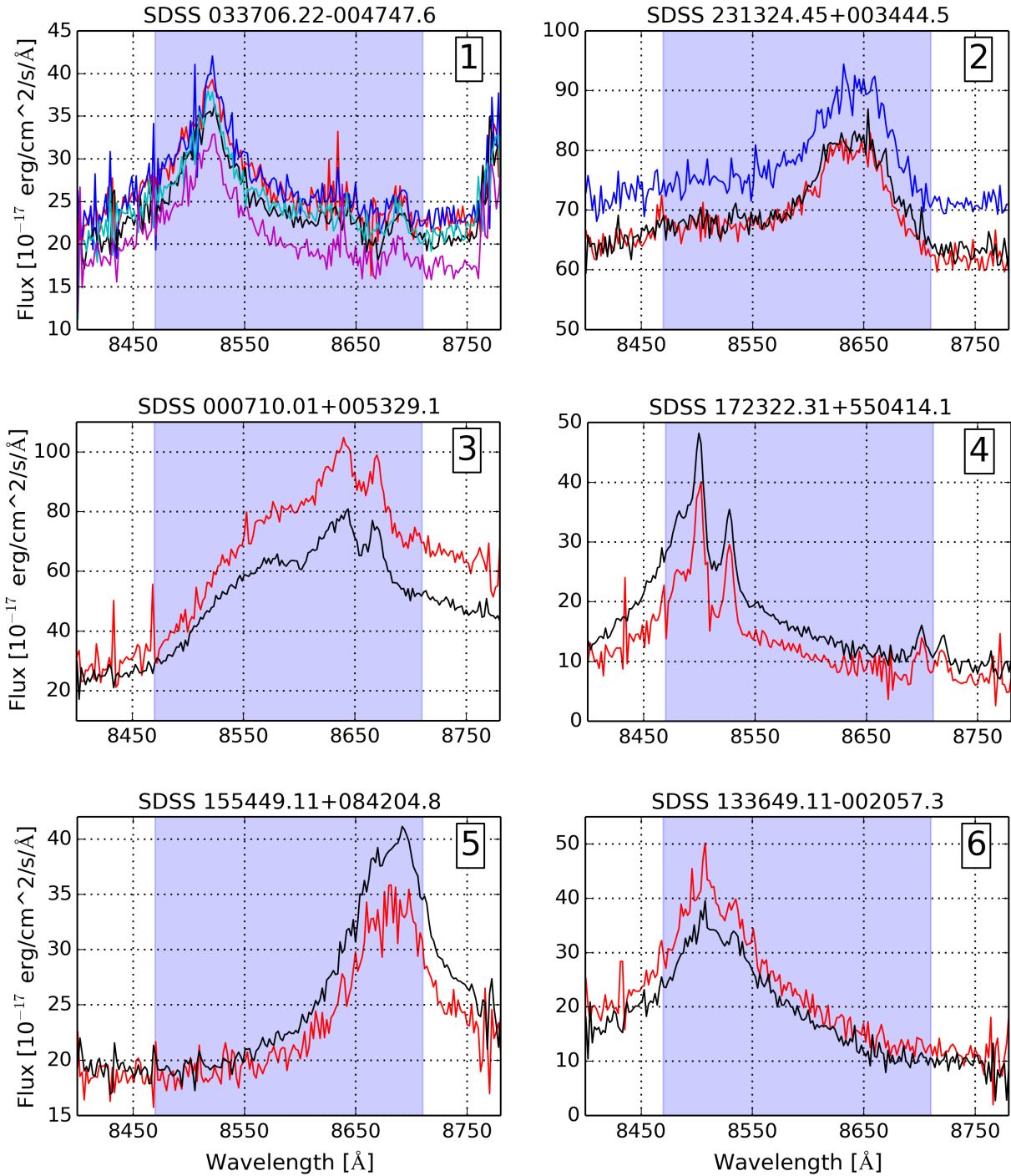
Figure 5.1: We present six bright SDSS quasars ($z' \leq 17.5$ mag) which have BELs in Gaia's RVS and at least two available spectra in dr7. The blue shaded region indicates the RVS wavelength interval. These objects would be promising candidates for a BEL variability study for Gaia's previous magnitude limit. We list important information of the six quasars in Table 5.2. Plots from PW2015.
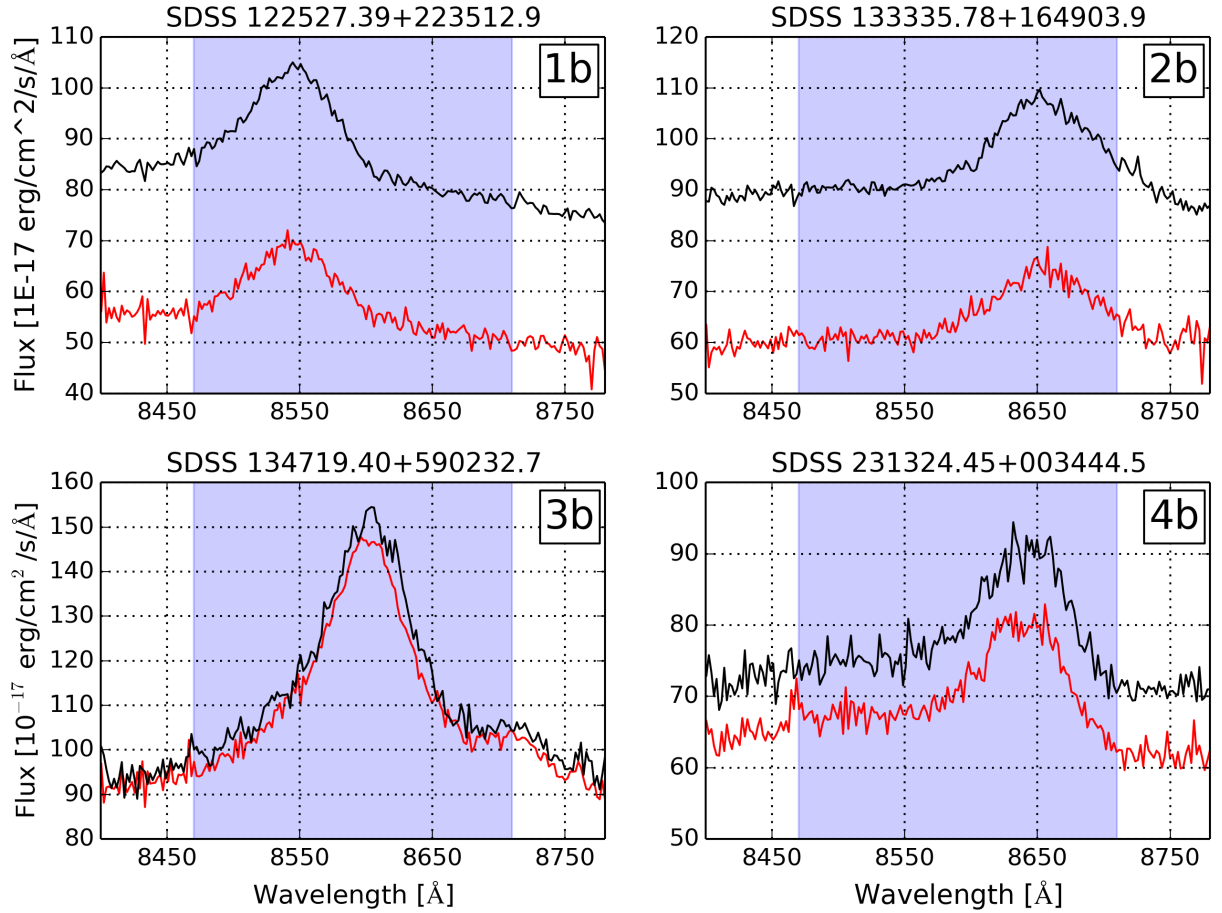
Figure 5.2: We present the four bright SDSS quasars ($z' \leq 16.5\,\text{mag}$) which have BELs in Gaia's RVS and two available spectra. These objects are promising candidates for a BEL variability study with Gaia. We list important information of the four quasars in Table 5.3.

5.3 Conclusions

Due to the revised magnitude limit of $G_{\text{RVS}} \leq 16\,\text{mag}$, we expect that Gaia's radial velocity spectrograph is obtaining high-resolution spectra of broad emission lines for about 70 quasars. By estimating the corresponding SDSS magnitude limit to $z' = 16.5\,\text{mag}$, we find 52 SDSS quasars with relevant redshifts. For four of these quasars, we plot their spectra in order to show their variable broad emission lines. For this very small number of quasars that Gaia should detect with the RVS (~ 70), we could investigate the profile of BELs and its variations with time as explained in the last chapter. There are on average about 40 measurements within Gaia's lifetime of five years. Hence we could only analyze long-term variability of BELs. Although we have some quasars with additional intraday observations, we would need to coadd the spectra to obtain a higher SNR in the RVS spectrum instead of analyzing single spectra.

Part II

The Astrometric Microlensing Effect with Gaia
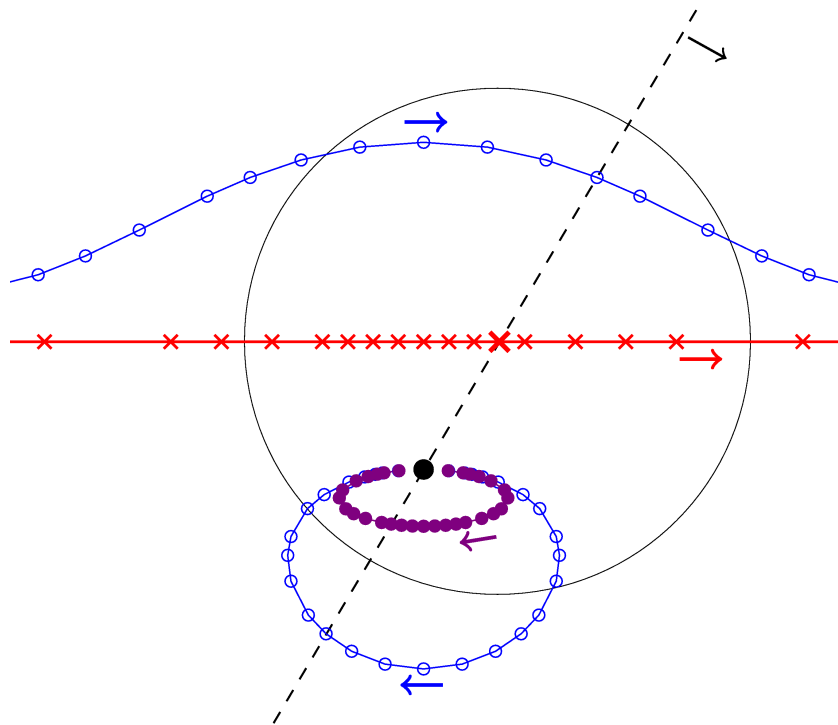
Chapter 6

Introduction

Gaia measures the positions and kinematics of about one billion stars in the Milky Way. Due to its positional accuracy and the large amount of stars, the satellite is able to observe the astrometric microlensing effect. In our work we consider the special case of strong gravitational lensing with a pointlike lens and source which we call microlensing. When the projected positions on the sky of observer, lens, and source are close, but not perfectly aligned always two images exist. However, the images have a separation of order two Einstein radii (typically a few milliarcsecond) and only their light centroid could be observable with precise astrometric telescopes. Instead of two images, an Einstein radius would appear if all components are perfectly aligned. The Einstein radius for microlensing in the galaxy is given by

$$\theta_{\mathrm{E}} = \sqrt{\frac{4GM_{\mathrm{L}}}{c^2}\left(\frac{1}{D_{\mathrm{L}}} - \frac{1}{D_{\mathrm{S}}}\right)}, \tag{6.1}$$

where D_{L} and D_{S} are the distances of source and lens to the observer, and M_{L} the mass of the lens (Chwolson 1924; Einstein 1936; Paczynski 1986). For small angular separations ($\lesssim \theta_{\mathrm{E}}$) of lens and source, one can also detect the corresponding magnitude change which is called photometric microlensing.

A quantity to describe the probability of microlensing events is the optical depth τ. Paczynski (1986) describes it as an integral along the line-of-sight:

$$\tau = \int_0^{D_S} \frac{4\pi G \cdot D_{\mathrm{L}}(D_{\mathrm{S}} - D_{\mathrm{L}})}{c^2 \cdot D_{\mathrm{S}}} \rho(D_{\mathrm{L}})dD_{\mathrm{L}}, \tag{6.2}$$

where $\rho(D_{\mathrm{L}})$ characterizes the average matter density of microlensing at the lens distance. He estimates that about one in a million stars ($\tau = 5 \cdot 10^{-7}$) will be affected by microlensing. However, Paczynski assumed a projected lens source separation smaller than one Einstein radius. This is necessary to detect photometric microlensing, but one can measure the astrometric displacements to much larger angular lens source distances. Hence the optical depth and probability for astrometric microlensing is considerably higher. Belokurov & Evans (2002), for example, determine an all-sky astrometric microlensing optical depth for Gaia of about $\tau_{\mathrm{ast}} = 2.5 \cdot 10^{-5}$. In comparison to Paczynski (1986), they calculate a slightly smaller value of $\tau_{\mathrm{phot}} = 1.2 \cdot 10^{-7}$ for photometric microlensing.

The probability to detect an astrometric microlensing event with a nearby lensing star is higher than with a distant lens. This is reasonable due to their larger proper motion and larger Einstein radius (Equa-
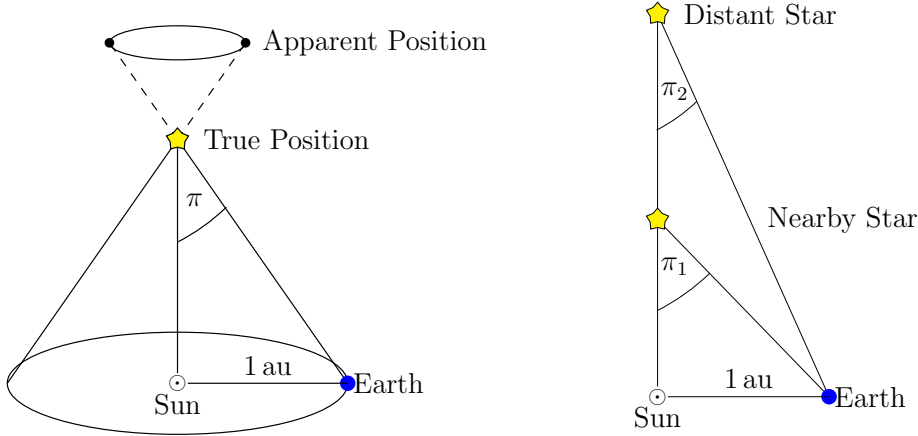
Figure 6.1: Left panel: The trigonometric parallax π is an angle which is defined by the distance between earth and sun (au) and the distance to the star. Right panel: The illustration shows the effect of an increasing parallax with stellar distance to the earth ($\pi_1 > \pi_2$). One can measure the same effect for proper motions that are typically higher for nearby stars. Image according to Proft (2010).

tion 6.1). Similarly to the proper motion, the trigonometric parallax π (e.g., Weigert et al. 2006),

$$\sin(\pi) = \frac{1\,\text{au}}{D_{\text{L}}}, \tag{6.3}$$

is larger for stars in the solar neighborhood. For small angles, as in the case of stellar parallaxes, we have $\sin(\pi) \approx \pi$. Hence if Gaia measures the stellar parallax (in arcseconds), we can calculate the distance to the object (in parsec). Schematically, we describe the parallax and the effect of decreasing parallax/proper motion with distance in Figure 6.1.

In this chapter, we give an introduction to the basics of astrometric and photometric microlensing. Furthermore, we present important information on the observation of microlensing with the Gaia satellite.

6.1 Basics of Photometric Microlensing

We define photometric microlensing as the amplification of light from a pointlike source by a pointlike lens. As described in Section 4.3, there are always two images (I+ and I-) due to the focusing of light. However, in case of microlensing one can not resolve the two images with current telescopes, which have a separation of about $2\theta_{\text{E}}$. With a typical mass interval of $10^{-6} \leq m/M_{\odot} \leq 10^6$, the Einstein radii for microlensing are of order milliarcsecond or smaller (Schneider et al. 2006). We can only determine the total image magnification derived by Paczynski (1986)

$$A(u) = |A_+| + |A_-| = \frac{u^2 + 2}{u\sqrt{u^2 + 4}} \tag{6.4}$$

$$\text{with } A_{\pm} = \frac{u^2 + 2}{2u\sqrt{u^2 + 4}} \pm \frac{1}{2}, \tag{6.5}$$

where the impact parameter u characterizes the projected distance between lens and source:

$$\vec{u} = \frac{\vec{\theta}_S - \vec{\theta}_L}{\theta_E}.$$

(6.6)

The total magnification $A(u)$ is always larger than one, but the sum of the individual image magnifications is equal to one ($A_+ + A_- = 1$). For large and small angular separations one can approximate the magnification by (Dominik & Sahu 2000)

$$A(u) \simeq 1 + \frac{2}{u^4} \quad (u \gg 1),$$

(6.7)

$$A(u) \simeq \frac{1}{u} \qquad (u \ll 1).$$

(6.8)

Hence in case of a large impact parameter, the magnitude shift

$$\Delta\text{mag} = -\frac{5}{\ln 10 \cdot u^4}$$

(6.9)

strongly depends on the angular separation but a photometric microlensing event is only observable for a small impact parameter. Due to this, the Einstein time

$$t_E = \frac{D_L \theta_E}{v_\perp} = \frac{\theta_E}{\mu}$$

(6.10)

is the typical timescale in photometric microlensing. It describes the duration to cross the Einstein radius θ_E and contains lens information on its proper motion μ, the distance D_L, and the transverse velocity $v_\perp$. We can determine the Einstein time from observed microlensing light curves. But for the derivation of the individual lens parameter, we need additional lens measurements, which are often not available. One could solve the degeneracy problem of lens parameters for special cases such as visible lenses, high magnification microlensing events ($A(u) \gg 1$), or binary lenses (Schneider et al. 2006). Apart from lens mass detections, one can use photometric microlensing observations to detect extrasolar planets (Mao & Paczynski 1991) or to study the density of bright- or dark objects (Paczynski 1986).

In Figure 6.2, we present different microlensing scenarios with small impact parameters ($u = 0.1, 0.3,$ 0.5, 0.7, 0.9, and 1.1). On the left image there is a point mass M causing an Einstein ring shown as dashed circle. The solid lines in the panel are the path of a source object for the individual impact parameters. Their corresponding source image magnification Δmag is given on the right panel in dependence on the time in units of t_E. One can see that the smaller the impact parameter the larger is the magnification. If u converges to zero, the magnification diverges theoretically to infinity. In practice, the pointlike objects have a dimension and the finite source size effect limits the magnification of the source image.

6.2 The Theory of Astrometric Microlensing

Apart from magnitude variations also the apparent position of the source will change due to microlensing. To detect this positional shift of a background star, high astrometric accuracy is necessary. In Figure 6.3, we show the principle of an astrometric microlensing event for a lens (red cross) with a distance of 50
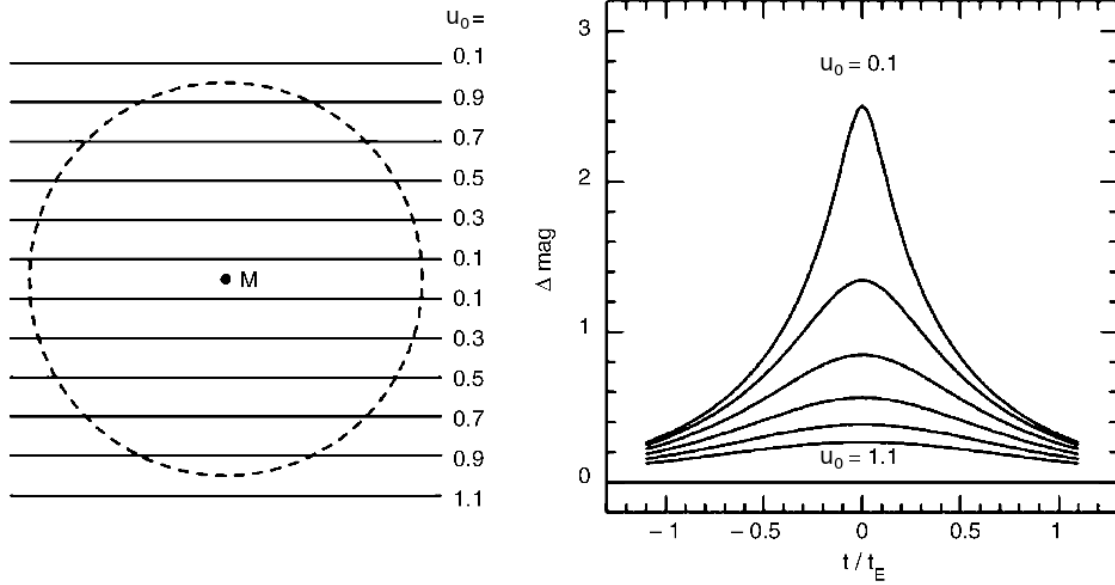
Figure 6.2: Left panel: A lens with mass M has an Einstein ring (dashed circle) with a radius given by Equation 6.1. The solid lines represent trajectories of a source with minimal impact parameters of $u_0 = 0.1$, 0.3, 0.5, 0.7, 0.9, and 1.1. Right panel: In this diagram the corresponding magnification (Δmag) for the six different minimal impact parameters in dependence on the time are shown. We can see that one can measure photometric microlensing events only for small impact parameters of $u \lesssim 1$ (Schneider 2006).

parsec and an Einstein radius of 8.5 milliarcseconds. In this example, the projected lens-source distance is 4.25 milliarcseconds (impact parameter $u = 0.5$). The position of the source (black dot) is fixed, but the lens (red cross) is moving in the upper panel. Due to microlensing there are two source images shown as blue open circles at coordinates

$$\theta_\pm = \frac{1}{2} \left[u \pm \sqrt{u^2 + 4} \right] \vec{\tilde{u}} \quad \text{with} \quad \vec{\tilde{u}} = \frac{\vec{u}}{u}. \tag{6.11}$$

However, current telescopes can not resolve the images. Hence only the light centroid (purple dot) is measurable. When the lens is moving from left to right, the centroid shift image moves clockwise on an elliptical orbit with semi-major axis (Dominik & Sahu 2000)

$$a = \frac{1}{2\sqrt{u_0^2 + 2}} \cdot \theta_E \tag{6.12}$$

and semi-minor axis

$$b = \frac{u_0}{2(u_0^2 + 2)} \cdot \theta_E. \tag{6.13}$$

The plot shows the displacement for an observer in the focus without considering the effect of the parallax. At each time, the positions of lens, source, source images, and centroid shift are aligned. The black circle indicates the Einstein ring of the lens for the situation when all images and true stellar positions are on the dashed line. The bottom panel shows the centroid shift trajectory for the astrometric microlensing event, but for impact parameters $u = 0.5$, 1, 2, $\sqrt{2}$, and 5.

In the following, we give the most important equations of the astrometric microlensing effect starting with a dark lens which is much fainter than the source. Considering the position of the two source images (θ_+ outside and θ_- inside the Einstein radius) and their magnifications, we can calculate the
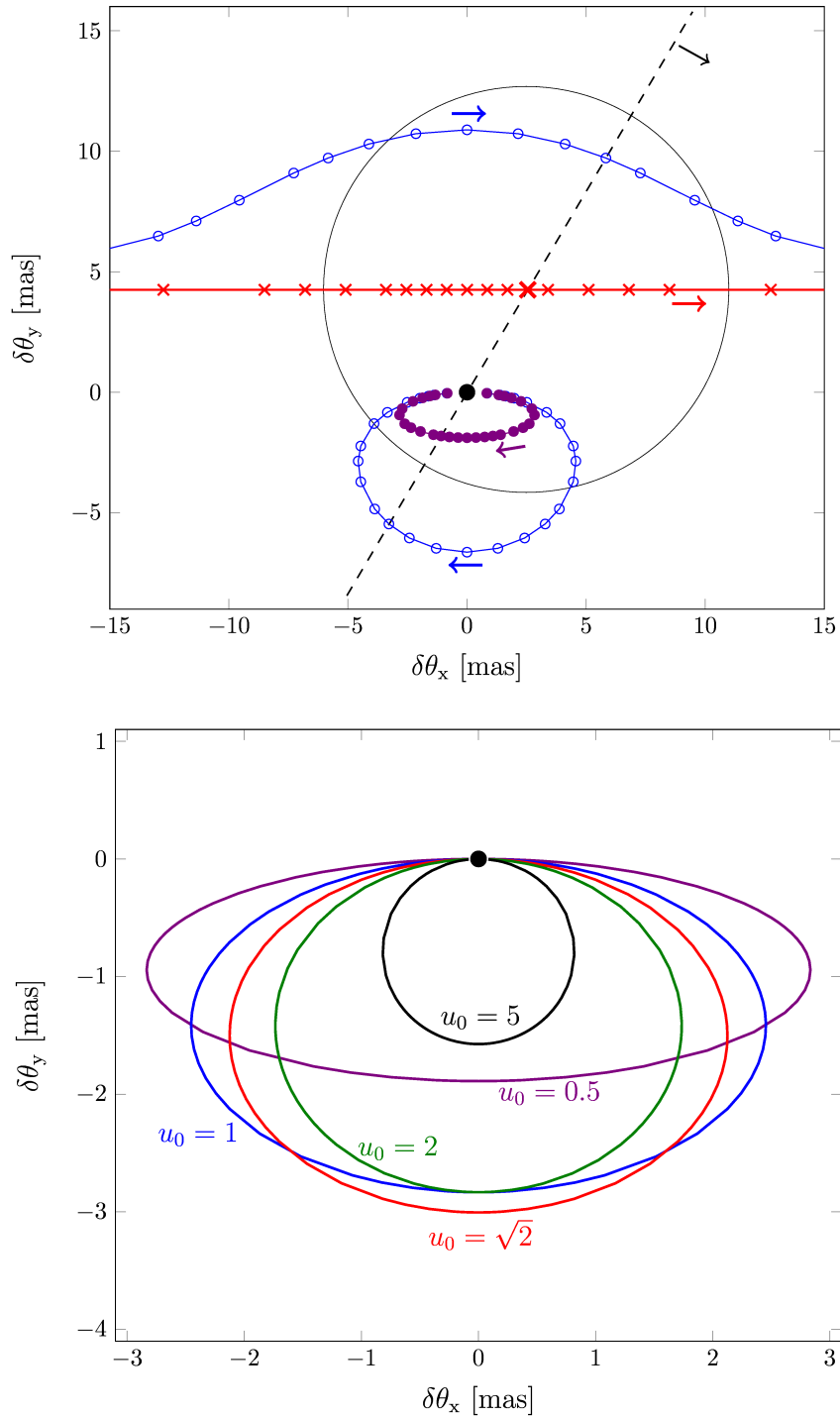
Figure 6.3: *Upper panel:* The illustration shows an astrometric microlensing event with a theoretical lens at distance 50 pc, Einstein radius of 8.5 mas, impact parameter of 0.5 (equivalent to 4.25 mas) and a distant background star. At each time, the lens (red cross), source (big black dot), two unresolvable source images (open blue circles), and the corresponding light centroid of the two images (violet dot) lie on one line (e.g., dashed line). (Proft et al. 2011, according to Fig. 3 of Paczynski 1996a). *Bottom panel:* We plot various centroid shift trajectories, colored ellipses, resulting from the astrometric microlensing effect of the same lens but for impact parameters $u_0 =$0.5, 1, $\sqrt{2}$, 2 and 5 (Proft et al. 2011, according to Fig. 2 of Dominik & Sahu 2000)

67

centroid position by (Hog et al. 1995; Miyamoto & Yoshii 1995; Walker 1995; Lee et al. 2010)

$$\vec{\theta}_{\rm c} = \frac{A_+\vec{\theta}_+ + A_-\vec{\theta}_-}{A_+ + A_-} = \frac{\theta_{\rm E}}{2}\left[\frac{u(u^2+4)}{u^2+2} + u\right]\vec{u}. \tag{6.14}$$

Using Equation 6.5 and 6.11, the shift between the light centroid and the unperturbed source position is then

$$\delta\vec{\theta}_{\rm c} = \vec{\theta}_{\rm c} - \theta_{\rm E}\vec{u} = \frac{\vec{u}}{u^2+2}\cdot\theta_{\rm E}. \tag{6.15}$$

At an impact parameter of $u = \sqrt{2}$ the centroid shift is maximal with (Paczynski 1998)

$$\delta\theta_{\rm c,max} \approx 0.354\theta_{\rm E}. \tag{6.16}$$

For example, the maximal possible centroid shift of our example lens ($D_{\rm L} = 50\,{\rm pc}$, $\theta_{\rm E} = 8.5\,{\rm mas}$, distant source) with an impact parameter of $u = \sqrt{2}$ amounts to 3 milliarcseconds. For large and small impact parameters, we can approximate the centroid shift by (Dominik & Sahu 2000)

$$\delta\theta_{\rm c} \simeq \frac{1}{u}\theta_{\rm E} \quad (u \gg \sqrt{2}), \tag{6.17}$$

$$\delta\theta_{\rm c} \simeq \frac{u}{2}\theta_{\rm E} \quad (u \ll \sqrt{2}). \tag{6.18}$$

One can see above that for large angular separations the magnitude shift (Equation 6.9) decreases with u^{-4} and the centroid displacement (Equation 6.17) only with u^{-1}. Hence Paczynski (1996b) and Miralda-Escude (1996) conclude that the cross section for astrometric microlensing is much larger than for photometric microlensing. Due to the larger cross section, the duration of an astrometric microlensing event is much larger than the Einstein time $t_{\rm E}$. Honma (2001) gives the average duration in which Gaia could observe the positional displacement as

$$t_{\rm ast} = \frac{\pi}{2}\left(\frac{t_{\rm E}\theta_{\rm E}}{\theta_{\rm min}}\right) \tag{6.19}$$

with an accuracy threshold $\theta_{\rm min}$. This threshold depends on the astrometric accuracy $\sigma_{\rm a}$ (Table 6.1) and the number of consecutive measurements n:

$$\theta_{\rm min} = \frac{3\sqrt{2}\sigma_{\rm a}}{\sqrt{n}}. \tag{6.20}$$

In case of Gaia, we typically have $n = 5$. Furthermore, we consider a two-dimensional accuracy and a 3-sigma-area for a convincing astrometric shift observation (Belokurov & Evans 2002; Lindegren & Bastian 2011).

If one can not resolve a bright lens from the background source, we have to consider the luminous lens effect. Similarly to equation 6.14, the position of the light centroid in case of a luminous lens is (Dominik & Sahu 2000)

$$\vec{\theta}_{\rm c,lum} = \frac{A_+\vec{\theta}_+ + A_-\vec{\theta}_- + f_{\rm LS}\vec{\theta}_{\rm L}}{A_+ + A_- + f_{\rm LS}}, \tag{6.21}$$

where $f_{\rm LS} = f_{\rm L}/f_{\rm S}$ is the flux ratio of the lens and source objects. The centroid shift of a luminous lens

is then given by

$$\delta\vec{\theta}_{\text{c,lum}} = \frac{A_+\vec{\theta}_+ + A_-\vec{\theta}_- + f_{\text{LS}}\vec{\theta}_{\text{L}}}{A_+ + A_- + f_{\text{LS}}} - \frac{\theta_{\text{E}}\vec{u}}{1 + f_{\text{LS}}}. \tag{6.22}$$

For large impact parameters ($u \gg \sqrt{2}$), one can approximate the centroid displacement by

$$\delta\theta_{\text{c,lum}} = \frac{1}{(1 + f_{\text{LS}})u}\theta_{\text{E}}. \tag{6.23}$$

Additionally, for an astrometric microlensing event with a bright lens and a small impact parameter it is reasonable to calculate the source centroid displacement for these impact parameters for which one can resolve lens and source. In case of Gaia, we use an angular resolution of 200 milliarcseconds. In this scenario, the largest with Gaia observable centroid shift would be at a lens-source distance of 200 milliarcseconds.

About half of all stars are part of a binary or multiple systems. Hence lensing stars have often a companion which causes distortions, twists, and jumps in the astrometric microlensing ellipse (Han et al. 1999). In general the systems are widely separated with a projected binary distance d much larger than the Einstein radius of the lens component that has the smallest angle to the source (primary lens). An & Han (2002) calculate the influence of a second lens in a widely separated system with a close source on the magnification and the centroid shift. Considering the mass ratio $q = m_2/m_1$ of the binary system, the magnitude of the second lens

$$A_2 \sim 1 + 2\frac{q^2}{d^4} \quad (d \gg 2) \tag{6.24}$$

has a minor impact on the resulting microlensing light curve. But the centroid shift of the second component

$$\delta\theta_2 \sim \theta_{\text{E,1}}\frac{q}{d} \quad (d \gg \sqrt{2}) \tag{6.25}$$

can affect the trajectory to much larger angular separations depending on the second lens mass. In this instance, we can determine the total centroid shift

$$\delta\vec{\theta}_{\text{c}} \sim \delta\vec{\theta}_{\text{c,1}} + \delta\vec{\theta}_{\text{c,2}} \tag{6.26}$$

as the superposition of the individual positional displacements of both lenses (Chung et al. 2009). Even if we know that our lens candidate is a member of a multiple system, it is often difficult to estimate its individual mass and hence the additional effect on the centroid shift.

The advantage of astrometric in comparison to photometric measurements is the opportunity to determine the mass, distance, and velocity of a lens independently. In photometric microlensing it is often only possible to measure the Einstein time which depends on all three quantities (Equation 6.10). If we observe the centroid shift trajectory, we can infer the Einstein radius of the lens. Additionally, astrometric measurements of the proper motion and parallax can solve the degeneracy problem. Therefore, the astrometric detection of the microlensing effect enables to determine the mass of the lens

$$M_{\text{L}} = 0.123M_\odot\frac{\theta_{\text{E}}}{\pi_{\text{LS}}} \tag{6.27}$$

with the use of the parallax of the lens source system ($\pi_{\text{LS}} = \pi_{\text{L}} - \pi_{\text{S}}$) and the Einstein radius to high

accuracies of a few percent (Paczynski 1998). Alternatively, if we can measure the angular distance between lens and source and know the unaffected source position, one could calculate the centroid shift of the microlensing event. We can obtain the most information and hence the best accuracy on the mass measurement with supplementary photometric observations. All described measurements are only possible if the lens is visible. For a dark lens, additional photometric detections are necessary for lens mass estimations. Regardless of whether the lens is visible or not, complementary photometric observations should be done when one measures an astrometric microlensing event. For this, a prediction of microlensing events and a microlensing alert system is reasonable.

6.3   Astrometric Microlensing Detections with Gaia

Gaia's astrometric instrument provides high positional and proper motion accuracies especially for bright objects. With an angular resolution of roughly 200 milliarcseconds (U. Bastian, priv. comm.), the satellite can not resolve the two individual images resulting from the astrometric microlensing effect. But from Gaia's data we can derive the light centroid shift of source objects up to microarcsecond scale. In this context, one has to be careful when working with resolutions and accuracies. Gaia is able to distinguish two close objects that have a small separation of about 200 milliarcseconds (angular resolution). Otherwise, each measured object has an uncertainty in its position (astrometric accuracy). For bright stars the errors on their position are of order microarcseconds.

For analyzing the positional displacements, we have to consider the astrometric accuracy of a single measurement instead of the end mission accuracy listed in Table 2.1. The astrometric accuracy of a single measurement depends on the brightness of the star, the object type, the extinction, and the position on the sky. de Bruijne (2009) presents performances for different spectral types of stars and different interstellar reddenings. Furthermore, he distinguishes between the along and across-scan direction for stars moving over the Astrometric Field CCDs. Quasar spectra are very different from stellar ones. Additionally, quasar spectra strongly depend on their redshifts. For our examination, it is suitable to use the positional accuracies already presented in Belokurov & Evans (2002). The astrometric accuracies for faint objects ($\gtrsim 15$ mag) described in Belokurov & Evans (2002) are similar to the standard errors for different stellar types (along-scan, without reddening) presented in de Bruijne (2009). We list the astrometric accuracies σ_a, used in our study, for magnitudes G between 10 and 20 mag in Table 6.1. One measurement is the combination of the astrometric information from nine CCDs of the Astrometric Field.

For several reasons, only about 2% of detected astrometric centroid shifts can be additionally observed as photometric event (Belokurov & Evans 2002). On the one hand Gaia's scanning law produces sets of measurements interrupted by measurement gaps. These gaps depend on the sky position but typically they have a duration of about two months. In many cases, high proper motion stars cause astrometrically detectable microlensing events. While the duration for astrometric microlensing events with

G [mag]	10	11	12	13	14	15	16	17	18	19	20
σ_a [μas]	30	30	30	40	60	90	150	230	390	700	1400

Table 6.1: Estimated astrometric accuracy for a single measurement of the Gaia satellite published in Belokurov & Evans (2002). We list the accuracy σ_a in dependence on the apparent magnitude G for a mean sky position.

high proper motion lenses amounts to several months, the timescale of the corresponding photometric event, the Einstein time, is of order days. Hence Gaia very likely would miss the source brightness amplification of a detected astrometric microlensing event. On the other hand Gaia can monitor astrometric microlensing events to much larger impact parameter than the related photometric one (Equation 6.9 and 6.17). To increase the number of microlensing events with both astrometric and photometric measurements, a microlensing alert system exists.

The Science Alert Development Unit, which is part of the CU5 (Coordination Unit: Photometric Processing), is responsible for analyzing different kind of science alerts. In addition to microlensing events, it also focuses on transients like supernovae, dwarf or classical novae, Gamma Ray Burst afterglows, M-dwarf flares, variable stars, asteroids or surprising events. To find or follow up transient events, the team compares current measurements with historic data and checks unexpected variations. The variability can be classified from Gaia's low-resolution spectra, the light curve, and cross-matching with stored data (Wyrzykowski & Hodgkin 2012). About 1,000 photometric microlensing events are expected to be observed by Gaia. These events are mainly located in the direction of the Galactic plane or bulge. Due to Gaia's scanning law, with typical observational gaps of several weeks, the majority of them should have Einstein times larger than $t_E = 30$ days (Belokurov et al. 2003). As mentioned above, the vast majority of existing photometric events have small Einstein times. If an astrometric microlensing event is detected by the alert system, the community will be informed to search for the complementary photometric microlensing event with selected ground based telescopes (Wyrzykowski & Hodgkin 2012).

Instead of using the alert system, we focus on another possibility to improve the amount of microlensing detections. We predict astrometric microlensing events for the duration of the Gaia mission by our microlensing program (Proft et al. 2011) considering star catalogs with high positional accuracies and information on proper motions. In the next chapter, we describe the approach for these astrometric microlensing predictions considering the characteristics of the satellite.

Chapter 7

Prediction of Astrometric Microlensing Events

The feasibility to predict astrometric microlensing events was first proposed by Paczynski (1995). He also emphasizes that one can observe the corresponding photometric microlensing events with ground-based telescopes. If one wants to predict astrometric microlensing candidates, one should search for high proper motion stars having event durations shorter than the space mission. In addition to this, faint lensing stars are suitable to avoid the luminous lens effect which decreases the light centroid shift. These high proper motion stars are usually a member of our solar neighborhood within a distance of about 100 parsec. Optimally, the astrometric deviation resulting from the microlensing effect increases for smaller lens distances. Additionally, for many high proper motion stars the parallax is known. In this case we can derive the lens distance to high accuracies. The precise knowledge of the lens distance significantly improves the centroid shift calculation.

Salim & Gould (2000) were the first who searched systematically for nearby astrometric microlensing events. The authors identified 178 astrometric microlensing candidates between 2005 and 2015 that could be observed with the Space Interferometry Mission (SIM). This mission was canceled in 2010 and the necessary astrometric accuracy of current telescopes is in general not sufficient to detect these 178 events. Since 2000 the positional and proper motion accuracies in suitable lensing catalogs considerably improved. In principle, using current astrometric catalogs the centroid shift predictions are more reliable, but one has to be careful because of stars that are wrongly assigned to high proper motion objects.

In Proft et al. (2011) we predict astrometric microlensing events between 2012 and 2019.[1] For this, we identified stars with large proper motion that are potential microlensing candidates. To verify the candidates, we checked their proper motion and calculated important properties like the centroid shift of the source position. This microlensing catalog contains 1118 candidates. However, we discovered that only 4% of the proper motions are correct, which leaves 43 astrometric microlensing events. The majority of these 43 events have small astrometric deviations below $\sim$100 microarcseconds (dark lens) or a bright lens that reduces the centroid shift of the source. Nine events could have strong astrometric

---

[1]We described the results of that paper (the microlensing events) in the diploma thesis Proft (2010). Afterwards, during the beginning of our work on this dissertation, we further improved the microlensing program and plotted additional diagrams. We published all results in Proft et al. (2011). In the following, we will clearly distingish between the work presented in Proft et al. (2011) and new research conducted after the work published in that paper. The new detected microlensing events are not published yet (April 2016).
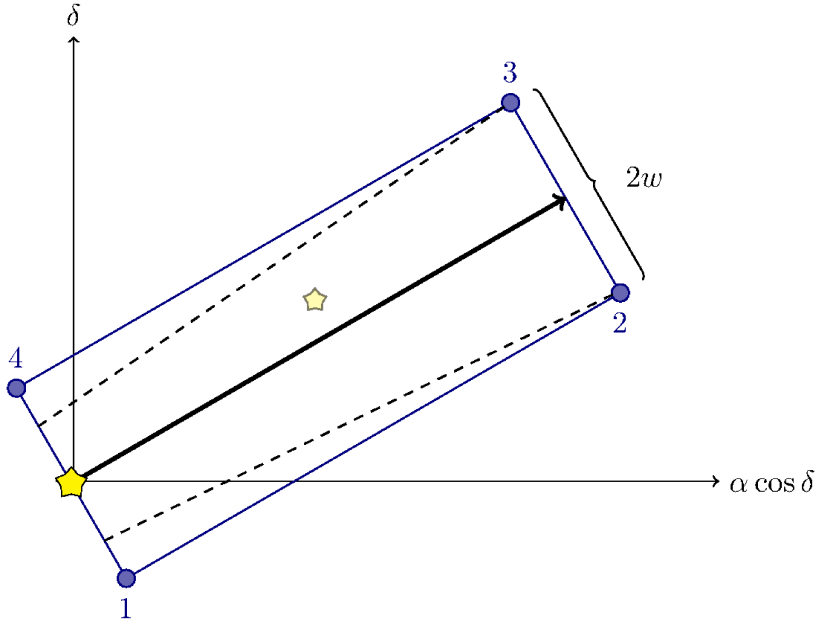
Figure 7.1: The diagram shows the trajectory of a high proper motion star for a given time interval (black arrow). Due to an increasing uncertainty in position and proper motion with time, we need to define a trapezium around the trajectory (dashed lines). For our program we can simplify it to a rectangle with corner points 1 to 4 characterized by the width $2w$. If the position of a background object (small star) is located in the rectangle, our program identifies the lens (big star) as candidate a for astrometric lensing (Proft et al. 2011).

deviations between 100 and 4000 microarcseconds. Especially two out of these nine microlensing events could lead to an astrometric microlensing event observable with Gaia.

In this chapter, we improve the search for astrometric microlensing events between January 2014 and December 2019. In our work, we always regard the output of our microlensing program as microlensing candidates and only after verifying the lens candidate proper motion we call them astrometric microlensing events. First, we describe the method that we apply to determine all astrometric microlensing candidates, the old events (Proft et al. 2011) and the new discovered candidates. Our first idea is to review the VLT (Very Large Telescope) instrument SPHERE (**S**pectro-**P**olarimetric **H**igh-contrast **E**xoplanet **RE**search) as microlensing detector. Afterwards, we perform a second improved study to identify astrometric microlensing events with the Gaia satellite. In Section 7.2, we present all resulting microlensing events additional to Proft et al. (2011) and calculate important lens and source quantities. At the end of this chapter, in Section 7.3, we discuss further opportunities to advance the prediction of astrometric microlensing events. From now on we denote our paper Proft et al. (2011) as P2011.

7.1   The Microlensing Program

In Figure 7.1, we present the main principle to detect a lensing star and a corresponding source object with our microlensing program. We give the position of the lens (big yellow star) in equatorial coordinates, where $\alpha \cdot \cos \delta$ presents the projection from a sphere to a plane. The uncertainty in the lens position and proper motion, which is given for the epoch 2000.0, increases with time. When the lens is moving between two epochs (e.g., 2008 and 2020), we have to consider this uncertainty by defining a width w. Hence the trajectory of the lensing star (black arrow) is surrounded by a certain trapezium.

Catalog	Sky Field	Magnitude	Stars in Field ($\mu > 0.15"$/year)
LSPM-NORTH	$\delta > 0°$	$V < 21$	$\approx 62,000$
PPMX	$0° > \delta > -30°$	$V < 15$	$\approx 109,000$
UCAC3	$-30° > \delta > -90°$	$8 < R < 16$	$\approx 477,000$
OGLEBG	Galactic Bulge	$11 < I < 18$	≈ 100

Table 7.1: The table presents the lensing catalogs (LSPM-NORTH, PPMX, UCAC3, and OGLEBG) used in our microlensing program together with the selected sky field, the limiting V magnitude, and the number of contained stars with large proper motion.

For simplicity, it it sufficient to use a rectangle instead of the trapezium considering the positional and proper motion uncertainties in 2020. The higher the proper motion of the lens the larger is the area of the rectangle and thus the microlensing probability. If a source object (small yellow star) crosses the rectangle, the microlensing program defines it as a lensing candidate. In general, the source object is a distant star with small proper motion. Hence we do not consider the source proper motion for identifying microlensing candidates, but we take it into account when calculating the microlensing parameters.

For our microlensing program we need suitable catalogs for lens and source stars. Source star catalogs should be complete all sky catalogs optimally up to Gaia's magnitude limit of $G \approx 20$ mag. Appropriate catalogs for lensing stars should contain stars with reliable proper motions larger than $\mu \gtrsim 0.15"$/year. Additionally, high positional accuracies of about 100 milliarcseconds and large proper motion accuracies of about 10 milliarcseconds per year in the selected lensing catalog are necessary to ensure good microlensing candidates. Like in P2011, we choose the PPMXL catalog of positions and proper motions on the ICRS from Roeser et al. (2010) as source catalog for the whole sky. As lensing catalogs we also select the LSPM-NORTH (Lepine & Shara 2005), PPMX (Roeser et al. 2008), UCAC3 (Zacharias et al. 2010), and OGLE Bulge (OGLEBG, Sumi et al. 2004) for different declinations. In Table 7.1, we list the selected celestial region, limiting V magnitude, and the number of stars for each lensing catalog. There exist several high proper motion catalogs with confirmed proper motions like NLTT (Luyten & Hughes 1980), LHS (Luyten 1979), or rNLTT (Salim & Gould 2003) that are not suitable as lensing catalogs for two reasons. First, old catalogs (e.g., LHS, NLTT) have large uncertainties in position and proper motion. Second, catalogs like the rNLTT with better astrometry are less complete than the selected lensing catalogs.

7.2 Astrometric Microlensing Events between 2014 and 2019

In P2011 we searched for astrometric microlensing events that are detectable with the Gaia satellite. In order to find new events, we apply the approach to another telescope. At the suggestion of Hans Martin Schmid from ETH Zurich, we want to find microlensing candidates for the VLT instrument SPHERE[2]. The main objective of this instrument is to discover and analyze giant extrasolar planets with the help of direct imaging. So far (February 16, 2016) 65 planets in 60 planetary system could be found by various telescopes using direct imaging[3]. Due to SPHERE's design and its positional accuracy of 1 milliarcsecond, it is also suitable to detect astrometric microlensing events.

---

[2]http://www.eso.org/sci/facilities/develop/instruments/sphere.html
[3]http://www.exoplanet.eu/

Schmid (2009) gives a list of 41 bright stars ($m_V < 10$ mag) with high proper motion larger than $\mu = 0.5''/yr$ that are observable with SPHERE. The objects are called ZIMPOL targets named for the **Z**urich **Im**aging **Pol**arimeter. The lensing catalogs LSPM-North, UCAC3, and PPMX, used in our microlensing program, contain these stars. A large fraction of the 41 objects have V< 6 mag which are mainly too bright for Gaia. In infrared the instrument can search for a faint background star ($m_V \lesssim 21$ mag) around a guide star ($m_V \lesssim 10$ mag) with a radius of 7 arcseconds and in visual/red light up to about 4 arcseconds. Considering all of these parameters, we use the lens and source catalogs of our previous study (P2011), a limiting lens magnitude of $m_V = 11$ mag and a rectangle width of $w = 7''$. Because the astrometry is more accurate in our previous lens catalogs, we do not directly take the list of ZIMPOL targets. But in doing so, we have to check afterwards whether the new microlensing candidates are a member of the ZIMPOL targets. Furthermore, we could identify additional guide stars working as lens not listed in the ZIMPOL sample. Although the 41 ZIMPOL targets have large proper motions, which increases the chance for a potential microlensing event, a sample of 41 objects is very small, and hence it is not very likely to predict many microlensing candidates with ZIMPOL stars as lenses.

Our first query with SPHERE parameters results in 50 astrometric microlensing candidates between 2014 and 2019. The potential lensing stars have minimal projected distances between 9 and 6019 milliarcseconds. To know whether ZIMPOL objects are among these candidates, we do a crossmatch of the 41 targets with the candidate list of 50 objects. The crossmatch provides no overlap between the two tables. Thus, we do not find astrometric microlensing candidates observable with SPHERE using the ZIMPOL targets as lenses. However, among the 50 candidates, there could be additional targets causing astrometric microlensing events observable with SPHERE although they are not in the ZIMPOL list.

We discover that 12 microlensing candidates (not confirmed as events yet) have minimal lens source distances smaller than 0.7 arcseconds. Because we chose a rectangle width of $w = 0.7''$ in P2011, these candidates should have been already detected before. We have several hypotheses why there are additional microlensing candidates that were not covered by the previous request:

- We should select the rectangle width w larger than 0.7"/year due to large errors in given positions and proper motions.

- Sources could have a proper motion that is not negligible for the event prediction.

- The minimal distance of lens and source could be larger than 0.7".

We will now inspect the new candidates to infer true events and analyze in detail why the individual microlensing events were not found in the previous study. Furthermore, we estimate the lens mass and distance to infer the maximal centroid shift and examine the additional events for observability with SPHERE and the Gaia satellite.

7.2.1 Inspection of New Microlensing Candidates

In P2011 we discovered that the majority, 96% in our total sample, of high lens proper motions are spurious. Due to this, we had to check the supposed candidates from our program with two color diagrams and the proper motion by eye. We "blinked" more than 100 objects using pictures from different surveys in the Aladin Sky Atlas (Bonnarel et al. 2000; Boch & Fernique 2014). In the same way, Lepine & Shara (2005) built the catalog LSPM-North and hence we always measured correct proper motions for

LSPM-North lenses. However, for PPMX and UCAC3 only these lensing stars were true high proper motion objects which are already known in high proper motion catalogs (e.g., LHS, NLTT, or rNLTT). Hence we checked every microlensing candidate with the Simbad Astronomical Database (Wenger et al. 2000) for affiliation to one of the high proper motion catalogs. Furthermore, because of crowding in the Galactic plane, we could not validate OGLEBG stars, which are a small sample of candidates. Following this procedure, we are analyzing the 50 new supposed astrometric candidates. After excluding one old microlensing event (listed in P2011) and another true event which was presented twice, we can verify 14 new microlensing events ("'1. Sample'"). Thus, for our bright lenses, the fraction of stars with wrong high proper motion amounts to 68% (34 out of 50 stars). This value is much better than the 96% of erroneous candidates of our old study when we considered bright and faint lenses ($m_V < 21$ mag for northern and $m_V \lesssim 15$ for southern sky). We emphasize that one has to be careful when choosing a large rectangle width w for fainter lensing stars. The amount of theoretical microlensing candidates would increase linearly and one has to confirm much more stellar proper motions. Additionally, for the majority of events the centroid shift decreases to a value that is most likely not measurable by the telescope.

In the following, we calculate the maximal source centroid shift and further microlensing quantities for the 14 new microlensing events that are important to make a statement on the detectability with SPHERE and Gaia. To infer the maximal source centroid shift, we have to estimate the distance of lens and source, and the lens mass.

The most accurate method to calculate the lens distance is to use its trigonometric parallax. But we can find information on the parallax only for few lenses with the help of Simbad. If one does not know the stellar parallax, one has to calculate the absolute magnitude M of a star. Together with its apparent magnitude m, we can determine the distance r by the distance modulus (e.g., Weigert et al. 2006)

$$m - M = 5\log\left(\frac{r}{1\,\mathrm{pc}}\right) - 5. \tag{7.1}$$

If we have the stellar parallax, we can substitute it with the radius and have

$$M_V = m_V + 5\log(\pi) + 5. \tag{7.2}$$

In case Simbad contains the information of the spectral type and luminosity class of our lens, we estimate the absolute magnitude from a Hertzsprung-Russel-diagram (e.g., Kaler 1994). Otherwise we determine these properties with the method of reduced proper motions and infrared magnitudes J, H, and K given in the 2MASS catalog (Cutri et al. 2003). In the method of reduced proper motions one uses the effect that nearby stars on average have larger proper motions. Hence instead of an absolute magnitude M_V, we have a magnitude H_V that depends on the proper motion μ (Jones 1972; Salim & Gould 2000; Lepine & Shara 2005):

$$H_V = m_V + 5\log(\mu) + 5. \tag{7.3}$$

In Figure 7.2, we plot a reduced proper motion diagram for a fraction of 10,000 Hipparcos stars as red crosses. We selected these stars to indicate the main sequence and giant branch of the Hertzsprung-Russel diagram. Our 12 lensing stars (blue triangles), that cause 14 astrometric microlensing events, are in the area of M, K, or G dwarfs. For a smaller distinction of an individual spectral type, we calculate the colors J-H, H-K, and J-K. Bessell & Brett (1988) list color tables for subdivided spectral classes for dwarfs and
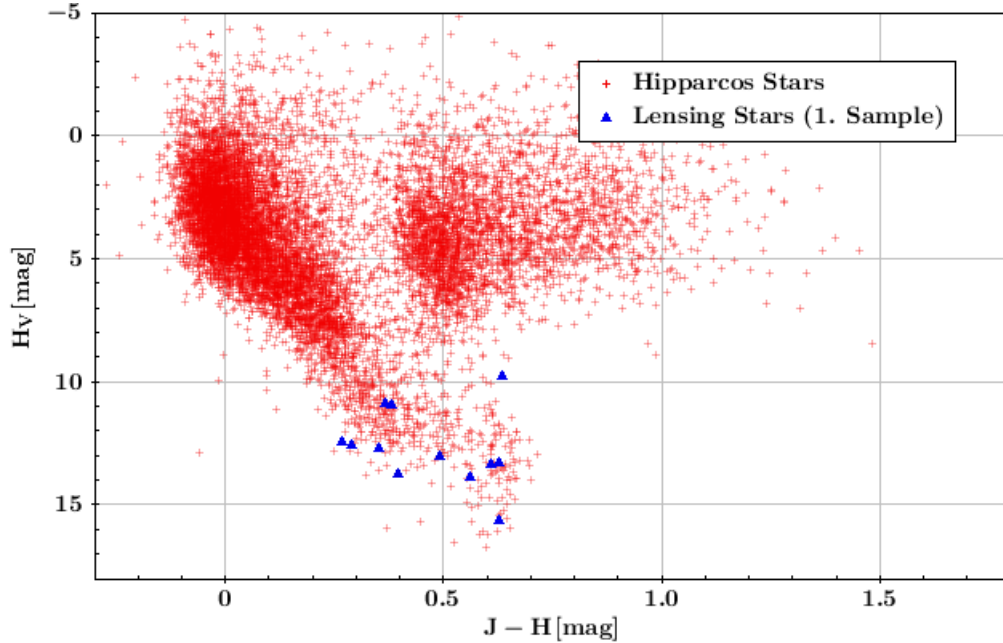
Figure 7.2: The reduced proper motion diagram shows the magnitude H_V against the color J-H for our new lensing stars (blue triangles) and a selection of 10,000 Hipparcos stars (red crosses) which indicate the Hertzsprung-Russel diagram. The 12 lensing stars are on the main sequence (M, K, or G dwarfs) and they are responsible for 14 microlensing events between 2014 and 2019.

giants. We can estimate the mass of our lensing stars from its determined spectral type and luminosity class, e.g., a M2 dwarf has a mass of $M_L \approx 0.4 M_\odot$. Together with the information on its distance to the sun, inferred from the method of reduced proper motions or from the parallax, we calculate the Einstein radius (Equation 6.1). Because the distance to the source is in general not available, we assume the typical case of a distant source. Now we are able to evaluate the source centroid shift and can make a first statement on the detectability.

We present the 14 verified microlensing events in Table 7.2 together with relevant lens and source parameters. For two events, #2 and #13, we calculate maximal centroid shifts equal or larger than SPHERE's positional accuracy of 1 milliarcsecond. But depending on the number of consecutive observations, the accuracy threshold (similar to equation 6.20) is higher. Furthermore, for objects that are not member of the ZIMPOL targets, it is not clear yet whether they are suitable as guide stars. The first event (object #2), for example, consists of a lens with magnitude $m_V = 10.5$ mag which is slightly too faint for being a guide star. The second event (object #13) has a maximal centroid shift only equal to SPHERE's accuracy. However, the uncertainties in the centroid shift and date of closest approach are huge. On the one hand the events could be measurable considering the errors, on the other hand time uncertainties of half a year or more are problematic to detect predicted events with SPHERE. We suggest to wait for the first Gaia data release appearing in summer 2016 to repeat the investigation.

For lens number #2, #5, #9, and #13 we estimated maximal centroid shifts of $\delta\theta_c = 1.876$ mas, 0.128 mas, 0.583 mas, and 1.018 mas, respectively. Considering the source brightness (i.e. the astrometric accuracy), these events could lead to a detectable astrometric microlensing event with the Gaia satellite. However, we do not find these microlensing events in our old query and have to investigate possible explanations. But before we can do this, we check whether there are more neglected microlensing
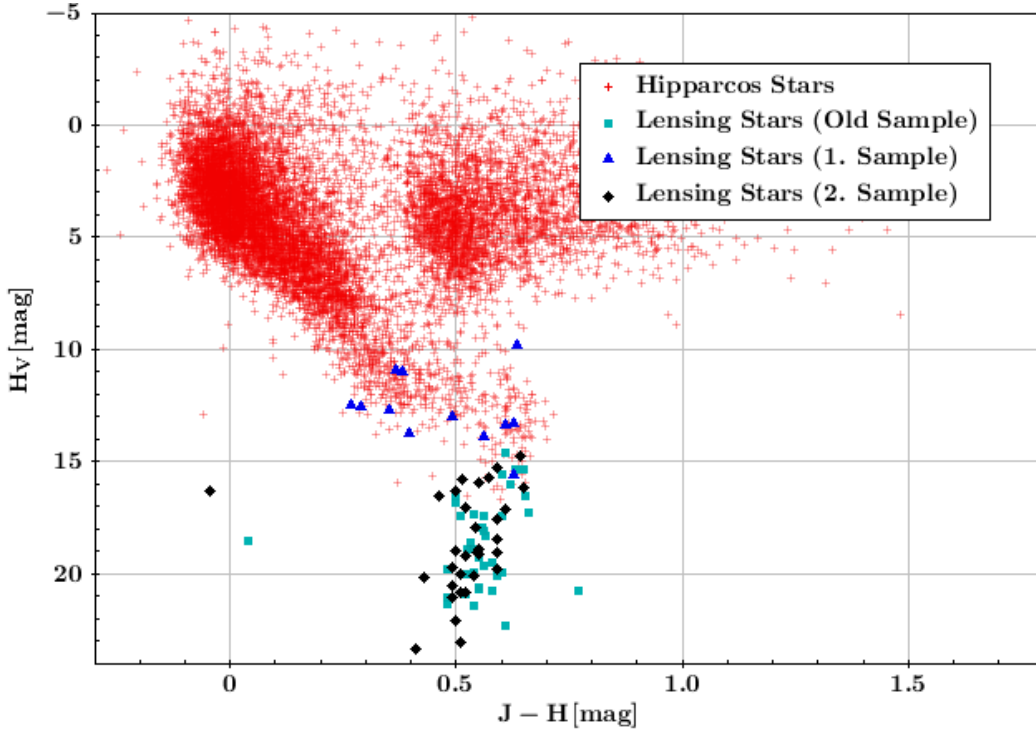
Figure 7.3: Similar reduced proper motion diagram as Figure 7.2. It presents a selection of 10,000 Hipparcos stars (red cross), our old microlensing events (cyan square), and the new microlensing events from the SPHERE request (blue triangle) and the additional request (black rhombus).

candidates for Gaia.

To be sure that we are not missing more microlensing candidates, we apply a second search. For this, we include also faint lenses (magnitudes given in column three of Table 7.1) and select a rectangle width of $w = 2$". We investigate this second analysis and exclude the results which are already in Table 7.2 and the events presented in P2011. To quickly check the proper motion of nearly 1,000 lens candidates, we checked with the help of Simbad whether the star is a member of a specific high proper motion catalog, e.g., LSPM-North, LHS, or NLTT. After the validation of lens proper motions, we can confirm 36 additional astrometric microlensing events between 2014 and 2019 which we did not find with the first Gaia search. In Table 7.3 and 7.4, we list the resulting events (#15 to #50) continuing the enumeration and the chosen quantities of the previous events presented in the Table 7.2. Due to the large rectangle width, there are many events with small centroid shifts not measurable with Gaia. However, we find two astrometric microlensing events (boldface, #36 and #43) with maximal centroid shifts of $\delta\theta_c = 0.176$ mas and 0.119 mas, respectively. These positional displacements could be sufficient for Gaia because of their bright source stars which facilitate high positional accuracies.

Our previous search, described in P2011, was biased towards to faint M dwarfs. On the other side, the fraction of new discovered microlensing events from our search for SPHERE ("1. Sample" in Figure 7.2 and 7.3) is biased towards higher masses and magnitudes on the main sequence of the Hertzsprung Russel diagram. One can explain this effect with the chosen magnitude limit of $m_V < 11$ mag for SPHERE lenses. The additional microlensing events from our second search ("2. Sample" in Figure 7.2 and 7.3) are in the same region as the old sample on the Hertzsprung Russel diagram. We show the reduced proper motion diagram for all event samples together with 10,000 Hipparcos stars in Figure 7.3. The

microlensing events of the old sample are between 2012 and 2019. Since Gaia started to observe in 2014, we only consider events from 2014 to 2019 for the two new queries. For four lenses of our old sample, we do not have information on the infrared magnitudes, two of these objects are white dwarfs. Combining all our queries, we find 93 astrometric microlensing events, 81 of them are between 2014 and 2019. Out of 81 events, 50 are new discoveries and 31 are a member of the old sample. The majority of detected microlensing events have insignificant source centroid shifts, hence an observation with Gaia is very unlikely.

In this subsection, we presented newly discovered astrometric microlensing events between 2014 and 2019 and gave a first statement on their detectability with Gaia. In total, there are 50 new determined microlensing events, but only six of them could be possible to observe. In the following, we explore these six promising events (#2, #5, #9, #13, #36, and #43) and display their calculated quantities.

#	lens ID	α_{L}	δ_{L}	μ_{L}	$m_{\mathrm{V,L}}$	$t_{\min}$	$d_{\min}$	$\delta\theta_{\mathrm{c}}$	$m_{\mathrm{V,S}}$
		(deg)	(deg)	("/yr)	(mag)	(yr)	(")	(mas)	(mag)
1	PPMX 231909.0 -383528	349.78764	-38.59128	0.130	10.4	2015.39	0.287	0.261	18.0
2	**UCAC3 264.26526 -044.31923**	**264.26526**	**-44.31923**	**1.067**	**10.5**	**2015.83**	**0.295**	**1.876**	**13.8**
3	LSPM J2045+4429	311.26706	44.49900	0.410	10.8	2016.98	1.466	0.158	20.1
4	UCAC3 068.35718 -038.30309	68.35718	-38.30309	0.392	10.8	2017.26	1.216	0.043	20.0
5	**LSPM J0216+6457**	**34.20507**	**64.95261**	**0.350**	**8.3**	**2017.50**	**1.371**	**0.128**	**15.1**
6	UCAC3 068.35718 -038.30309	68.35718	-38.30309	0.392	10.8	2017.94	2.381	0.022	19.5
7	UCAC3 243.45232 -057.57044	243.45232	-57.57044	1.482	7.2	2018.21	4.020	0.102	16.6
8	UCAC3 243.45232 -057.57044	243.45232	-57.57044	1.482	7.2	2018.32	3.050	0.134	17.7
9	**LSPM J2139+6017**	**324.81729**	**60.28381**	**0.296**	**10.4**	**2018.50**	**0.178**	**0.583**	**18.2**
10	LSPM J0237+4359	39.42264	43.99292	0.300	10.2	2018.76	5.961	0.010	15.5
11	UCAC3 014.37973 -043.55476	14.37973	-43.55476	0.206	10.9	2019.27	1.368	0.029	19.9
12	UCAC3 011.45119 -041.90913	11.45119	-41.90913	0.241	7.9	2019.77	5.108	0.062	8.5
13	**UCAC3 310.57823 -052.69926**	**310.57823**	**-52.69926**	**1.067**	**8.3**	**2019.79**	**0.353**	**1.018**	**19.1**
14	UCAC3 155.60251 -060.17715	155.60251	-60.17715	0.439	10.2	2019.99	3.811	0.054	14.9

Table 7.2: We present 14 astrometric microlensing events between 2014 and 2019 from our search for the VLT instrument SPHERE. We excluded the old events presented in P2011. Given are the lens ID, the lens coordinate at equinox J2000.0 (α_{L}, δ_{L}), the apparent magnitude of lens and source ($m_{\mathrm{V,L}}$, $m_{\mathrm{V,S}}$), the lens proper motion (μ_{L}), the time at closest approach ($t_{\min}$), the angular distance of lens and source at closest approach ($d_{\min}$), and our estimated maximal centroid shift of the source image ($\delta\theta_{\mathrm{c}}$). The lensing stars are not members of the SPHERE high proper motion targets, and hence not observable with SPHERE. By studying the expected maximal source centroid shift, we find that some of these microlensing events are in principle measurable with Gaia (boldface lenses #2, #5 #9, #13).

#	lens ID	α_L (deg)	δ_L (deg)	μ_L ("/yr)	$m_{V,L}$ (mag)	t_{min} (yr)	d_{min} (")	$\delta\theta_c$ (mas)	$m_{V,S}$ (mag)
15	LSPM J1953+2219	298.26630	22.32357	0.420	16.6	2014.05	1.827	0.012	16.8
16	LSPM J1548+5939	237.01520	59.65041	0.443	13.9	2014.14	1.636	0.049	20.7
17	LSPM J0258+5354	44.68924	53.91312	0.549	16.4	2014.29	0.668	0.014	19.7
18	LSPM J2140+3703	325.05325	37.05792	0.502	11.3	2014.56	0.962	0.101	18.1
19	LSPM J1918+1728	289.65414	17.46673	0.635	19.1	2014.71	0.964	0.007	18.0
20	LSPM J1757+1502	269.37421	15.04320	0.449	15.8	2014.82	1.935	0.016	18.9
21	LSPM J1918+1728	289.65414	17.46673	0.635	19.1	2014.94	0.713	0.009	18.9
22	LSPM J1425+5319	216.34837	53.32272	0.587	12.7	2015.02	0.757	0.157	21.0
23	UCAC3 025.58508 -031.55999	25.58508	-31.55999	0.749	16.7	2015.43	1.533	0.015	19.8
24	PPMX 073840.9 -211328	114.67066	-21.22458	0.657	11.7	2015.53	0.559	0.412	20.3
25	LSPM J1909+2206	287.29639	22.11367	0.532	13.4	2015.73	0.461	0.078	18.8
26	LSPM J0711+4329	107.79767	43.49946	0.675	15.9	2015.81	0.744	0.046	17.5
27	LSPM J2003+3931	300.78983	39.52057	0.420	15.8	2015.81	1.738	0.019	18.4
28	LSPM J0550+1719	87.60056	17.32189	0.579	15.4	2016.04	0.783	0.016	19.0
29	UCAC3 245.67063 -048.65557	245.67063	-48.65557	0.759	11.5	2016.10	1.629	0.094	16.0
30	LSPM J0350+4325	57.55788	43.42790	1.440	14.4	2016.26	1.512	0.067	20.7
31	UCAC3 257.06166 -034.60627	257.06166	-34.60627	0.861	16.2	2016.52	0.406	0.070	19.0
32	PPMX 174317.5 -183118	265.82307	-18.52191	0.576	11.9	2016.69	0.297	0.443	19.5
33	LSPM J0533+3837	83.33482	38.62088	0.555	17.1	2016.92	0.592	0.026	20.2

Table 7.3: We list the additional astrometric microlensing Events #15 to #33 between 2014 and 2019. For this, we already excluded our old candidates presented in P2011 and the 14 new events of Table 7.2. The presented parameters and units are the same used in Table 7.2. In comparison to the microlensing query of P2011, we selected a rectangle width of $w = 2$". The additional microlensing candidates #34 to #50 are given in table 7.4.

#	lens ID	α_L (deg)	δ_L (deg)	μ_L ("/yr)	$m_{V,L}$ (mag)	t_{min} (yr)	d_{min} (")	$\delta\theta_c$ (mas)	$m_{V,S}$ (mag)
34	PPMX 184420.6 -301357	281.08621	-30.23251	0.546	12.6	2016.93	1.415	0.024	17.8
35	UCAC3 257.06166 -034.60627	257.06166	-34.60627	0.861	16.2	2016.96	1.573	0.018	18.0
36	**UCAC3 287.64001 -041.54744**	**287.64001**	**-41.54744**	**0.676**	**15.7**	**2016.98**	**0.201**	**0.176**	**16.7**
37	UCAC3 342.16002 -031.14475	342.16002	-31.14475	0.452	12.0	2017.13	0.374	0.512	20.0
38	PPMX 171126.7 -144753	257.86148	-14.79824	0.429	13.1	2017.17	1.691	0.272	19.5
39	LSPM J0510+1924	77.66283	19.40199	0.831	18.8	2017.24	0.695	0.040	19.0
40	UCAC3 125.76490 -044.74732	125.76490	-44.74732	0.414	16.0	2017.51	1.757	0.016	17.9
41	LSPM J1507+0052	226.77554	0.86992	0.460	18.8	2017.55	1.357	0.006	20.1
42	LSPM J1847+2820	281.88803	28.34961	0.472	18.9	2017.74	1.583	0.005	20.0
43	**LSPM J1914+1919**	**288.66318**	**19.31762**	**0.749**	**11.6**	**2017.95**	**1.428**	**0.119**	**14.9**
44	UCAC3 009.98353 -030.54628	9.98353	-30.54628	0.506	14.5	2018.04	1.301	0.045	21.3
45	UCAC3 311.11620 -041.39763	311.11620	-41.39763	0.504	15.0	2018.53	0.667	0.062	16.9
46	LSPM J2135+5428	323.78958	54.47421	0.410	16.0	2018.69	1.232	0.024	19.8
47	LSPM J1959+2722	299.84644	27.38012	0.411	14.5	2018.79	1.797	0.012	18.7
48	LSPM J1941+3239	295.36527	32.66413	0.697	14.8	2019.08	1.207	0.063	18.3
49	LSPM J1514+1130	228.55814	11.51629	0.440	13.0	2019.39	1.943	0.054	21.0
50	LSPM J0614+1509	93.50661	15.16511	1.443	14.7	2019.82	1.560	0.073	15.2

Table 7.4: We list the additional astrometric microlensing Events #34 to #50 between 2014 and 2019. For this, we already excluded our old candidates presented in P2011 and the 14 new events of Table 7.2. The presented parameters and units are the same used in Table 7.2 and 7.3. In comparison to the microlensing query of P2011, we selected a rectangle width of $w = 2$". The two boldface rows (lens #36 and #43) are promising microlensing events for a detection with the Gaia satellite.

7.2.2 Confirmed Microlensing Events Observable with Gaia

In the previous subsection, we discovered six new microlensing events that have a maximal centroid shift (dark lens, considering the error) larger than the positional accuracy σ_a of Gaia. Considering their event durations t_{ast} (Equation 6.19) and centroid shifts in case of a luminous lens $\delta\theta_{c,lum}$ (Equation 6.23), one gets a more realistic perspective on the detectability with Gaia. For all six astrometric microlensing events we calculate important lens and source properties presented in Table 7.5 together with known coordinates and magnitudes of all lenses and sources. Only lens #9 (numbering is the same as in Table 7.2, 7.3 and 7.4) has an angular distance smaller than 200 milliarcseconds to the source and Gaia is not able to resolve both. Therefore, we determine the centroid shift considering the luminous lens effect $\delta\theta_{c,lum}$ and the centroid shift when lens and source achieve the separation of Gaia's typical angular resolution $\delta\theta_{c,res}$. The source objects of our six microlensing events are always fainter than their lens and it is not possible to infer the source types and their distance from archives.

As mentioned above, we checked the microlensing candidates with Simbad for affiliation to one of the old high proper motion catalogs to exclude wrongly assigned high proper motion stars. To verify the six lens proper motions more precisely and to confirm the corresponding astrometric microlensing events, we use the program Aladin. In Figure 7.4, we demonstrate it for the excellent event #2. We select the position of the source at epoch J2000.0 in the center of our image (red arrow). Then we search for photographies from different sky surveys or atlases around this coordinate to see the movement of lens and source with time. In this case, pictures from ESO (1986), AAO (1992), SERC (1994), and 2MASS (1999) are available. In every single panel we mark the lensing star with a blue cross visible in all other images as well. The source proper motion is very small; hence the source is always close to the red arrow. For all six images we apply the same procedure and can confirm the value of the lens proper motion. Furthermore, we are also able to validate the source for events #2, #5, #9, and #13. Due to the faint sources of event #36 and #43 ($m_{V,S}$ =18.2 mag, 19.1 mag), we can not confirm the source objects by having a look on pictures from previous sky surveys.

Out of the six events, lens #2 is the most promising event for an observation with the Gaia satellite. It is the only new microlensing event that has a maximal centroid shift (without considering the huge errors) larger, even 20 times larger, than the accuracy threshold θ_{min} (Equation 6.20) described in Chapter 6.2. With a distance of 5 parsec, the lens is very close to the sun and hence the astrometric microlensing signal is very high ($\delta\theta_{c,max} = 1.876 \pm 3.094$ mas). The large centroid shift error is caused by the positional and proper motion uncertainty given in the catalogs and the uncertainty by determining the lens distance and mass. Due to a bright source star ($m_V = 13.8$ mag), Gaia has an astrometric accuracy (single measurement) of $\sigma_a = 50$ mas and an accuracy threshold of $\theta_{min} = 0.095$ mas. Although the astrometric timescale of about eight years is very long, the great astrometric accuracy and the large centroid shift would enable a good measurement if Gaia observes the event. Furthermore, the expected date of the closest approach for lens and source is within the mission, expected to have been at the end of 2015.

Having a maximal centroid shift of $\delta\theta_{c,max} = 0.176 \pm 0.423$ mas but a necessary positional Gaia accuracy of $\sigma_a = 0.200$ mas, #36 is the most unlikely microlensing event. Furthermore we can give a statement on the date of closest approach only with an error of eleven months. Events #5 and #43 have a small centroid shift as well ($\delta\theta_{c,max} = 0.128$ mas, $\delta\theta_{c,max} = 0.119$ mas) but considering the brighter source objects, σ_a amounts to 0.095 mas and 0.085 mas, respectively. Moreover, because of parallax information,

the centroid shift errors are very small. Events #9 and #13 have large centroid shifts ($\delta\theta_{c,res} = 0.520\,\text{mas}$, $\delta\theta_{c,max} = 1.018\,\text{mas}$) that are higher than Gaia's positional accuracy. Because of faint sources, the centroid shifts of both events are still smaller than Gaia's accuracy thresholds of $\theta_{min} = 0.854\,\text{mas}$ and $\theta_{min} = 1.018\,\text{mas}$, respectively.

Investigating the properties of all six potential microlensing events, we find several reasons for their absence in our old query from P2011. The events #5 and #43 have minimal projected distances between lens and source larger than the chosen rectangle width $w = 0.7''/yr$ ($\theta_{min} = 1.37''/yr$, $\theta_{min} = 1.43''/yr$). Three predicted events (#2, #9, and #13) have a considerable source proper motion. As mentioned before, we used the source proper motion for calculating the angular distance of lens and source but not to define the microlensing candidates with the program. Only for event #36 we do not find an explicit argument.

For completeness, we present selected old astrometric microlensing events published in P2011 with maximal centroid shifts larger than Gaia's astrometric accuracy in the appendix (Table 8.1). Due to Gaia's observing beginning, we excluded the events before 2014. The first three lenses could have had their closest approach to the source in early 2014. Hence Gaia could miss the astrometric signal at closest approach for these cases. One can read a detailed discussion of the old two best events P2011-18 and P2011-20 in P2011. Combining our previous and new microlensing query, we find eleven microlensing events (six new and five from P2011) between 2014 and 2019. Out of the eleven, three astrometric microlensing events have very promising centroid shifts considering Gaia's accuracy threshold.

The Einstein time for all eleven events is smaller than two weeks. Hence it is unlikely that Gaia observers the corresponding photometric microlensing signal. Additionally, for large impact parameters $u \gg 1$, like our new events and P2011-34, the magnitude shift is smaller than the photometric threshold of Gaia. Hence photometric observations from ground are necessary to get more information on the individual events. For this, the science alert team informs the community when Gaia measures an astrometric event. Furthermore, one can follow up our predicted astrometric microlensing events considering the calculated times at closest approach. However, the uncertainties in our estimated centroid shifts and dates at closest approach are too large to devise an optimal observing strategy currently. An idea could be to use the measurements of Gaia's first data release. With these first data one can improve the properties for bright lensing stars ($m_V \lesssim 12\,\text{mag}$). Further data releases of Gaia enable the revision also for fainter lensing star quantities.

#	2	36	5	43	9	13
Lens ID	**UCAC3 264.26 526-044.31923**	UCAC3 287.64 001-041.54744	LSPM J0216 +6457	LSPM J1914 +1919	LSPM J2139 +6017	UCAC3 310.57 823-052.69926
α_L (deg)	**264.26526**	287.64001	34.20507	288.66318	324.81729	310.57823
δ_L (deg)	**-44.31923**	-41.54744	64.95261	19.31762	60.28381	-52.69926
t_{min} (yr)	**2015.83±0.46**	2016.98±0.93	2017.50±0.39	2017.95±0.26	2018.50±0.40	2019.79±0.74
ϑ_{min} (")	**0.295±0.499**	0.201±0.479	1.371±0.178	1.428±0.198	0.178±0.257	0.353±0.485
μ_L ("/yr)	**1.067**	0.676	0.468	0.749	0.296	1.067
$m_{V,L}$ (mag)	**10.5**	15.7	8.3	11.6	10.4	8.3
MK	**M3.5**	M4	G8	M2	G8	K7
M_V (mag)	**11.3**	11.5	6.0	10.5	5.9	8.5
M_L ($M_\odot$)	**0.35**	0.30	0.85	0.40	0.85	0.54
D_L (pc)	**5.1**	68.7	39.4	19.1	66.2	12.1
θ_E (mas)	**23.676**	5.962	13.243	13.059	10.222	19.016
u_0 (θ_E)	**12.5**	33.7	103.6	109.4	17.4	18.6
σ_a (mas)	**0.050**	0.200	0.095	0.085	0.450	0.730
θ_{min} (mas)	**0.095**	0.379	0.180	0.161	0.854	1.385
$\delta\theta_{c,max}$ (mas)	**1.876±3.094**	0.176±0.423	0.128±0.020	0.119±0.020	0.583±0.832	1.018±1.389
$\delta\theta_{c,res}$ (mas)	**-**	-	-	-	0.520±0.053	-
$\delta\theta_{c,lum}$ (mas)	**-**	-	-	-	0.000±0.001	-
t_E (days)	**8**	3	10	6	13	7
t_{ast} (days)	**3176**	79	1191	809	237	140
μ_S ("/yr)	**0.073**	0.003	0.015	0.010	0.217	0.063
$m_{V,S}$ (mag)	**13.8**	16.7	15.1	14.9	18.2	19.1

Table 7.5: We give the six new astrometric microlensing events between 2014 and 2019 ordered by date t_{min} with centroid shifts potentially measurable by Gaia that are not published in P2011. The event numbering is the same as in Table 7.3. The listed quantities are: lens coordinates (α_L, δ_L), time and angular distance at closest approach (t_{min}, ϑ_{min}), lens and source proper motion (μ_L, μ_S), lens and source apparent magnitude ($m_{V,L}$, $m_{V,S}$), lens spectral type (MK), lens absolute magnitude (M_L), lens distance (D_L), angular Einstein radius (θ_E), impact parameter (u_0), positional accuracy (σ_a), accuracy threshold for consecutive Gaia observations (θ_{min}), maximal centroid shift for a dark lens ($\delta\theta_{c,max}$), maximal centroid shift for a luminous lens ($\delta\theta_{c,res}$), centroid shift at $\theta = 200\,\text{mas}$ ($\delta\theta_{c,lum}$), and typical timescale of a photometric and the corresponding astrometric microlensing event (t_E, t_{ast}). We emphasize the most promising event (#2).
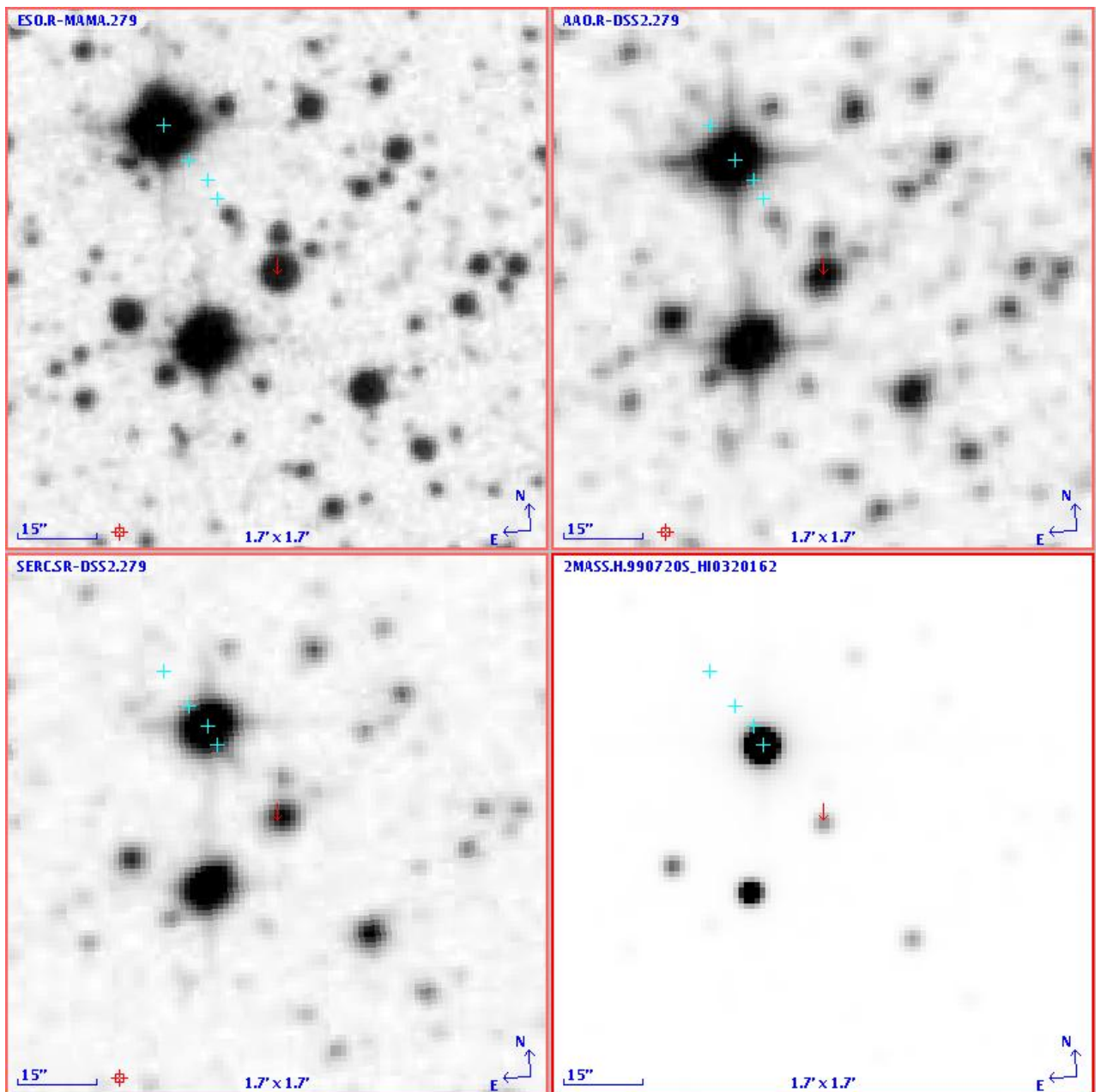
Figure 7.4: The pictures show the lens and source of the new most promising astrometric microlensing event #2 for four different surveys in 1985, 1991, 1996, and 1999. We used the program Aladin to produce the images and to indicate the lens and source positions. The red arrow gives the position of the source at epoch J2000.0. Due to the small source proper motion, we can see the source close to this position in all four images. In every picture we mark the lens position with a blue cross to see the movement of the star with increasing time. With these images we can confirm the lens proper motion of 1.1"/yr and the corresponding microlensing event.

7.3 Conclusions

We predicted astrometric microlensing events and checked their observability with the VLT instrument SPHERE and the Gaia satellite. For this analysis, we considered our previous microlensing study published in P2011. First, we wanted to find microlensing candidates for the VLT instrument SPHERE. Due to its magnitude limit of $m_V \approx 10\,\mathrm{mag}$ for guide stars, only a small sample of potential lensing stars were available (ZIMPOL targets and stars with $m_V \lesssim 10\,\mathrm{mag}$) for our actual microlensing search. We did not find candidates with ZIMPOL targets as lenses, but the two stars UCAC3 264.26526-044.31923 (#2) and UCAC3 310.57823-052.69926 (#13) could cause astrometric microlensing events observable with the VLT instrument. Unfortunately, one guide star as lens could be too faint ($m_V = 10.5\,\mathrm{mag}$) and the uncertainties of the calculated centroid shifts and dates at closest approach are huge. For a realistic search of predicted events with SPHERE, more accurate data is necessary. We suggested to repeat the study when the first data release of Gaia measurements is available.

In the first actual search, we found microlensing candidates which should be already in our old request for Gaia events. By increasing the rectangle width for the microlensing search from $w = 0.7''$ to $w = 2''$, we identified a large number of new candidates. Checking the new candidates for correct proper motion, we validated 50 new microlensing events. Similar to P2011, we calculated important quantities like the maximal centroid shift and the centroid shift with the luminous lens effect. Out of the 50 events, we discovered six astrometric microlensing events that could be measurable within the Gaia mission (2014 to 2019). Together with the already predicted events from P2011 in this timescale, we found eleven events. For several of the eleven events the measurability is marginal because of the luminous lens effect or large errors in the centroid displacement. Out of the eleven, two already published events and one new discovered microlensing event are very likely to happen due to their advantageous lensing parameters like measurable centroid shifts of several milliarcseconds. For several reasons, we did not find the complete list of microlensing candidates before. First, to produce the list of microlensing candidates, we did not consider the source proper motion, but we used it afterwards to calculate the minimal angular distance between lens and source. Second, by increasing the rectangle width, we got two astrometric microlensing events with minimal angular lens to source distance of $\vartheta_{\min} \approx 1.4''$.

Chapter 8

Summary and Perspectives

The Gaia satellite had its successful launch and commissioning during our work on this thesis. The main research mission has started in July 2014 and will continue until 2019 or even 2020. The final catalog, expected in 2022, will contain one billion stars and other celestial objects in the Milky Way offering very precise information on their positions, proper motions, and magnitudes. Since the beginning of observations, a few unexpected problems are occurring. For example, the satellite is getting additional stray light from the sun and other astronomical sources which reduces the magnitude limit for detections with the high-resolution spectra by one order of magnitude. We adapted our analysis accordingly.

In this thesis, we contribute to two different kinds of research questions with respect to the Gaia mission. In the first part, we showed the opportunities to explore the spectra of quasars with Gaia's blue and red photometers and with Gaia's radial velocity spectrograph. In the second part, we predicted astrometric microlensing events of nearby stars by improving our published stellar microlensing search (Proft et al. 2011). We now summarize our methods and main results of these two research questions. Afterwards, we present the perspectives from Gaia's preliminary data releases and its final catalog for quasar variability studies and for stellar astrometric microlensing measurements and predictions.

Quasar Spectra with Gaia

For at least 500,000 quasars, Gaia is producing astrometric, photometric and spectroscopic information. In order to investigate potential quasar variability studies with Gaia's low-resolution spectra, we simulated noisy spectra for various redshifts and for different magnitudes using a composite quasar spectrum as template. The detection of variability in quasar spectra is dependent on the signal-to-noise ratio which again is a function of the magnitude. We found that the SNR in the low-resolution spectra allows the analysis of continuum and broad emission line variability measurable up to a magnitude of $G \sim 18\,\mathrm{mag}$. In particular, we can measure the Baldwin effect for all of these bright quasars. Additionally, we would be able to measure sufficiently large time lags between continuum and broad emission line responses for a smaller number of objects. Considering the scanning law of the satellite, we found that especially spectral variations with time lags that are larger than a few months of bright ($G < 18\,\mathrm{mag}$) quasars are easy to detect within Gaia's data. However, even for time lags of order months, we need a high cadence of measurements to obtain accurate values for a reverberation mapping project. With this technique, we would be able investigate the structure of quasar broad line regions. Depending on the accuracy and amount of reverberation mapping data, we can determine cosmological luminosity distances with the

help of quasars.

We mainly used a composite quasar spectrum in this thesis to simulate realistic Gaia spectra. There is a considerable spread of quasar spectra that could influence our predictions. One example are objects with low equivalent width broad emission lines. However, our simulated template spectra are very useful because they present an overview on major quasar research applications possible to analyze with Gaia data. Especially when additional data simultaneously or following to Gaia observations are necessary, observational campaigns have to be planned in time.

Apart from low-resolution spectra, Gaia produces a high-resolution spectrum in a very small wavelength range as well. The high-resolution spectrum is only useful for quasars that have redshifts for which an emission line falls in this wavelength interval. At the faint magnitude limit, we calculated very low signal-to-noise ratios in the lines and hence Gaia could only analyze broad emission lines with the radial velocity spectrograph. Due to a revision of the originally proposed magnitude limit, we determined only 70 quasars fulfilling the conditions. Only for this small number of quasars, Gaia's high-resolution spectra could be used to investigate the broad emission line profiles and hence the broad line region structure.

Prediction of Stellar Astrometric Microlensing Events

By using astrometric microlensing detections, we can determine stellar masses[1] which serve as lens for the light of a background star. In Proft et al. (2011), we already predicted astrometric microlensing events between 2012 and 2019. Because we noticed that some microlensing events were missing in our previous research, we increased the search radius around our lensing stars in order to find close-by source objects. Similarly to our previous work, we excluded lensing stars with erroneous proper motion. In this process, we found 50 microlensing events from which six have maximal centroid shifts theoretically observable with Gaia. Two of these six events have bright lenses ($V < 11\,\text{mag}$) and such centroid shift values that there is a chance to detect the corresponding microlensing signal with the VLT instrument SPHERE as well.

Due to Gaia's scanning law and the smaller cross section of photometric microlensing events, the satellite will only be able to detect the corresponding photometric event for about 2% of the astrometric microlensing events. Additionally, our six new and the five already published promising events have Einstein times smaller than two weeks. Furthermore, for the majority, their photometric signals are below the detection limit of Gaia. Hence photometric observations from the ground are necessary to get more information on the individual events. Currently, when Gaia measures an astrometric microlensing event, the science alert team informs the community to get photometric measurements from earth. By predicting the events, we could improve the number of photometric observations with ground-based telescopes. Unfortunately, the centroid shift errors (similar to the centroid shift itself) and the errors of the event date (on average half a year) are very large. The reason for this are the positional and proper motion uncertainties in current astrometric catalogs.

Perspectives from Gaia's Data Releases

Before the end of the Gaia mission there will be four preliminary data releases, the first most likely this summer (2016). The first two data releases will not contain low- or high-resolution spectra at all.

---

[1]When the detection limit for astrometric microlensing improves, also planetary masses could be determined.

Apart from science alerts, observations of individual epochs will be published only in the final catalog. Hence we can not explore variability in quasar spectra with preliminary Gaia data releases. To perform a reverberation mapping campaign with complementary ground-based observations, we would need to determine the suitable quasar sample contemporary. The quasars should have high-cadence measurements and ideally also large time lags. As studied in this thesis, the time lag increases for large redshifts, the selection of low-ionisation lines, and large broad line region radii. In comparison to high-ionisation lines, low-ionisation lines are suitable because they have larger broad line region radii.

In future (at the earliest 2022), we can use the complete Gaia catalog to predict microlensing events. We then have an accurate list of high proper motion stars with revised uncertainties in positions and proper motions and in addition to this, information on stellar parallaxes for all lens and source stars. For the first time, we will be able to determine all lens and source distances and this to a high level of accuracy. By selecting these stars as lenses, we can calculate precise expected centroid shift trajectories and precise corresponding dates at closest approach between lens and source stars. With these predictions, astrometric microlensing could become a common technique to calculate masses of stellar lenses in the solar neighborhood to high accuracies of only about a few percent. But even before the final Gaia catalog, we can use the four preliminary data releases to gradually improve the different uncertainties. For example, we can use Gaia's first data release to predict astrometric microlensing events for the 2.5 million Tycho 2 stars. In this way, we still can detect potential events within Gaia's lifetime astrometrically and we could improve the centroid shift and microlensing date errors for these bright lenses ($V \lesssim 12\,\mathrm{mag}$). Additionally, by organizing a complementary photometric monitoring campaign, we would be able to observe the corresponding photometric microlensing event. Especially because of the much more precise microlensing dates, we have a real chance to observe the photometric signals.

A: Low-Resolution Quasar Spectra with Gaia
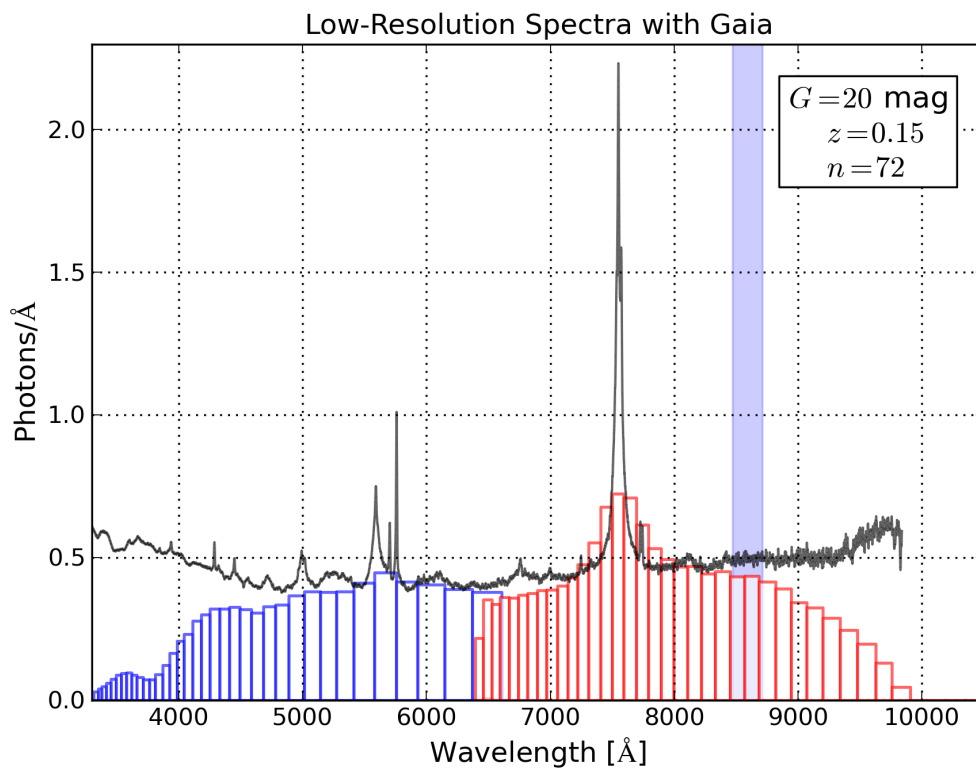
Figure 8.1: The diagram shows the composite quasar spectrum from VB2001 for redshift $z = 0.15$ and magnitude $G = 20$ in black. We present our simulated noisy low-resolution spectra of the blue photometer in blue and of the red photometer in red. 72 spectra of both FoVs are coadded to get spectra at the end of the Gaia mission. The blue shaded region indicates the area of the RVS. For this redshift, Gaia can measure the signal of Hβ and Hα.
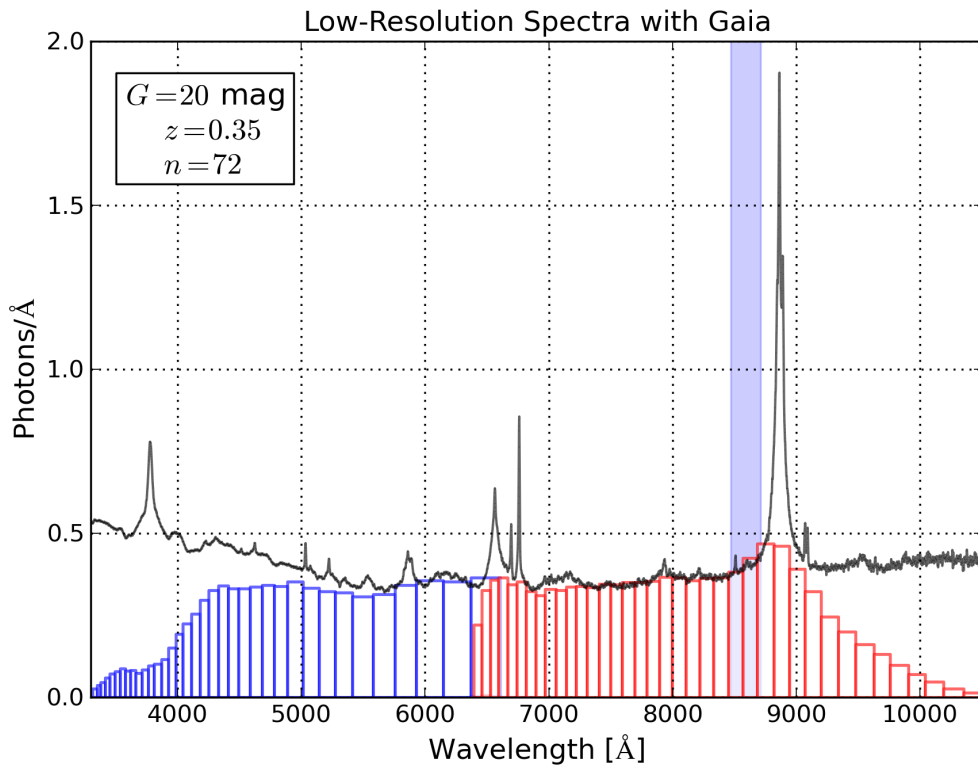
Figure 8.2: Same Figure as 8.1 but for redshift $z = 0.35$. For this redshift, Gaia can measure the signal of Hβ and Hα.
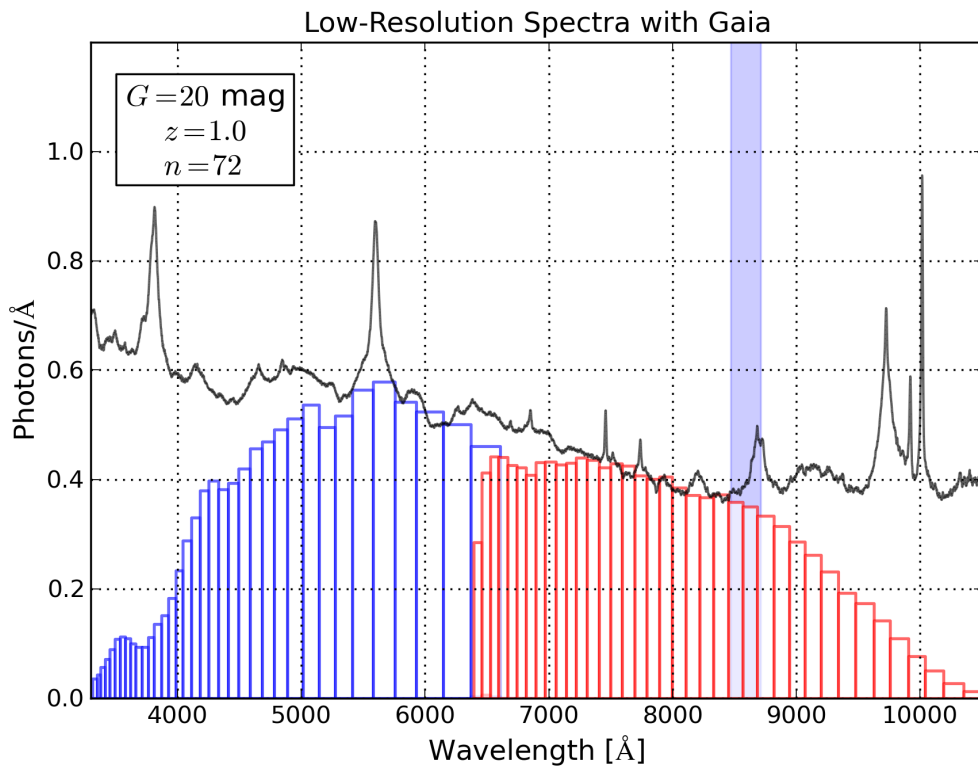
Figure 8.3: Same Figure as 8.1 but for redshift $z = 1.0$. It is the most difficult range to measure the redshift.
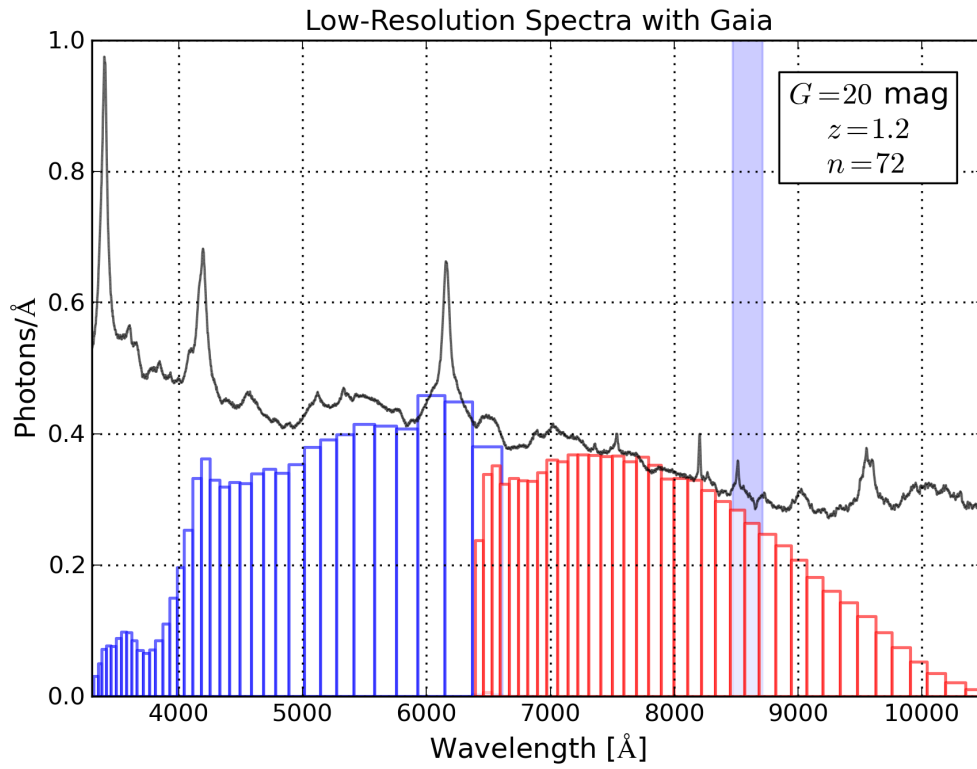
Figure 8.4: Same Figure as 8.1 but for redshift $z = 1.2$. For this redshift, Gaia can clearly measure the signal of MgII and CIII].
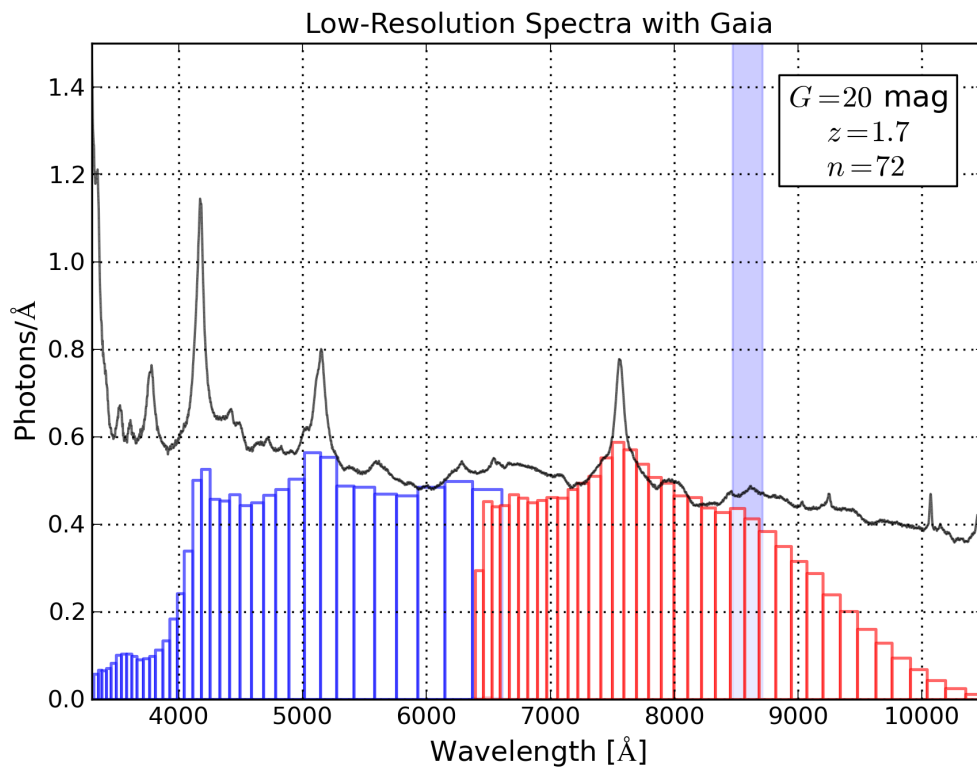
Figure 8.5: Same Figure as 8.1 but for redshift $z = 1.7$. For this redshift, Gaia can clearly measure the signal of MgII, CIII], and CIV.
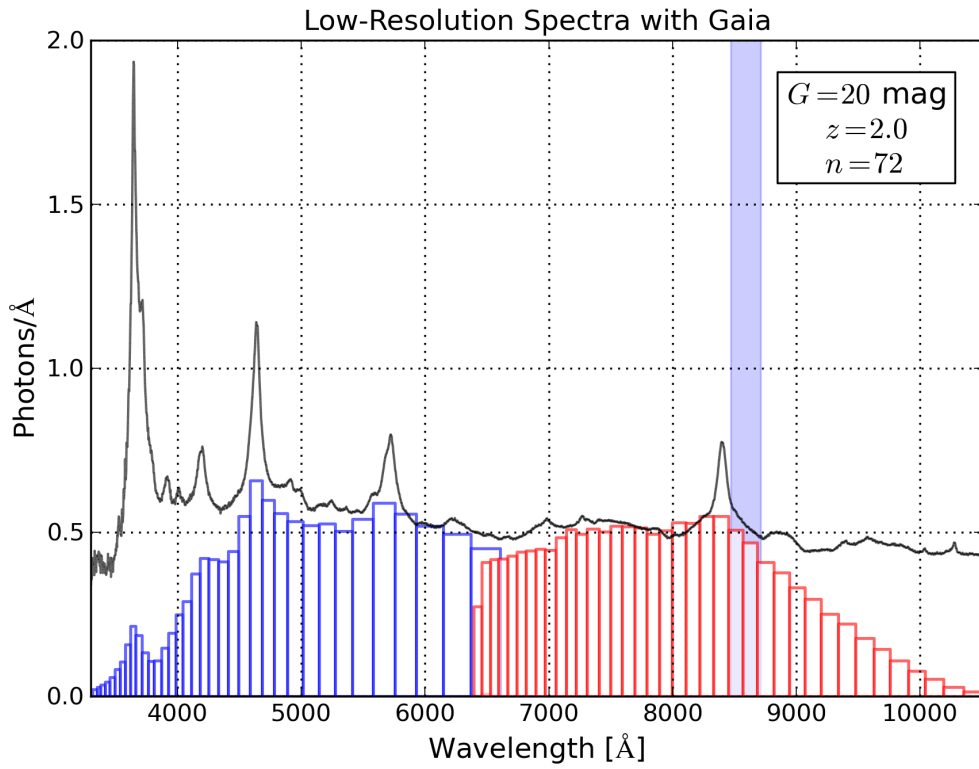
Figure 8.6: Same Figure as 8.1 but for redshift $z = 2.0$. For this redshift, Gaia can measure the signal of MgII, CIII], CIV, and Lyα.
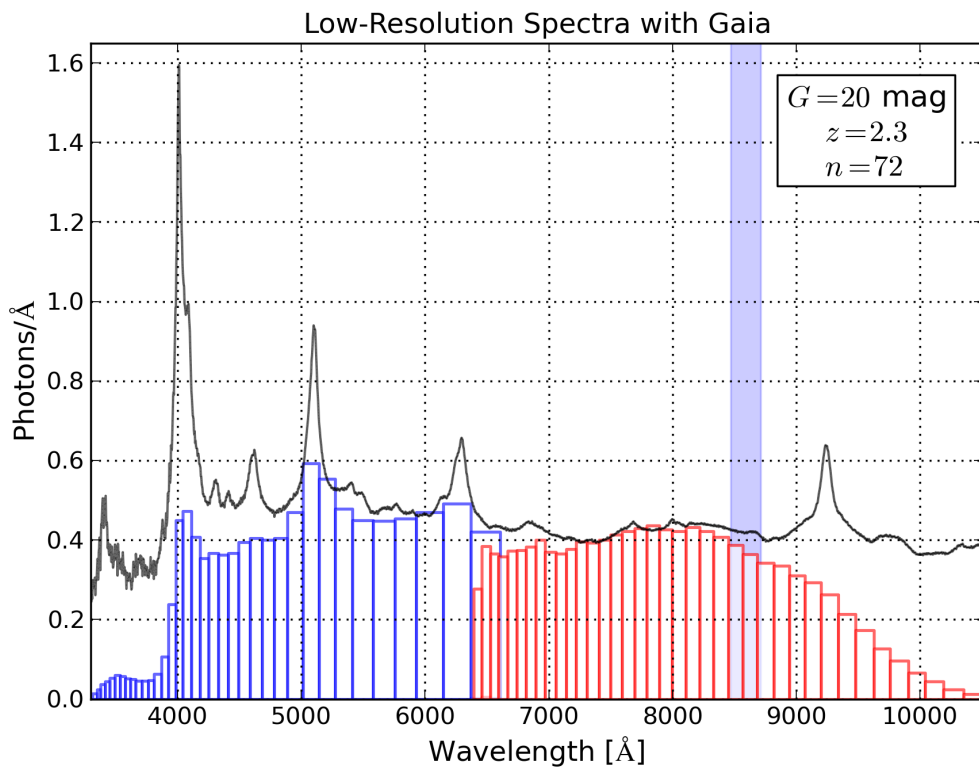
Figure 8.7: Same Figure as 8.1 but for redshift $z = 2.3$. For this redshift, Gaia can measure the signal of CIII], CIV, and Lyα.

B: Selected Published Microlensing Events between 2014 and 2019

Appendix

#	**P2011-18**	P2011-19	**P2011-20**	P2011-28	P2011-34
Lens ID	**LSPM J0431 +5858E**	LSPM J0207 +4938	**LSPM J2004 +3808**	LSPM J2022 +2657	LSPM J1209 +0042
α_{L} (deg)	**67.80238**	31.76613	**301.08704**	305.61134	182.36808
δ_{L} (deg)	**58.97810**	49.64538	**38.14137**	26.95245	0.70392
$t_{\min}$ (yr)	**2014.04±0.08**	2014.34±0.33	**2014.51±0.60**	2015.97±0.56	2016.95±0.36
$\vartheta_{\min}$ (")	**0.133±0.160**	0.061±0.130	**0.037±0.201**	0.012±0.173	0.152±0.137
μ_{L} ("/yr)	**2.375**	0.486	**0.341**	0.331	0.386
$m_{\mathrm{V,L}}$ (mag)	**12.1**	12.1	**12.7**	16.3	14.4
MK	**DC WD**	M3 V	**M1 V**	M4 V	M3 V
M_{V} (mag)	**13.3**	10.7	**9.5**	11.5	10.7
M_{L} ($M_{\odot}$)	**0.6**	0.35	**0.45**	0.3	0.35
D_{L} (pc)	**5.6**	19.3	**42.9**	92.5	55.7
θ_{E} (mas)	**29.560**	12.141	**9.243**	5.138	7.149
u_0 (θ_{E})	**4.5**	5.0	**4.0**	2.4	21.3
σ_{a} (mas)	**1.100**	0.610	**0.030**	1.050	0.380
$\theta_{\min}$ (mas)	**2.087**	1.157	**0.057**	1.992	0.721
$\delta\theta_{\mathrm{c,max}}$ (mas)	**5.972±5.946**	2.239±4.140	**2.069±8.810**	1.591±10.782	0.335±0.343
$\delta\theta_{\mathrm{c,res}}$ (mas)	**4.186±0.636**	0.732±0.278	**0.425±0.153**	0.132±0.046	0.255±0.128
$\delta\theta_{\mathrm{c,lum}}$ (mas)	**0.006±0.008**	0.005±0.012	**1.083±6.332**	0.093±1.368	13±15
t_{E} (days)	**5**	9	**10**	6	7
t_{ast} (days)	**101**	150	**2525**	23	105
μ_S ("/yr)	**0.011**	0.007	**0.024**	0.007	0.010
$m_{\mathrm{V,S}}$ (mag)	**19.7**	18.7	**12.7**	19.6	17.9

Table 8.1: We list the old microlensing events published in P2011 (excluding the events before 2014) with centroid shifts potentially measurable by Gaia. The shown properties are the same as in Table 7.5 and the shaded columns present the two events are the most promising events for a Gaia observation.

List of Figures

List of Tables

List of Publications

[1] **Proft, S.** & Wambsganss, J.
Exploration of quasars with the Gaia mission
2015, Astronomy & Astrophysics, 574, A46

[2] **Proft, S.**, Demleitner, M., & Wambsganss, J.
Prediction of astrometric microlensing events during the Gaia mission
2011, Astronomy & Astrophysics, 536, A50

[3 − 17] **Coauthor** paper published between 2011 and 2015 due to my observation in La Silla, Chile, between July 19 and August 2 in 2010 (MiNDSTEp program)

103

Bibliography

An, J. H. & Han, C. 2002, Astrophysical Journal, 573, 351

Andrei, A. H., Anton, S., Barache, C., et al. 2012, Mem. Societa Astronomica Italiana, 83, 930

Andrei, A. H., Souchay, J., Zacharias, N., et al. 2009, Astronomy and Astrophysics, 505, 385

Bahcall, J. N., Kirhakos, S., & Schneider, D. P. 1995, Astrophysical Journal, 450, 486

Bailer-Jones, C. A. L. et al. 2008, Monthly Notices of the Royal Astronomical Society, 391, 1838

Baldwin, J. A. 1977, Astrophysical Journal, 214, 679

Beckmann, V. & Shrader, C. R. 2012, Active Galactic Nuclei, ISBN-13: 978-3527410781. 350 pages. Wiley-VCH Verlag GmbH, 2012

Belokurov, V. & Evans, N. 2002, Mon.Not.Roy.Astron.Soc., 331, 649

Belokurov, V., Evans, N. W., & Du, Y. L. 2003, MNRAS, 341, 1373

Bessell, M. S. & Brett, J. 1988, Astronomical Society of the Pacific, 100, 1134

Blumenthal, G. R. & Mathews, W. G. 1975, Astrophysical Journal, 198, 517

Boch, T. & Fernique, P. 2014, in Astronomical Society of the Pacific Conference Series, Vol. 485, Astronomical Data Analysis Software and Systems XXIII, ed. N. Manset & P. Forshay, 277

Bonnarel, F., Fernique, P., Bienaymé, O., et al. 2000, Astronomy and Astrophysics, Supplement, 143, 33

Brown, A. 2006, Simulating Prism Spectra for the EADS-Astrium Gaia Design, Internal Gaia Report: GAIA-CA-TN-LEI-AB-005-7, Tech. rep.

Capellupo, D. M., Hamann, F., Shields, J. C., Rodríguez Hidalgo, P., & Barlow, T. A. 2012, Monthly Notices of the Royal Astronomical Society, 422, 3249

Carrasco, J. M. et al. 2006, GAIA-C5-TN-UB-JMC-001-2, Tech. rep.

Carroll, S. M. 2001, Living Reviews in Relativity, 4

Chelouche, D., Daniel, E., & Kaspi, S. 2012, Astrophysical Journal, Letters, 750, L43

Chung, S. et al. 2009, Astrophysical Journal, 695, 1357

Chwolson, O. 1924, Astronomische Nachrichten, 221, 329

Claeskens, J.-F., Smette, A., Vandenbulcke, L., & Surdej, J. 2006, Monthly Notices of the Royal Astronomical Society, 367, 879

Collier, S. et al. 1999, Monthly Notices of the Royal Astronomical Society, 302, L24

Collin-Souffrin, S. 1991, Astronomy and Astrophysics, 249, 344

Cutri, R. M. et al. 2003, The IRSA 2MASS All-Sky Point Source Catalog, NASA/IPAC Infrared Science Archive, http://irsa.ipac.caltech.edu/applications/Gator/

Czerny, B. & Hryniewicz, K. 2011, Astronomy and Astrophysics, 525, L8

Czerny, B., Hryniewicz, K., Maity, I., et al. 2013, A&A, 556, A97

de Bruijne, J. 2009, Along- and across-scan location-estimation performance, Tech. Rep. 1, European Space Agency

de Bruijne, J. H. J. 2012, Astrophysics and Space Science, 341, 31

Delchambre, L. 2014, GWP-S-831 Software Test Report for Cycle 15, Gaia Report: GAIA-C8-TR-IAGL-LD-003-15, Tech. rep.

Demleitner, M., Accomazzi, A., Eichhorn, G., et al. 2001, in Astronomical Society of the Pacific Conference Series, Vol. 238, Astronomical Data Analysis Software and Systems X, ed. F. R. Harnden, Jr., F. A. Primini, & H. E. Payne, 321

Disney, M. J., Boyce, P. J., Blades, J. C., et al. 1995, Nature, 376, 150

Dominik, M. & Sahu, K. C. 2000, Astrophysical Journal, 534, 213

Einstein, A. 1916, Annalen der Physik, 7, 769–822

Einstein, A. 1936, Science, 84, 506

Finet, F., Elyiv, A., & Surdej, J. 2012, Mem. Societa Astronomica Italiana, 83, 944

Friedman, A. A. 1922, Zeitschrift für Physik, 10, 377–386

George, I. M. & Fabian, A. C. 1991, Monthly Notices of the Royal Astronomical Society, 249, 352

Gil-Merino, R., Goicoechea, L. J., Shalyapin, V. N., & Braga, V. F. 2012, Astrophysical Journal, 744, 47

Goad, M. R., Korista, K. T., & Ruff, A. J. 2012, Monthly Notices of the Royal Astronomical Society, 426, 3086

Han, C., Chun, M., & Chang, K. 1999, Astrophysical Journal, 526, 405

Hestroffer, D., Dell'Oro, A., Cellino, A., & Tanga, P. 2010, in Lecture Notes in Physics, Berlin Springer Verlag, Vol. 790, Lecture Notes in Physics, Berlin Springer Verlag, ed. J. Souchay & R. Dvorak, 251–340

Hog, E. et al. 1995, Astronomy and Astrophysics, 294, 287

Holl, B., Prod'homme, T., Lindegren, L., & Brown, A. G. A. 2012, Monthly Notices of the Royal Astronomical Society, 422, 2786

Honma, M. 2001, Publications of the Astronomical Society of Japan, 53, 233

Hsu, C.-M. & Blaes, O. 1998, Astrophysical Journal, 506, 658

Hubble, E. 1929, Proceedings of the National Academy of Science, 15, 168

Jackson, N. 2015, Living Reviews in Relativity, 18

Jester, S., Schneider, D. P., Richards, G. T., et al. 2005, Astronomical Journal, 130, 873

Jones, E. M. 1972, Astrophysical Journal, 177, 245

Jordan, S. 2008, Astron.Nachr., 329, 875

Jordi, C. 2013, Photometric relationships between Gaia photometry and existing photometric systems, Gaia Report: GAIA-C5-TN-UB-CJ-041-8, http://www.rssd.esa.int/SYS/docs/ll_transfers/project=PUBDB&id=2760608.pdf, Tech. rep.

Jordi, C. 2015, in Highlights of Spanish Astrophysics VIII, ed. A. J. Cenarro, F. Figueras, C. Hernández-Monteagudo, J. Trujillo Bueno, & L. Valdivielso, 390–401

Jordi, C. & Carrasco, J. M. 2007, in Astronomical Society of the Pacific Conference Series, Vol. 364, The Future of Photometric, Spectrophotometric and Polarimetric Standardization, ed. C. Sterken, 215

Jordi, C., Gebran, M., Carrasco, J. M., et al. 2010, Astronomy and Astrophysics, 523, A48

Kaler, J. B. 1994, Sterne und ihre Spektren (Heidelberg ; Berlin ; Oxford: Spektrum, Akad. Verl.), 367 S.

Kaspi, S. et al. 2007, Astrophysical Journal, 659, 997

Kembhavi, A. K. & Narlikar, J. V. 1999, Quasars and active galactic nuclei : an introduction (Cambridge University Press)

Kochanek, C., Falco, E., Impey, C., et al. 2013, "CASTLES Survey: Gravitational Lens Data Base", project homepage, Harvard-Smithsonian Center for Astrophysics. URL (cited on 1 December 2013): http://cfa-www.harvard.edu/glensdata/

Kollatschny, W. & Zetzl, M. 2013, Astronomy and Astrophysics, 549, A100

Kotilainen, J. K., Falomo, R., Decarli, R., et al. 2009, Astrophysical Journal, 703, 1663

Lee, C.-H. et al. 2010, Monthly Notices of the Royal Astronomical Society, 407, 1597

Lepine, S. & Shara, M. M. 2005, The Astronomical Journal, 129, 1483

Lewis, G. F. & Ibata, R. A. 1998, ApJ, 501, 478

Lindegren, L. & Bastian, U. 2011, in EAS Publications Series, Vol. 45, EAS Publications Series, 109–114

Luyten, W. J. 1979, LHS catalogue. A catalogue of stars with proper motions exceeding 0"5 annually, ed. Luyten, W. J.

Luyten, W. J. & Hughes, H. S. 1980, Sep. print University of Minnesota, Minneapolis, MN (USA), 16 p., 55, 1

MacLeod, C. L., Ivezić, v., Sesar, B., et al. 2012, Astrophysical Journal, 753, 106

MacLeod, C. L., Ivezić, Ž., Kochanek, C. S., et al. 2010, Astrophysical Journal, 721, 1014

Mao, S. & Paczynski, B. 1991, Astrophysical Journal Letters, 374, L37

Meusinger, H., Hinze, A., & de Hoon, A. 2011, Astronomy and Astrophysics, 525, A37

Mignard, F. 2002, in EAS Publications Series, Vol. 2, EAS Publications Series, ed. O. Bienayme & C. Turon, 327–339

Mignard, F. 2012, Mem. Societa Astronomica Italiana, 83, 918

Miralda-Escude, J. 1996, Astrophysical Journal Letters, 470, L113+

Miyamoto, M. & Yoshii, Y. 1995, Astronomical Journal, 110, 1427

Morgan, C. W. et al. 2010, Astrophysical Journal, 712, 1129

Paczynski, B. 1986, Astrophysical Journal, 304, 1

Paczynski, B. 1995, Acta Astron., 45, 345

Paczynski, B. 1996a, Gravitational Microlensing in the Local Group, Tech. Rep. POPe-661

Paczynski, B. 1996b, Acta Astronomica, 46, 291

Paczynski, B. 1998, Astrophysical Journal Letters, 494, L23

Pâris, I., Petitjean, P., Aubourg, É., et al. 2012, Astronomy and Astrophysics, 548, A66

Perlmutter, S., Aldering, G., Goldhaber, G., et al. 1999, Astrophysical Journal, 517, 565

Perryman, M. et al. 2001, Astron.Astrophys., 369, 339

Peterson, B. M. 1993, Publications of the Astronomical Society of the Pacific, 105, 247

Peterson, B. M. 1997, An introduction to active galactic nuclei. (Cambridge University Press)

Peterson, B. M., Ferrarese, L., Gilbert, K. M., et al. 2004, Astrophysical Journal, 613, 682

Peterson, B. M. & Horne, K. 2004, Astronomische Nachrichten, 325, 248

Peterson, B. M. & Wandel, A. 1999, Astrophysical Journal, Letters, 521, L95

Planck Collaboration, Ade, P. A. R., Aghanim, N., et al. 2015, ArXiv e-prints

Popović, L. v., Jovanović, P., Stalevski, M., et al. 2012, A&A, 538, A107

Popović, L. v. & Simić, S. 2013, MNRAS, 432, 848

Proft, S. 2010, Diploma thesis, Heidelberg, Univ., Vorhersage astrometrischer Mikrolinsenkandidaten für den Zeitraum der Gaia-Mission

Proft, S., Demleitner, M., & Wambsganss, J. 2011, A&A, 536, A50

Proft, S. & Wambsganss, J. 2015, Astronomy and Astrophysics, 574, A46

Riess, A. G., Filippenko, A. V., Challis, P., et al. 1998, Astronomical Journal, 116, 1009

Robin, A. C., Luri, X., Reylé, C., et al. 2012, Astronomy and Astrophysics, 543, A100

Roeser, S., Demleitner, M., & Schilbach, E. 2010, The Astronomical Journal, 139, 2440

Roeser, S. et al. 2008, Astronomy and Astrophysics, 488, 401

Salim, S. & Gould, A. 2000, Astrophysical Journal, 539, 241

Salim, S. & Gould, A. 2003, Astrophysical Journal, 582, 1011

Schmid, H. M. 2009, VLT-BBB-SPH-14690-GGGG, Tech. Rep. 1, ETH Zurich

Schmidt, M. 1963, Nature, 197, 1040

Schneider, D. P., Richards, G. T., Hall, P. B., et al. 2010, VizieR Online Data Catalog, 7260, 0

Schneider, P. 2006, Einführung in die Extragalaktische Astronomie und Kosmologie (Berlin, Heidelberg: Springer-Verlag Berlin Heidelberg), Online–Ressource, in: Springer-Online

Schneider, P., Kochanek, C. S., & Wambsganss, J. 2006, Gravitational Lensing: Strong, Weak and Micro (Springer-Verlag)

Shen, Y. 2012, ApJ, 757, 152

Slezak, E. & Mignard, F. 2007, A realistic QSO Catalogue for the GAIA Universe Model, Gaia-c2-tn-oca-es-001-1, Observatoire de la Côte d'Azur

Sumi, T. et al. 2004, Monthly Notices of the Royal Astronomical Society, 348, 1439

Taris, F., Souchay, J., Andrei, A. H., et al. 2011, A&A, 526, A25

Treyer, M. & Wambsganss, J. 2004, A&A, 416, 19

Urry, C. M. & Padovani, P. 1995, Publications of the Astronomical Society of the Pacific, 107, 803

Vanden Berk, D. E., Richards, G. T., Bauer, A., et al. 2001, Astronomical Journal, 122, 549 (VB2001)

Vanden Berk, D. E., Wilhite, B. C., Kron, R. G., et al. 2004, Astrophysical Journal, 601, 692

Walker, M. A. 1995, Astrophysical Journal, 453, 37

Watson, D., Denney, K. D., Vestergaard, M., & Davis, T. M. 2011, Astrophysical Journal, Letters, 740, L49

Weigert, A., Wendker, H. J., & Wisotzki, L. 2006, Astronomie und Astrophysik, 4th edn., Lehrbuch Physik (Weinheim: Wiley-VCH Verlag), XVI, 424 S.

Wenger, M., Ochsenbein, F., Egret, D., et al. 2000, Astronomy and Astrophysics, Supplement, 143, 9

Wilhite, B. C., Vanden Berk, D. E., Brunner, R. J., & Brinkmann, J. V. 2006, Astrophysical Journal, 641, 78

Wilhite, B. C., Vanden Berk, D. E., Kron, R. G., et al. 2005, Astrophysical Journal, 633, 638

Wyrzykowski, Ł. & Hodgkin, S. 2012, in IAU Symposium, Vol. 285, IAU Symposium, ed. E. Griffin, R. Hanisch, & R. Seaman, 425–428

Zacharias, N. et al. 2010, Astronomical Journal, 139, 2184

Acknowledgements

At the end of this thesis, I am glad to acknowledge all the people who supported my work on this dissertation and beyond. First of all, I would like to thank my supervisor Joachim Wambsganss for his helpful advises to my research, my presentation skills and also for providing financial support. Moreover, I am very grateful that it was possible to balance my family and work under his supervison.

During my thesis, I was very glad to have scientists from many different research fields in our institute who were interested in my work and could contribute to my investigations. In particular, I wish to thank Ulrich Bastian for detailed information on the Gaia mission and for his attendence in my thesis committees. I want to thank Anna Pasquali for helpful comments on spectra analyses and Markus Demleitner for constructive comments about the detection of astrometric microlensing events. Moreover, I am indebted to thank Robert Schmidt for answering questions regarding many different kinds of research fields.

I want to thank Jochen Heidt for his immediate agreement to be the second corrector of my dissertation and to be a member of my three thesis committees. Additionaly, I want to thank him, Eva Grebel, and Ulrich Platt to be my PhD committee members.

A special thank goes to the former group member Janine Fohlmeister for many scientific and non-scientific discussions. For about four years, we collaborated to inspire seventh grade girls for physics and astronomy which I enjoyed very much. In this context, I want to thank Lina Girdziute for managing this project and the equal opportunities office for financial support. For me, Janine acted as a role model that it is possible to have a family while working on a dissertation.

Robert Schmidt, Thomas Gerner, and Sebastian Martschat read my thesis and gave constructive comments with regard to improving the scientific understanding and the English language. For this, I am very grateful and I want to thank them for their time.

Since my start at ARI, I am a member of the lensing group and I got to know many students and scientists. In this context, I wish to thank Christiane Diehl, Janine Fohlmeister, Thomas Gerner, Emanuela Giannini, Fabian Köhlinger, Dominik Leier, Robert Schmidt, Frederik Schönebeck, Dominique Sluse, Yannis Tsapras, Michael Walther, and Fabian Zimmer for deep scientific discussions in our group seminars, journal clubs, and beyond.

In the last years, I had many different office neighbors with which I could talk about our studies, astronomical news, or private events. Specially, I wish to thank Emanuela Giannini and Christiane Diehl for a really nice time together.

Finally, I want to thank my family and my closest friends to believe in me and for all their support. Especially, I deeply thank Sebastian and Leni. Your are the most important motivation in my life.

Statement of Authorship - Selbständigkeitserklärung

Ich, Svea Proft, versichere, dass ich die vorgelegte Dissertation selbstständig verfasst habe und keine anderen als die angegebenen Quellen und Hilfsmittel benutzt habe.